Terrestrial Environmental Sciences

Haibing Shao · Ju Wang · Thorsten Schäfer · Chun-Liang Zhang · Horst Geckeis · Thomas Nagel · Uwe Düsterloh · Olaf Kolditz · Hua Shao *Editors*

Thermo-Hydro-Mechanical-Chemical (THMC) Processes in Bentonite Barrier Systems

OPEN ACCESS

Springer

Terrestrial Environmental Sciences

Understanding the function and evolution of terrestrial environmental systems is fundamental to many environmental aspects investigated in the geo- and hydrosciences. The terrestrial environmental systems under investigation here range from the geosphere and its related water cycle to associated matter fluxes and biogeochemical transformations. Modelling is important for system characterization and understanding as well as describing potential paths of terrestrial environmental systems. Benchmarking builds a bridge to experimental studies and provides a methodology for model validation. Moreover, benchmarking and code comparison foster community efforts. This book series invites contributions in fundamental and applied aspects in terrestrial environmental sciences as well as in other related fields to promote interdisciplinary approaches.

Haibing Shao · Ju Wang · Thorsten Schäfer ·
Chun-Liang Zhang · Horst Geckeis ·
Thomas Nagel · Uwe Düsterloh · Olaf Kolditz ·
Hua Shao
Editors

Thermo-Hydro-Mechanical-Chemical (THMC) Processes in Bentonite Barrier Systems

Springer

Editors
See next page

ISSN 2363-6181 ISSN 2363-619X (electronic)
Terrestrial Environmental Sciences
ISBN 978-3-031-53203-0 ISBN 978-3-031-53204-7 (eBook)
https://doi.org/10.1007/978-3-031-53204-7

This Springer imprint is published by the registered company Springer Nature Switzerland AG
The registered company address is: Gewerbestrasse 11, 6330 Cham, Switzerland

Paper in this product is recyclable.

Editors
Haibing Shao
Department Umweltinformatik
Helmholtz Centre for Environmental Research
Leipzig, Germany

Thorsten Schäfer
Applied Geology
Institute of Geosciences
Friedrich-Schiller-Universität Jena
Jena, Germany

Horst Geckeis
Institute for Nuclear Waste Disposal
Karlsruhe Institute of Technology
Karlsruhe, Germany

Uwe Düsterloh
Chair for Geomechanics and Multiphysics Systems
Technische Universität Clausthal
Clausthal-Zellerfeld, Germany

Hua Shao
Federal Institute for Geosciences and Natural Resources
Hannover, Germany

Ju Wang
Beishan URL for HLW Disposal
China National Nuclear Corporation
Beijing, China

Chun-Liang Zhang
Gesellschaft für Anlagen- und Reaktorsi
Köln, Germany

Thomas Nagel
Geotechnical Institute
TU Bergakademie Freiberg
Freiberg, Germany

Olaf Kolditz
Department of Environmental Informatics
Helmholtz Centre for Environmental Research
Leipzig, Germany

Acknowledgements

The project “Deutsch-Chinesische Entsorgungsforschung—Pilotprojekt: Reanalysis of BRIUG THM Mock-up Test (ELF-China-Pilot)” is funded by the Federal Ministry for Economic Affairs and Climate Action (BMWi/BMWK).

The funding under grant numbers 02E11850A-F is greatly acknowledged.

Funded by

Project partners

Contributions

We appreciate the contributions to the ELF-China project by:

- (BGR, Federal Institute for Geosciences and Natural Resources, Hanover, DE)
  - Stephan Kaufhold (BGR, Federal Institute for Geosciences and Natural Resources, Hanover, DE)
  - Hua Shao (BGR, Federal Institute for Geosciences and Natural Resources, Hanover, DE)
- (BRIUG, Beijing Research Institute of Uranium Geology, Beijing, CN)
  - Ju Wang (BRIUG, Beijing Research Institute of Uranium Geology, Beijing, CN)
  - Yuemiao Liu (BRIUG, Beijing Research Institute of Uranium Geology, Beijing, CN)
  - Qi Zhang (BRIUG, Beijing Research Institute of Uranium Geology, Beijing, CN)
  - Jingli Xie (BRIUG, Beijing Research Institute of Uranium Geology, Beijing, CN)
  - Nana Li (BRIUG, Beijing Research Institute of Uranium Geology, Beijing, CN)
  - Liang Chen (BRIUG, Beijing Research Institute of Uranium Geology, Beijing, CN)
  - Rui Su (BRIUG, Beijing Research Institute of Uranium Geology, Beijing, CN)
  - Xingguang Zhao (BRIUG, Beijing Research Institute of Uranium Geology, Beijing, CN)
  - Shengfei Cao (BRIUG, Beijing Research Institute of Uranium Geology, Beijing, CN)
  - Like Ma (BRIUG, Beijing Research Institute of Uranium Geology, Beijing, CN)
  - Jingbo Zhao (BRIUG, Beijing Research Institute of Uranium Geology, Beijing, CN)

- (FSU, Friedrich-Schiller-Uiversität, Jena, DE)
  - Thorsten Schäfer (FSU, Friedrich-Schiller-Uiversität, Jena, DE)
  - Janis Pingel (FSU, Friedrich-Schiller-Uiversität, Jena, DE)
- (GRS, Gesellschaft für Anlagen- und Reaktorsicherheit gGmbH, Braunschweig, DE)
  - Oliver Czaikowski (GRS, Gesellschaft für Anlagen- und Reaktorsicherheit gGmbH, Braunschweig, DE)
  - Chun-Liang Zhang (GRS, Gesellschaft für Anlagen- und Reaktorsicherheit gGmbH, Braunschweig, DE)
- (KIT, Karlsruhe Institute of Technology, Karlsruhe, DE)
  - Horst Geckeis (KIT, Karlsruhe Institute of Technology, Karlsruhe, DE)
  - Yasmine Kouhail (KIT, Karlsruhe Institute of Technology, Karlsruhe, DE)
  - Muriel Bouby (KIT, Karlsruhe Institute of Technology, Karlsruhe, DE)
  - Frank Heberling (KIT, Karlsruhe Institute of Technology, Karlsruhe, DE)
  - Nikoletta Morélova (KIT, Karlsruhe Institute of Technology, Karlsruhe, DE)
  - Madeleine Stoll (KIT, Karlsruhe Institute of Technology, Karlsruhe, DE)
  - Stephanie Kraft (KIT, Karlsruhe Institute of Technology, Karlsruhe, DE)
  - Nadine Gill (KIT, Karlsruhe Institute of Technology, Karlsruhe, DE)
  - Claudia Joseph (KIT, Karlsruhe Institute of Technology, Karlsruhe, DE)
- (UFZ, Helmholtz Centre for Environmental Research, Leipzig, DE)
  - Chaofan Chen (UFZ, Helmholtz Centre for Environmental Research, Leipzig, DE)
  - Olaf Kolditz (UFZ, Helmholtz Centre for Environmental Research, Technische Universität Dresden, Germany)
  - Haibing Shao (UFZ, Helmholtz Centre for Environmental Research, Leipzig, DE)
  - Wenqing Wang (UFZ, Helmholtz Centre for Environmental Research, Leipzig, DE)
- (TUBAF, Technische Universität Bergakademie Freiberg, Freiberg, DE)
  - Aqeel Afzal Chaudhry (TUBAF, Technische Universität Bergakademie Freiberg, Germany)
  - Heinz Konietzky (TUBAF, Technische Universität Bergakademie Freiberg, Germany)
  - Thomas Nagel (TUBAF, Technische Universität Bergakademie Freiberg, Germany)
- (TUC, Technische Universität Clausthal; Clausthal-Zellerfeld, DE)
  - Uwe Düsterloh (TUC, Technische Universität Clausthal; Clausthal-Zellerfeld, DE)
  - Juan Zhao (TUC, Technische Universität Clausthal; Clausthal-Zellerfeld, DE)

Contents

List of Figures

List of Tables

Chapter 1
Introduction

Haibing Shao, Ju Wang, Thorsten Schäfer, Chun-Liang Zhang, Horst Geckeis, Thomas Nagel, Uwe Düsterloh, Olaf Kolditz, and Hua Shao

For the disposal of high-level radioactive waste in deep geological formations, different host rocks (rock salt, crystalline and clay rock) are investigated internationally. According to the Site Selection Act (StandAG), the three host rocks that are potentially suitable for the disposal of high-level radioactive waste in Germany–rock salt,

H. Shao · O. Kolditz
Helmholtz Centre for Environmental Research UFZ, 04318 Leipzig, Germany

J. Wang
Beishan Underground Research Laboratory for HLW Disposal, Beijing Research Institute of Uranium Geology, Beijing 100029, China

T. Schäfer
Friedrich-Schiller-University Jena, Institute of Geosciences, Applied Geology, Jena, Germany

C.-L. Zhang
Gesellschaft für Anlagen- und Reaktorsicherheit (GRS) gGmbH, 38122 Braunschweig, Germany

H. Geckeis
Karlsruhe Institute of Technology, Institute for Nuclear Waste Disposal (INE), 76094 Karlsruhe, Germany

T. Nagel
Technische Universität Bergakademie Freiberg, Geotechnical Institute, 09599 Freiberg, Germany

U. Düsterloh
Clausthal University of Technology, Geomechanics and Multiphysical Systems, 38678 Clausthal-Zellerfeld, Germany

H. Shao (✉)
Federal Institute for Geosciences and Natural Resources (BGR), 30655 Hannover, Germany
e-mail: Hua.Shao@bgr.de

H. Shao et al. (eds.), *Thermo-Hydro-Mechanical-Chemical (THMC) Processes in Bentonite Barrier Systems*, Terrestrial Environmental Sciences,
https://doi.org/10.1007/978-3-031-53204-7_1

clay rock and crystalline rock (such as granite)–must be taken into account. Since there is no repository mine for high-level radioactive waste and no underground laboratory in these host rocks for repository research in Germany, German institutions are involved in research work in international rock laboratories in order to gain or expand knowledge of these host rocks. The German institutions have already been involved in geoscientific experiments in the Grimsel (Switzerland) and Äspö (Sweden) rock laboratories, where the properties of the granite formations are being explored.

Due to the rapid economic development in China, the energy requirement there has increased tenfold in recent years. To reduce fossil fuel consumption, 44 nuclear reactors with a capacity of 58 GW are currently (as of the end of 2019) in operation and 13 reactors with a capacity of 30 GW are under construction. The search for a site for a repository for high-level radioactive waste began in 1985. Two host rocks (granite and clay) are being intensively studied in China. In the Gobi desert (granite formation, the climatic (low precipitation, high evaporation), hydrogeological (low water table), and geological (stable crust, low seismicity) conditions as well as the social (low population density) and economic (infrastructure development due to the potential repository site) situations seem to be well suited for a repository. In 2020, the permit to set up an underground research laboratory (URL) has now been granted (Sect. 2.1).

In June 2021, the construction of the underground research laboratory (URL) started in the crystalline rock in the Gobi desert (Gansu province). The ground infrastructure with offices, conference rooms and workshops as well as access road and water supply have been completed now. The excavation phase with three shafts and a ramp of about 7 km length and a maximum depth of 560 m offers the opportunity to observe and evaluate the hydraulic, mechanical and geochemical changes in the fractured rock as a result of this intervention.

The Chinese repository concept for high-level radioactive waste in granitic rock is based on the multi-barrier system with bentonite as the backfilling and sealing material for boreholes, tunnels and and shafts after emplacement. For this purpose, the Chinese bentonite GMZ (GaoMiaoZi) is intended as shaped stones and pellets, which is extracted in an open-pit mine with a deposit reserve of 160 megatons (Chen et al., 2014). Extensive laboratory tests are carried out to determine the thermal, hydraulic, mechanical and chemical properties of the GMZ bentonite. A long-term mock-up test was started in 2011 to study the behavior of GMZ bentonite under the simulated repository conditions (Sect. 2.2).

In 2018, a Joint Declaration of Intent (JDoI) was signed between the Federal Ministry for Economic Affairs and Energy (BMWi), now BMWK and the China National Nuclear Corporation (CNNC). The aim of the JDoI is to promote possible cooperation in the field of repository research and nuclear safety and to create a general framework for cooperation. Under these conditions, the potential German partners have developed the following two project outlines:

- Study of thermo-hydro-mechanical-chemical processes on GMZ bentonite,
- ‘Fact-finding study’ on crystalline rock characterization and public acceptance.

On this basis, the project management organization Karlsruhe (PTKA) initiated a pilot project to investigate the GMZ on behalf of the BMWi in 2020. Helmholtz Center for Environmental Research (UFZ), TU Bergakademie Freiberg (TUBAF), Gesellschaft für Anlagen- und Reaktorsicherheit gGmbH (GRS), Technical University of Clausthal (TUC), Friedrich Schiller University Jena (FSU Jena), the Karlsruhe Institute of Technology (KIT), and Federal Institute for Geosciences and Natural Resources (BGR) are involved in these investigations. The pilot project focuses on thermal-hydrogeological-mechanical and chemical processes in bentonites (GMZ and MX-80, a bentonite intensively studied in many countries) and includes both experimental work and numerical modelling. The aim of this project are model and method verification as well as results comparison from different institutions.

The safe deposition of high-level radioactive waste from the energy industry is one of the major societal challenges of this century worldwide. At the same time, final disposal in deep geological formations is considered the safest solution to date–with many scientific and technical challenges still to overcome. The Pilot Project "Thermo-Hydro-Mechanical-Chemical (THMC) Processes in Bentonite Barrier Systems" is a collaborative project between German and Chinese scientists to organize a bilateral comparison of methods and technologies in (1) experimental laboratory and field research as well as in (2) systems analysis. Both German and Chinese partners obtain excellent complementary experimental and modeling research facilities. China's first underground research laboratory for geological disposal of high-level radioactive waste (Beishan URL) is currently under construction and will serve as an international collaboration platform for URL research in future. Due to the high cost of scientific programs and the technical operation of URLs, international cooperation is not only essential but also a prerequisite for excellent research and development to provide safe solutions–not only for radioactive waste deposition into deep geological repositories but also for other geoenergy applications such as energy storage and geothermal energy utilization.

Reference

Chen, L., Liu, Y. M., Wang, J., Cao, S. F., Xie, L. K., Zhao, X. G., Li, Y. W., & Liu, J. (2014). Investigation of the thermal-hydro-mechanical (THM)behavior of GMZ bentonite in the China-Mock-up test. *Engineering Geology, 172*. http://doi.org/10.1016/j.enggeo.2014.01.008

Chapter 2
Lab and Field Experimental Infrastructures

J. Wang, L. Chen, R. Su, X. G. Zhao, Y. M. Liu, S. F. Cao, J. L. Xie, and L. K. Ma

2.1 Beishan Underground Research Laboratory (URL)

J. Wang, L. Chen, R. Su, X. G. Zhao

Long-term safe disposal of high-level radioactive waste (HLW) is a challenging task for countries with nuclear power production. Due to its high radioactivity and long half-life, the HLW needs to be permanently isolated from the human environment. Geological disposal has been widely accepted as a feasible approach for safe management of HLW. Deep geological repositories (DGRs) can be built in suitable geological formations at a depth of several hundred meters below ground level. Various rock types such as granite, clay, tuff, and rock salt have been considered as potential rocks for hosting DGRs (Ahn, 2010). However, due to lack of actual implementation experience, the development of DGRs is a long-term and systematic research process. To develop DGRs successfully, many countries constructed underground research laboratories (URLs) to evaluate site suitability, develop and verify disposal concepts, optimize repository system components, and demonstrate long-term safety of DGRs (Wang et al., 2018).

2.1.1 The Strategy for China's URL

With the rapid development of nuclear industry, China has an urgent and strategic need for safe disposal of HLW. In accordance with the Guidelines on Research and Development (R&D) Planning for Geological Disposal of High-level Radioactive

J. Wang (✉) · L. Chen · R. Su · X. G. Zhao · Y. M. Liu · S. F. Cao · J. L. Xie · L. K. Ma
CAEA Innovation Center for Geological Disposal of High-Level Radioactive Waste, Beijing 100029, China
e-mail: wangju9818@163.com

Beijing Research Institute of Uranium Geology, Beijing 100029, China

H. Shao et al. (eds.), *Thermo-Hydro-Mechanical-Chemical (THMC) Processes in Bentonite Barrier Systems*, Terrestrial Environmental Sciences,
https://doi.org/10.1007/978-3-031-53204-7_2

Waste, which was issued by the China Atomic Energy Authority (CAEA), the Ministry of Science and Technology (MOST) and the former Ministry of Environment Protection (MOEP) in 2006, the China's strategy for HLW disposal is divided into three phases: (1) laboratory-based research and site selection for the disposal facility (2006–2020), (2) underground research and testing (2021–2040), and (3) the disposal facility construction (2041–2050) (Wang, 2010; CAEA, 2006). A milestone is to complete the construction of China's URL by 2020. Moreover, the 13th Five-year Plan of China (2016–2020) stated that "the construction of China's URL for HLW disposal should start before 2020", indicating that the Chinese government attaches great importance to the development of the URL.

Based on an analysis on the development process of URLs worldwide in combination with considerations of current situation in China, a newly defined type of URL (i.e., area-specific URL) was proposed (Wang, 2014). An area-specific URL is located at a site in an area that is considered as a potential area for a DGR. When an area has been selected as the first priority area for a DGR, but a specific site has not been determined, an area-specific URL can be built as long as the site has similar geological conditions to those of a future in-depth DGR site. The area-specific URL has a potential role, i.e., if investigations performed in the URL confirm that the site is suitable for a DGR, the siting process of the DGR will be accelerated. In addition, the acquired data, investigation results, and experience gained from an area-specific URL can be transferable to the future DGR in this area. Therefore, it is also called "Generation 3" URL. With this basic understanding, the major considerations of the China's URL strategy are as follows (Wang et al., 2018):

1. To build an area-specific URL in a representative granite formation within the area that has been identified as having the greatest potential for a DGR in China.
2. The URL will be a large-scale facility with full functionality.
3. The URL will be about 500 m deep, similar to the depth of the future repository.
4. The URL should be expandable.
5. The URL will serve for technology development and demonstration, site characterization, and public acceptance.
6. The URL will be open to international cooperation in the field of geological disposal.

2.1.2 Site Selection and Site Characterization for China's URL

2.1.2.1 Site Selection

Site selection for China's DGR started in 1985 (Wang et al., 2018). Considerable effort has been devoted to the selection of potential sites in granite formations. The attention on granite formations was primarily driven by the widespread occurrence of such rocks in China, coupled with the fact that granitic rocks are suitable for hosting

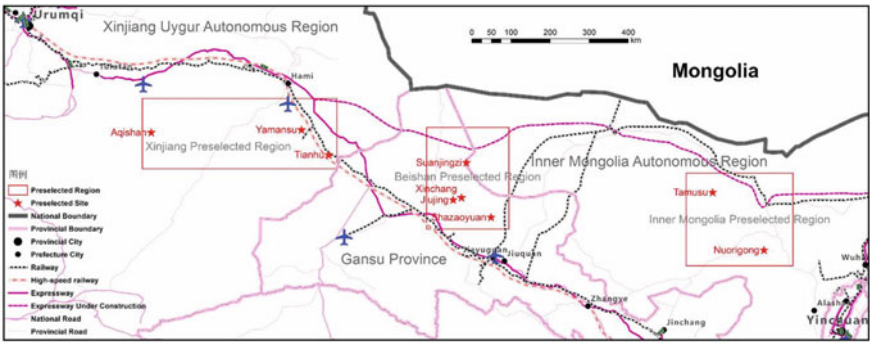

Fig. 2.1 Location of candidate URL sites in China (Wang et al., 2018)

DGRs. Over the past 30 years, significant progress has been made in site selection of the DGR. Six regions were selected as potential regions for the DGR (Wang et al., 2018). Based on a preliminary comparison of the six pre-selected regions, the focus was on site selection and site characterization in northwestern China, Inner Mongolia, and Xinjiang regions, as shown in Fig. 2.1. In 2011, the CAEA and the former MOEP jointly organized an expert meeting. In this meeting, the Beishan area of northwestern China was recommended as the first priority area for China's DGR (Wang et al., 2018). This decision provided an important basis for selecting the URL site.

Based on the achievements obtained from site selection of the DGR, site selection for China's URL started in 2015. Nine candidate URL sites (Fig. 2.1) were selected for further comparison and demonstration. In the Beishan area, there are four candidate sites. In the Xinjiang and the Inner Mongolia pre-selected regions, there exist three and two candidate sites, respectively. To determine the final site of the URL, comprehensive studies based on surface investigations, borehole drilling, and borehole testing were carried out in parallel at these nine sites. According to the site characterization results and the proposed siting criteria of the URL (Wang et al., 2018), a comparison was conducted among the nine sites. In 2016, a review meeting of senior experts for the URL site recommendation was organized by the CAEA. The result was that the Xinchang site in the Beishan pre-selected region was determined as China's URL site (Wang et al., 2018). Hence, we call China's first URL for HLW disposal as Beishan URL.

2.1.2.2 Site Characterization

The Beishan URL site is in the middle of the Xinchang granite intrusion (Fig. 2.2), which is situated in the middle of the Beishan area and has a length of 22 km and a width of 7 km. The topography of the URL site is characterized by a relatively flat landscape with small hills in the Gobi Desert (Fig. 2.3).

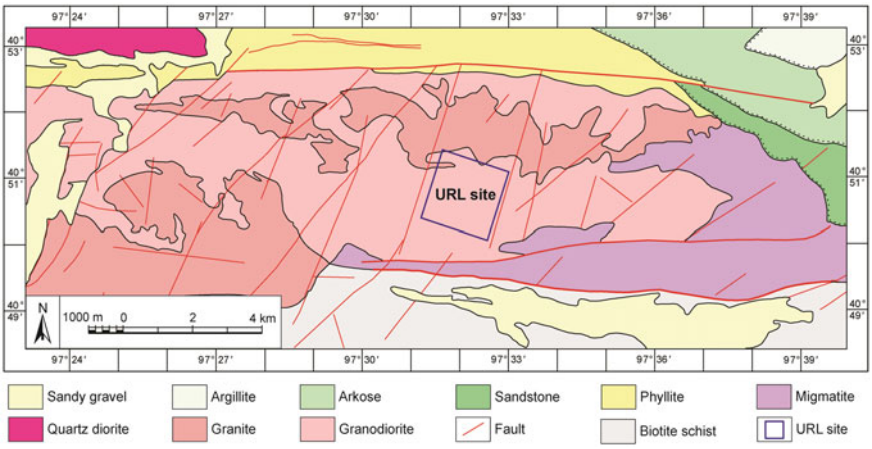

Fig. 2.2 Geological map of the Xinchang granite intrusion (Wang et al., 2018)

Fig. 2.3 Topography of the Beishan URL site

To understand geological, hydrogeological, and engineering conditions of the Beishan URL site, a series of investigations, such as geophysical surveying, borehole drilling, and hydraulic tests, have been conducted since 2015 (Wang et al., 2018). More than 30 boreholes with various depths were drilled within or around the site, and the borehole locations are shown in Fig. 2.4. In the site characterization phase of the URL, 600-m-deep vertical boreholes, i.e., boreholes BS06, BS28, BS32, and BS33,

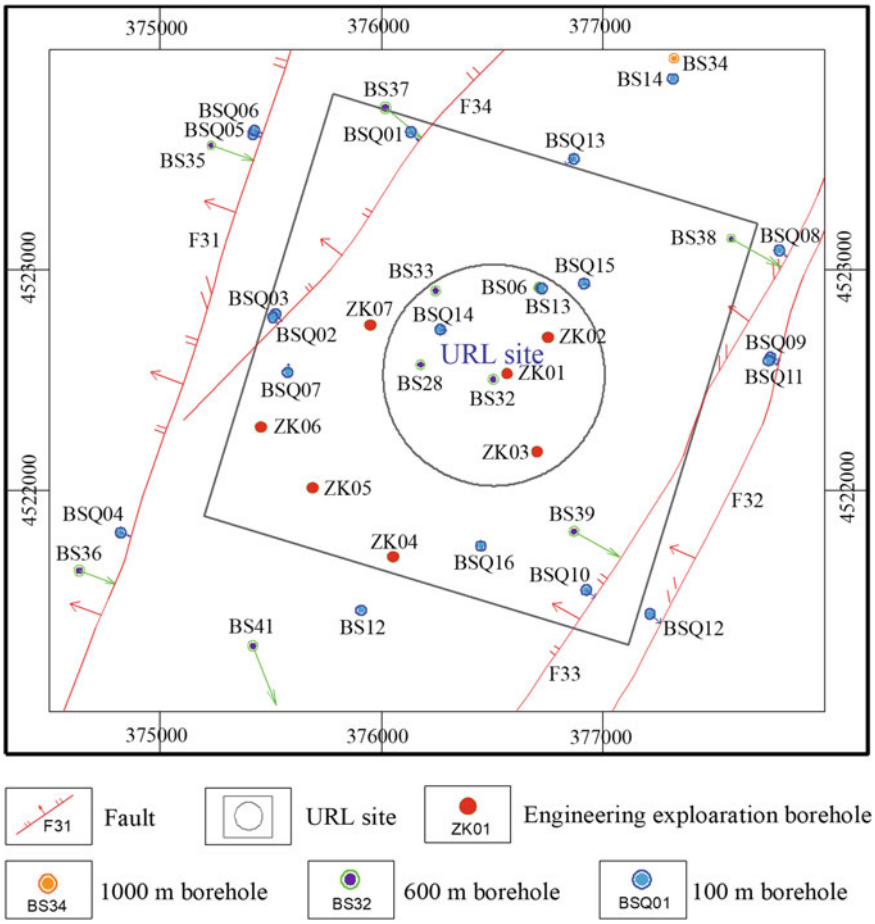

Fig. 2.4 Borehole locations at the Beishan URL site, modified from Wang et al. (2018)

were used for the exploration of geological conditions of the URL site, especially for the evaluation of rock quality or integrity. In addition, 600-m-deep and 100-m-deep inclined boreholes were used for investigating the features of the faults around the site. For example, boreholes BS38 and BSQ08 were drilled for investigating the northern section of fault F33, while boreholes BS39 and BSQ10 were used for investigating the southern section of this fault. Moreover, in the design phase of the URL, engineering exploration boreholes, i.e., boreholes numbered from ZK01 to ZK07, with a depth ranging from 400 to 600 m were drilled for further investigating the engineering geological conditions of the rock mass around the designed shafts and ramp of the URL.

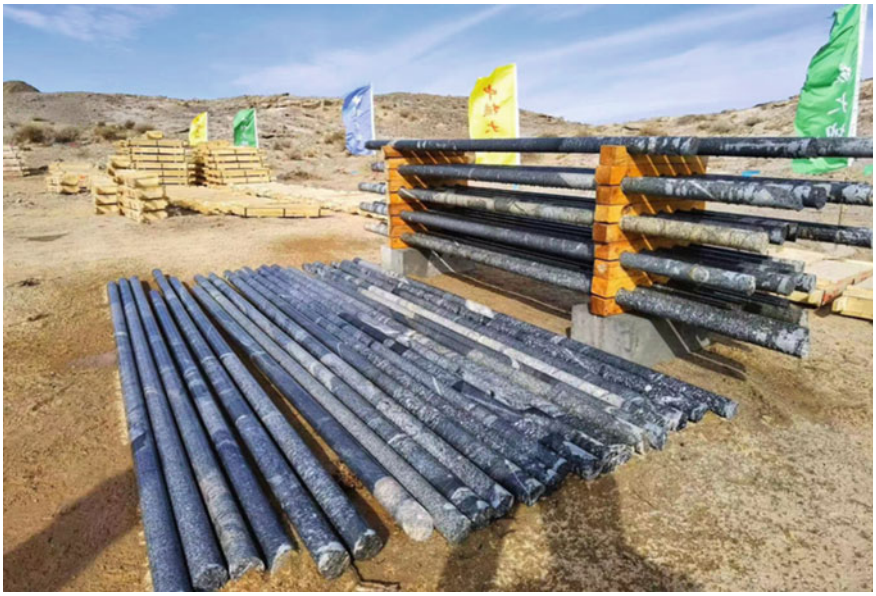

Fig. 2.5 Typical drilled cores extracted from the engineering exploration borehole ZK01

Geology

The geophysical survey results show that the granitic rocks at the URL site have a depth greater than 2 km. The rock types mainly include monzonitic granite and granodiorite (see Fig. 2.2). Meanwhile, for the drill cores of vertical boreholes, the RQD values larger than 90% accounts for 86.2% of the total drill cores (Wang et al., 2018), indicating very good integrity of rock mass at the site. In addition, the rock cores extracted from seven engineering exploration boreholes drilled in the preliminary design phase of the URL also show the extremely high integrity, as presented in Fig. 2.5. According to the investigation results, a 3D geological model of the URL site before excavation was established (Fig. 2.6) and used for site description and the optimization of the URL design. When more data are available during the URL construction, the geological model will be updated continuously.

Hydrogeology

The hydrogeological investigation results show that for all boreholes at the URL site, the water levels vary from 4 to 48 m below ground level. To evaluate the hydraulic properties of intact rocks and fracture zones, injection tests were conducted in vertical and inclined deep boreholes using a developed double packer equipment. The hydraulic conductivity (K) values in the test intervals at different depths were

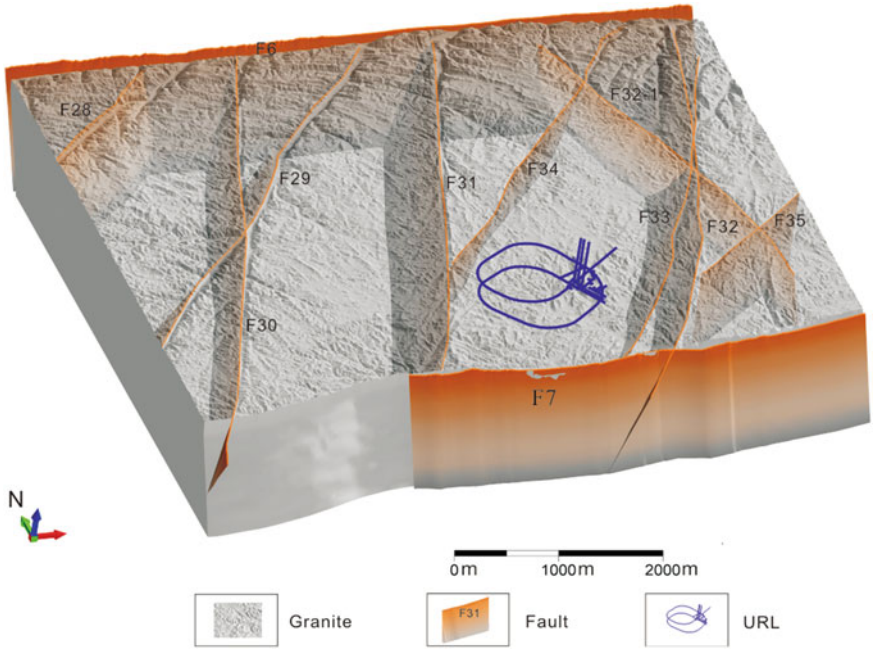

Fig. 2.6 A 3D geological model of the Beishan URL site before excavation (Wang et al., 2018)

measured. As presented in Fig. 2.7, at a shallow depth less than 50 m, the K values in several test intervals in boreholes BS32, BS35, and BS38 are larger than 10^{-7} m/s. With increasing depth, the K values start to decrease and are not sensitive to depth. For most intervals located in intact rock formations and fracture zones, the K values are less than 10^{-8} m/s and concentrate between 10^{-12} and 10^{-10} m/s (Wang et al., 2018), showing very low permeability of rock mass at the URL site. In addition, only few water-bearing fractured zones with K values ranging between 10^{-7} and 10^{-6} m/s were found in borehole BS33 at depths greater than 300 m.

Rock mechanics

Laboratory mechanical tests on rock samples, which were collected from six engineering exploration boreholes at the URL site, were carried out. The experimental results indicate that the uniaxial compressive strength (UCS) of the saturated rock samples varies from 108 to 225 MPa with an average value of 162 MPa. To provide far-field stress boundary conditions for optimization of the URL design and stability evaluation of surrounding rocks, a total of 102 hydro-fracturing in situ stress measurements were performed in five boreholes (Fig. 2.4) within the URL site at depths ranging between 60 and 600 m below the ground surface (Wang et al., 2018). The measurement results show that the in situ stresses present an increasing tend with

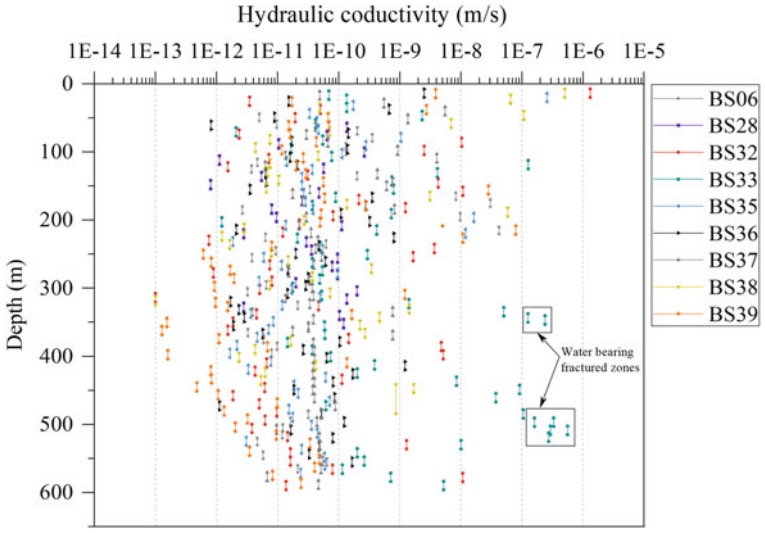

Fig. 2.7 Hydraulic conductivities of the rock masses at the Beishan URL site, modified from (Wang et al., 2018)

increasing depth, as presented in Fig. 2.8. The magnitudes of the maximum horizontal principal stress (σ_H) are all less than 25 MPa, which is at a low level compared with UCS of the core samples. Meanwhile, the measured σ_H is generally larger than the estimated vertical stress (σ_v), indicating that the in situ stress field at the Beishan underground research laboratory is dominantly controlled by the horizontal tectonic stress. In addition, fracture impression measurements show that the dominant orientation of σ_H is NEE direction with an average value of N55°E, which is in basically agreement with the orientation of crustal velocity vectors of the Beishan underground research laboratory (Zhao et al., 2013).

2.1.3 The Beishan URL Construction Project

According to site characterization results of the Beishan URL site, it is concluded that the Xinchang site is very suitable for hosting China's first URL. On May 6, 2019, the CAEA approved the "Beishan URL Construction" project. The objectives of the project are to construct a world-class URL for HLW disposal at the Xinchang site, to fill the gap in the field research and development platform for China's HLW disposal, to significantly improve China's abilities in HLW disposal technology development, and to meet China's urgent needs for R&D of HLW disposal technologies. The Beishan URL is estimated to cost over CNY 2.72 billion, and the construction period is from 2021 to 2027. A significant milestone is that on June 17, 2021, China kicked off the construction of the Beishan URL, and a ground-breaking ceremony was held

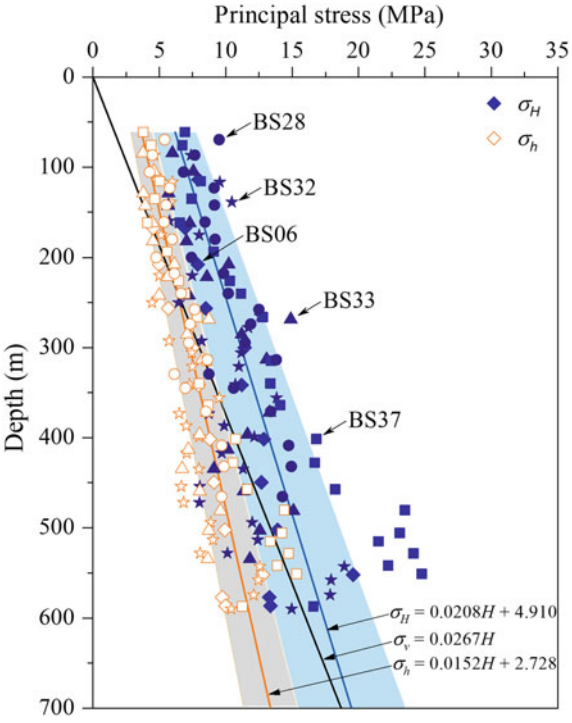

Fig. 2.8 Variation of the horizontal stresses with depth at the Beishan URL site, modified from (Wang et al., 2018)

at the URL site, marking that China's efforts on HLW disposal have entered a new phase, i.e., the URL development stage. The Beishan URL will provide an important scientific research platform for the future construction of a DGR, to speed up the process of safe disposal of HLW, and ensure the sustainable development of China's nuclear industry.

2.1.4 The Beishan URL Design and In Situ Test Plan During Its Construction

2.1.4.1 Design of the Beishan URL

Figure 2.9 presents the design of Beishan URL, which is characterized by the layout of three shafts, one spiral ramp and two experimental levels with a maximum depth of 560 m (Wang et al., 2018). The three shafts include one personnel shaft and two ventilation shafts. The conventional drill-and-blast method will be used for excavation of the 6 m diameter personnel shaft, while raise boring machine will be used for excavation of the two 3 m diameter ventilation shafts. The spiral ramp has a length of about 7 km, a cross-sectional diameter of 7 m, and a maximum curve diameter of

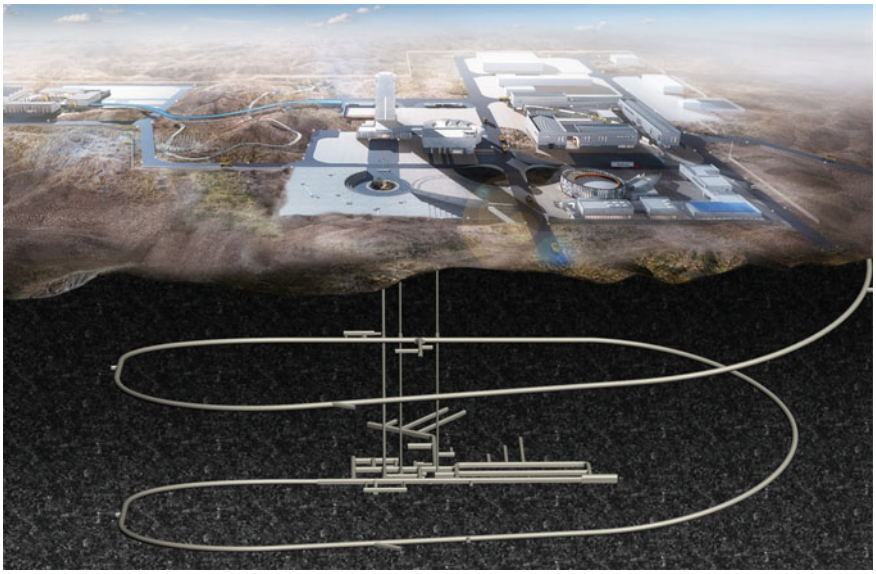

Fig. 2.9 A 3D-perspective view of the Beishan URL

about 255 m. The ramp will be excavated using the full-face tunnel boring machine (TBM), with the aim to minimize the damage to surrounding rocks. The ramp of Beishan URL is currently the world's first spiral ramp to be excavated by the TBM. The experimental tunnels will be constructed at two levels, i.e., –280 m and –560 m levels. The ramp and the three shafts are connected to the two experimental levels.

2.1.4.2 In Situ Test Plan During Beishan URL Construction

A comprehensive in situ test plan focusing on site characterization and technology development will be performed during URL construction, including geological mapping, geophysical surveying, hydrogeological investigations, rock suitability evaluation, TBM penetration test, in situ stress measurements and excavation damage zone (EDZ) characterization, etc. The test locations along the ramp and at the -560 m level are presented in Figs. 2.10 and 2.11, respectively. In parallel to the above activities, equipment to be used in the URL operation stage will be developed in surface laboratories and then tested in the two experiment levels. This includes excavation equipment for the deposition hole, installation equipment for the buffer material, and equipment for radionuclide migration testing.

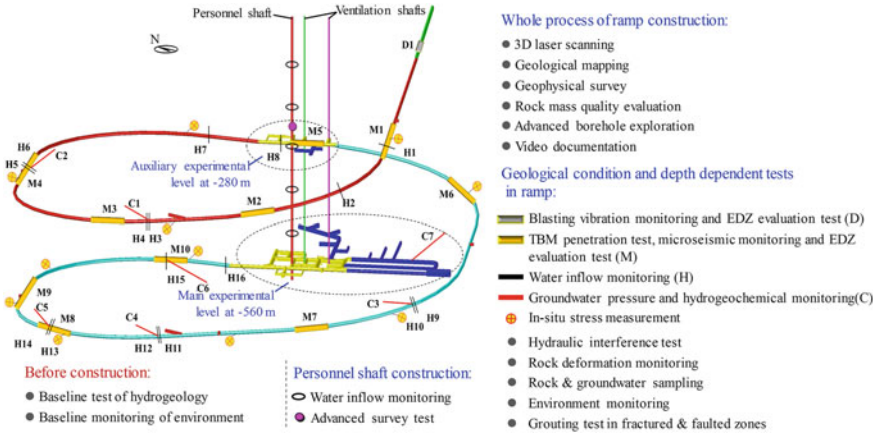

Fig. 2.10 Tests to be performed along excavation of the spiral ramp of Beishan URL

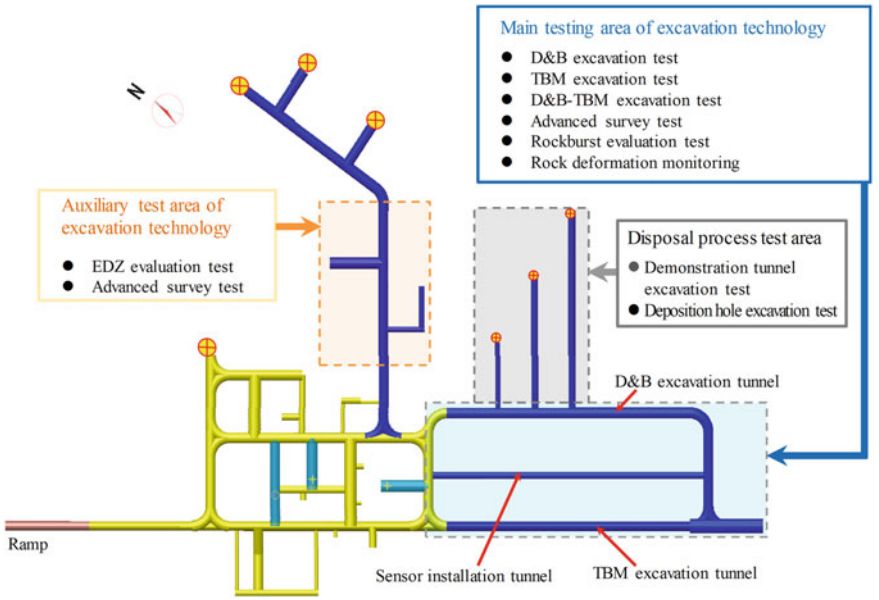

Fig. 2.11 Tests to be performed at –560 m level during construction of Beishan URL

2.1.5 The Progress of Beishan URL

The excavation of the personnel shaft and the ramp of Beishan URL started in June 2022. By the end of December 2022, the personnel shaft has been excavated to a depth of 160 m, while the ramp has been excavated to a length of 495 m by the drill-and-blast method to provide space for assembly and trial operation of the TBM.

Fig. 2.12 Very good quality of the rock mass after drill-and-blast excavation of the ramp

The quality of surrounding rocks is very good (Fig. 2.12), indicating that the good integrity of rock mass at the URL site is preliminarily verified by the excavation of the shaft and the ramp.

Fig. 2.13 The assembled TBM "Beishan No. 1" at Beishan URL

As mentioned in the aforementioned section, the ramp of Beishan URL is currently the world's first spiral ramp excavated by the TBM. In the past few years, the technical feasibility of TBM for tunneling the spiral ramp of Beishan URL has been demonstrated, and the study results show that TBM method is feasible for the Beishan URL project (Ma et al., 2020). In September 2022, the specially designed TBM "Beishan No.1" for the spiral ramp excavation was successfully manufactured at China Railway Construction Heavy Industry Co. LTD in Changsha, China. In November 2022, the TBM was transported to Beishan URL and assembled on site (Fig. 2.13). On December 30, 2022, the TBM tunneling started (Fig. 2.14). Geological and hydrogeological investigations are being conducted following the excavation process of the URL. Currently, the construction of Beishan URL is in smooth progress and coordinated well with in situ tests. It is expected that the achievements to be obtained from Beishan URL will successfully contribute to the development of China's DGR and similar facilities worldwide.

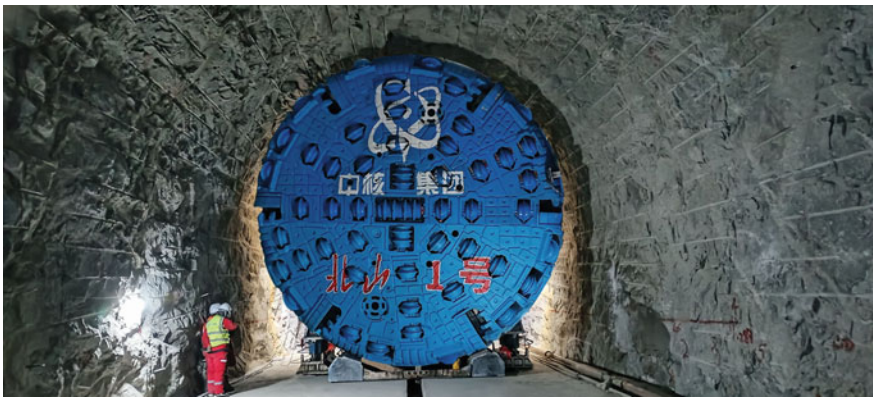

Fig. 2.14 The TBM "Beishan No. 1" in the ramp

2.2 Chinese Mock-Up Test on GMZ

Y. M. Liu, S. F. Cao, J. L. Xie, L. K. Ma

The shaft-tunnel model with a multi-barrier system located in saturated granite areas is the preliminary concept of the high-level radioactive waste (HLW) repository in China (Wang, 2010). An engineered barrier system (EBS) with buffer materials surrounding the canisters is the main part of the multi-barrier system. The Gaomiaozi (GMZ) bentonite is considered as the potential EBS buffer material, and the Beishan site as the most potential site for HLW disposal project in China (Liu and Wen, 2003).

Figure 2.15 shows the large-scale thermal-hydro-mechanical-chemical (THMC) China-Mock-Up facility. It was designed as a vertical cylindrical tank with an inner diameter of 900 mm and a height of 2200 mm, filled with compacted GMZ-bentonite. The THMC China-Mock-Up facility was built in 2010 and has been in continuous operation at the laboratory of the Beijing Research Institute of Uranium Geology (BRIUG) (Liu et al., 2013). This facility can be used to evaluate key THMC processes in the compacted GMZ-bentonite blocks during the early phase of HLW disposal system, providing a reliable database for numerical modeling and further investigations.

2.2.1 Experiment Materials

2.2.1.1 Main Properties of GMZ Bentonite

The GMZ bentonite was extracted from the Inner Mongolia autonomous region in northern China, 300 km northwest of Beijing. In this area, the reserves of bentonite

Fig. 2.15 External view of THMC China-Mock-Up facility

are about 160 $\times 10^6$ tons, and the proven reserves of Na-bentonite are about 120 million tons and the mining area is about 72 km^2. The major bentonite clay layer of the deposit extends about 8,150 m with a thickness of 8.78–20.47 m. This deposit was formed in the later Jurassic period (Liu et al., 2007).

The GMZ01 bentonite was mined from the Jiucaigou tunnel located in the east of the GMZ-bentonite deposit, and the GMZ02 bentonite from the middle area which was near the ZK2401 section of GMZ-bentonite deposit (Xie et al., 2018). The natural sodium GMZ bentonite was air dried and its moisture content after drying was about 10%.The naturally dried bentonite was crushed to 200 meshes by a Raymond mill, and some impurities with high hardness and density were removed during this process.

The previous studies have shown that the GMZ01 bentonite has ideal thermal, hydraulic, mechanical, and physico-chemical properties as a buffer material. The main thermal-hydraulic-mechanical (THM) properties of GMZ01 bentonite are summarized below.

The X-diffraction analysis showed that the clay mineralogy is dominated by montmorillonite (75±2%), which is the essential mineral for sealing performance. The GMZ01bentonite also contained varying amounts of quartz (12±1%), cristobalite (7±1%), feldspar (4±1%), calcite and kaolinite (1±1%). The high content of montmorillonite resulted in a high cation exchange capacity (CEC = 77.30 meq/100 g), a large plasticity index (I_p = 275), and a large specific surface area (a_s = 570 m^2/g) (Liu and Wen, 2003). The major exchangeable cations were Na^+ (43.6 meq/100g), Ca^{2+} (29.1 meq/100g), and Mg^{2+} (12.3 meq/100g).

The existing studies have suggested that the thermal conductivity of GMZ01 bentonite increases with the increase in dry density and moisture content. With a dry density of 2000 kg/m^3 and a moisture content of 7%, the thermal conductivity of the GMZ01 bentonite is about 1.12 W/mk (Liu and Cai, 2007). Regarding the hydraulic properties, Chen et al. (2006) obtained the water retention curve at room temperature under confined and unconfined conditions. It was found that the coefficient of unsaturated hydraulic conductivity of GMZ01 bentonite for the initial dry density of 1700 kg/m^3 varies between 1.13×10^{-13} m/s and 8.41×10^{-15} m/s during the saturation process (Ye et al., 2009a). Ye et al. (2009b) also investigated the influence of temperature on the water retention capacity of highly compacted GMZ01 bentonite. The results showed that the water retention capacity of the highly compacted GMZ bentonite decreases as the temperature increases.

The research on mechanical behaviors of GMZ01 bentonite has also been conducted. Ye et al. (2007) performed swelling pressure tests on compacted GMZ bentonite with four dry densities (1.15 g/cm^3, 1.30 kg/cm^3, 1.50 g/cm^3, and 1.75 g/cm^3) through the constant-volume method, and measured the swelling pressure (about 4.3 MPa) when the GMZ01 bentonite with a dry density of 1.75g/cm^3 (Ye et al., 2007). Based on the experimental data, the regression curve of the relationship between the swelling pressure (P_s, kPa) and dry density (ρ_d, g/cm^3) of the GMZ01 bentonite at laboratory temperature was derived: $ln\,P_s = 5.151\ \rho_d – 0.618$. In view of the limited available data, the further validation of the equation is still necessary.

Cui et al. (2011) systematically investigated the THM behavior of compacted GMZ01 bentonite. In his study, the thermal-mechanical behavior of compacted GMZ bentonite with a dry density of 1700 kg/m^3 was studied using a temperature-suction-controlled isotropic cell, and the significant effect of suction on the compressibility parameters of GMZ bentonite was verified. Based on laboratory experiments, a coupled THM model of GMZ bentonite was proposed to reproduce the main physical-mechanical behavior of GMZ bentonite. However, further validation of the model by the mock-up test and in situ test is still required.

2.2.1.2 Preparation of Compacted Bentonite Blocks and Pellets

The bentonite used for the China-Mock-Up was excavated from Jiucaigou tunnel located in the east of the GMZ-bentonite deposit. The naturally dried bentonite was crushed to 200 meshes (GMZ01, particle size less than 0.07 mm) and 80 meshes (GMZ06, particle size less than 0.18 mm) by a Raymond mill, and some impurities with high hardness and density were removed in this process. Tables 2.1 and 2.2 show the chemical compositions and mineralogical compositions of GMZ01 and GMZ06.

Table 2.1 Chemical compositions of GMZ-Na-bentonite

	Al_2O_3	SiO_2	P_2O_5	CaO	K_2O	TiO_2	FeO	TFe_2O_3	MgO	Na_2O	MnO	LOI
GMZ01	14.24	68.40	0.05	0.99	0.68	0.14	0.26	2.53	3.31	1.62	0.04	7.67
GMZ06	14.11	68.44	0.04	0.91	0.68	0.16	0.41	2.36	3.20	1.62	0.04	7.76

Table 2.2 Mineral compositions of GMZ-Na-bentonite

	Montmorillonite	Quartz	Feldspar	Cristobalite	Kaolinite	Calcite
GMZ01	73.2	8.7	7.6	9.0	0.75	0.75
GMZ06	74.0	8.9	5.8	9.0	1.53	0.76

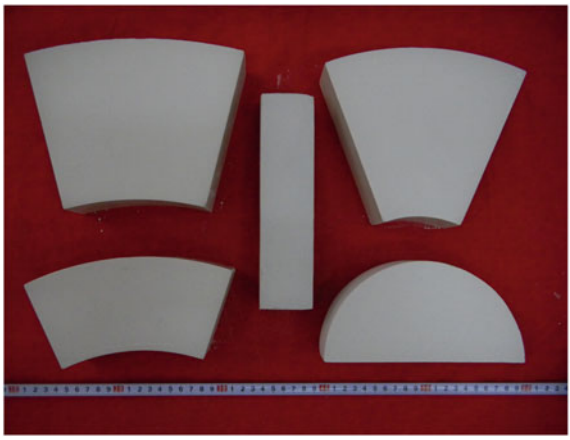

Fig. 2.16 Compacted bentonite blocks

Fig. 2.17 Crushed pellets of compacted bentonite blocks

The GMZ-bentonite powder with an average moisture content of 8.7% was compacted into high-density blocks by a computer-controlled triaxial testing machine combined with the self-designed steel molds. Totally, five types of compacted blocks were used in this test, as shown in Fig. 2.16. The GMZ06 was used to compact fan-shaped bentonite blocks, and the GMZ01 was used to compact hemicycle and rectangular bentonite blocks. The dry density of fan and hemicycle-shaped bentonite blocks was 1710 kg/m^3, and that of rectangular bentonite blocks was 1930 kg/cm^3. The rectangular bentonite blocks were subsequently crushed into small pellets with different grain sizes (see Fig. 2.17) to fill the space between bentonite blocks and

the steel tank walls. The average dry density of bentonite pellets was 1300 kg/m^3. The total mass of bentonite used in the experiment was about 2058 kg. Once the blocks have swollen and filled all the construction gaps, the dry density of bentonite decreased to an average value of about 1600 kg/cm^3.

2.2.2 Structure of China-Mock-Up Facility

The China-Mock-Up facility was constructed as a vertical cylindrical tank. The main components of the testing system were as follows (see Fig. 2.18): a steel tank, a central electrical heater with a temperature control system, a hydration system, an engineered barrier, sensors, a gas measurement and collection system, and a Data Acquisition System (DAS). The steel tank was used to simulate the vertical disposal pit with an inner diameter of 900 mm and a height of 2200 mm. A layer of geotextile was placed between the tank and bentonite. The gaps between the tank and the bentonite blocks were filled with crushed pellets.

The heater in the China-Mock-Up was made of 1-ton carbon steel with a diameter of 300 mm and a height of 1600 mm. It only simulated the thermal emission, dimensions, and weight of the reference canister. The weight pressure of the heater was 1.24 MPa, and the temperature of the heater was automatically controlled by a temperature-monitoring system.

The hydration system was employed to simulate the water penetration from the host rock. In the hydration system, the water supply to the barrier was realized by four vertical tubes (∅ 10 mm) installed on the interior boundary of the cylindrical tank. As presented in Fig. 2.18, the water tank was connected to the injection tubes and an argon tank in the experiment. By controlling the gas pressure in the argon tank, the water was injected from the bottom of the mock-up facility. Simultaneously, the injection rate was measured by a mass flowmeter, and the water sample tank was weighted constantly by a mass balance to quantify the injected water mass. Table 2.3 shows the main chemical compositions of water from borehole BS05 of the Beishan site used in the hydration system.

The engineered barrier was composed of compacted GMZ-bentonite blocks and pellets surrounding the heater. The blocks were arranged in 44 sections: 32 sections were set in two concentric rings around the heater and the left 12 sections in two rings and a core. Bentonite pellets and bentonite powder were filled in the installation space between the heater and the bentonite block, or steel tank.

More than 160 sensors, including the temperature, relative humidity (RH), stress, and displacement, were installed inside and outside the facility to monitor the evolution of bentonite and heater. The inside sensors were distributed in bentonite blocks and pellets in 7 sections (sections I–VII) vertically. Different types of sensors were placed within each section to investigate the temperature change, hydration process, and the behavior of buffer materials under complex coupling conditions. Table 2.4 lists the sensors installed in the mock-up test and associated parameters. The sen-

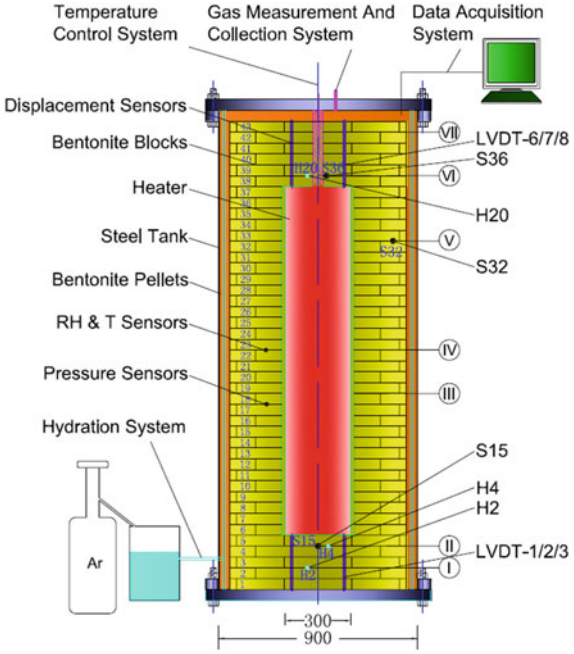

Fig. 2.18 General layout of the china-mock-up facility

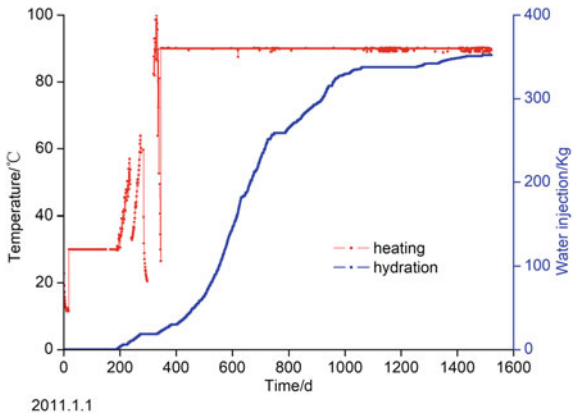

Fig. 2.19 Temperature and water consumption with time

Table 2.3 Chemical compositions of underground water from Beishan (unit: mg/L)

F^-	Cl^-	NO_3^-	SO_4^{2-}	CO_3^{2-}	HCO_3^-	Na^+	K^+	Mg^{2+}	Ca^{2+}
4.18	771	8.64	718	92.3	0.600	798	4.80	31.4	177

sors were placed within the grooves cut in the compacted bentonite blocks or in the surrounding pellets.

Table 2.4 Summary of the sensors installed in the mock-up test

Measured parameter	Sensors' type	Measured principal	IN*	B**	S***
Temperature	JCJ100AW	Pt100	28	2	2
Room temperature	JCJ100AW	Pt100			2
Total pressure	CYG-1712	Wheatstone bridge	37		
Pore water pressure	CYG-1715	Wheatstone bridge	8		
Relative humidity	HC2-C04	Capacitance	24		4
Displacement	HTGGA-20	Magnetic transfer	6		
Injection water volume	DMF-1-1-A	Faraday's law of electromagnetic induction			2
Container strain	JC-4A/BE120-5AA	Resistance strain effect			30
Strain and temperature	FSS1312DS	Resistance strain effect+Pt100			20
Metal corrosion	Custom-made	Alternating current impedance	10		
Total number			113	2	60

IN*—installation number, B**—Bentonite, S***—Structure

2.2.3 Test Procedures

The China-Mock-Up facility was assembled completely on September 10, 2010. The data acquisition and monitoring system automatically recorded all the measurement data every 10–30 min from January 1, 2011. In the data recording, January 1, 2011 was identified as Day 0 on the time scale after pre-operation.

On January 19, 2011, the heater was switched on and the temperature of the heater reached 30°C and remained constant. From Day 188 to Day 400, the temperature raised to 90°C gradually at a speed of 1°C/d. Finally, the constant temperature control mode was automatically activated by the computer, maintaining a temperature of 90°C. Figure 2.19 shows the heating phase with time.

The real THMC experiment with the water injection began on July 8, 2011 (Day 188). The water injection rate was gradually increased from 400 g/day to 1500 g/day, and the water injection rate was controlled artificially to avoid potential damage to the sensors by the rapid saturation in the first stage. From August 25, 2013 (Day 967),

the water injection pressure was gradually controlled from 0.2 MPa to 1 MPa. Figure 2.19 illustrates the water consumption with the time. To be mentioned here, there were no water supplies artificially sometimes due to holidays and some maintenance.

2.2.4 Analysis of Experimental Data

The sensors placed in the bentonite provided reasonable and consistent outputs. In this report, the experimental results recorded from January 1, 2011 to December 31, 2015 are analyzed, including the temperature change, relative humidity (RH), the stress in the bentonite, and heater displacement.

2.2.4.1 Temperature Evolution

There are four temperature sensors installed in each measurement profile. The measurement range of temperature sensor is from 0 to 300°C, with an accuracy of 0.1 °C. Figure 2.20 presents the temperature evolution in bentonite in sections II, III, V, and VI. It can be noticed that the temperature continuously increases with time at the first stage of temperature increase (30 °C– 90 °C). The trends of the temperature change also vary with the four seasons of environmental conditions. Moreover, the distribution of temperature is non-uniform vertically, and the temperature is much higher in the central part. Even in section V, the temperature is still below 70°C. In the experiment, the lower temperature can be partly attributed to the existence of installation space between the heater and compacted GMZ blocks, which is 5cm in width and filled with pellets. This installation method may reduce the thermal conductivity of the barrier in the area. In addition, the effective heating length in the center of the heater with a height of 1.6 m is only 1.2 m.

This is an important factor causing the higher temperature in the central part of the barrier. Besides, the temperature distribution is also influenced by a complex coupling mechanism. Considering that the saturation changes thermal conductivity, the temperature distribution also depends on the saturation process in the compacted bentonite. Due to the interruptions of the electric power supply, some fluctuations of temperature are also recorded.

Figure 2.21 shows the temperature distribution in the China-Mock-Up facility on July 8, 2012.

2.2.4.2 Relative Humidity (RH)

A total of 24 RH sensors are placed into holes drilled into the bentonite blocks at seven sections (sections I–VII) vertically. The RH and temperature in the bentonite can be measured by the RH sensors. Figure 2.22 shows the RH and temperature evolution in bentonite at sections II, III, V, and VII.

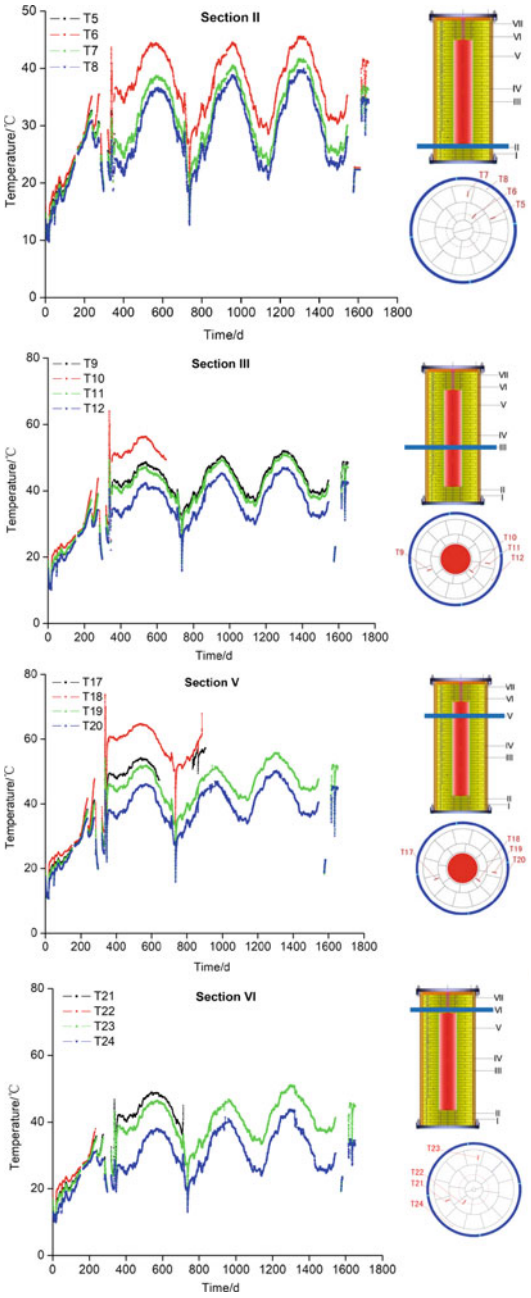

Fig. 2.20 Temperature evolution in sections II, III, V, and VI

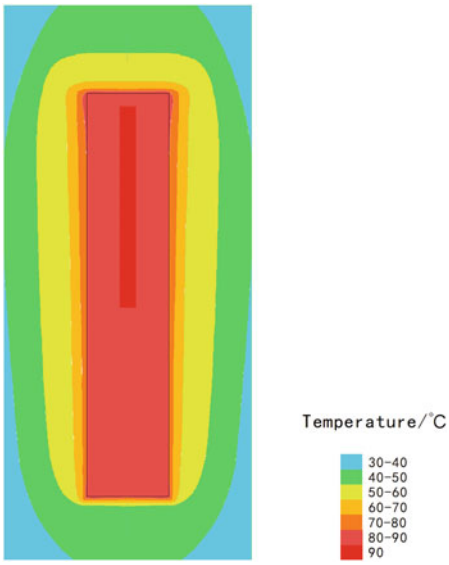

Fig. 2.21 Temperature distribution in the China-Mock-Up on July 8, 2012

As illustrated in the figures, the compacted bentonite is progressively saturated from section I to section VII, and the distance to the heater has a significant influence on the saturation velocity. Due to the temperature fluctuation, there are also some fluctuations in the RH evolution. The heating process generally leads to the increase of RH, which is probably related to the generation of the vapor phase.

The RH evolution in sections III and V are much more complex. With the increase of temperature, the bentonite near the heater has a decrease in RH due to the drying effect of the heater, particularly in the inner rings (H10, H16, and H18). In the inner part, the following stages can be noticed: (a) the stable RH stage: there is a stable RH stage with some fluctuations; (b) the decreased RH stage: when the temperature is kept at 90°C, continuous heat transfer from the heater leads to the drying effect, and then RH decreases; (c) the increased RH stage: with the increase of water injection rate, hydration gradually overcomes the drying effect and then the RH increases. This wetting tendency is tightly related to the accelerated saturation process caused by the increased water injection rate. On the contrary, the desiccation is not noticed (H7 and H15) in the outer part where the drying effect is insignificant. This findings are consistent with the previous results obtained by Villar et al. (2012).

Due to the non-uniform water supply in the vertical direction, the saturation process in section VII is less significant than that in section II at the bottom. The desiccation phenomenon was also observed from the sensor H22 located in the inner ring. In addition, the fluctuation of RH induced by the heating interruptions is particularly evident in section VII. It indicates that the generated vapor phase moves in both radial and longitudinal directions.

In conclusion, the RH variation in the inner rings is the result of the drying effect of the heater and the water penetration. The experimental results indicate that, due to

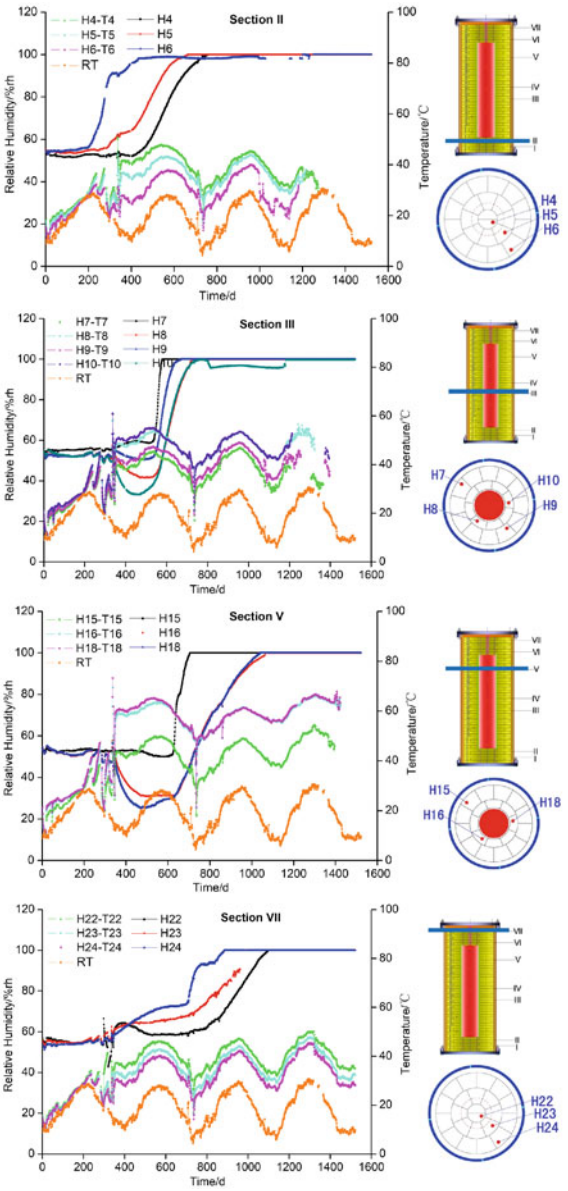

Fig. 2.22 RH and temperature evolution in sections II, III, V, and VII

the low permeability of the compacted bentonite, the drying effect was dominant in these sections at the beginning of the test. This finding is consistent with the results reported in other research works (Villar et al., 2012).

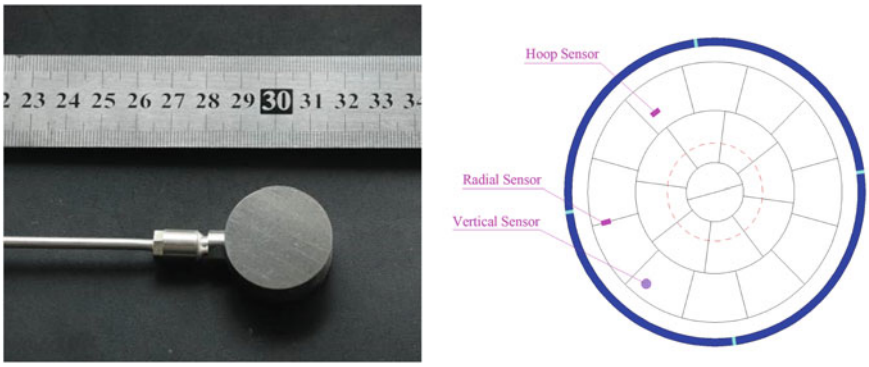

Fig. 2.23 Stress sensor and its location in the compacted bentonite

2.2.4.3 Stress Evolution

The swelling stress was measured by stress sensors installed in two or three different directions, i.e., x-, y-, and z-directions in each measurement profiles. Moreover, there were another three stress sensors directly contacting the inner top, bottom, and side walls of the steel tank, respectively. The CYG-1712 stress sensors were used, and its measurement principle was the Wheatstone bridge from SQSENSER (China). The stress sensor was capable of withstanding temperatures up to +100 °C with a stress measurement ranging from 0 to 20 MPa, as shown in Fig. 2.23. The sensors were placed within the grooves cut in the compacted bentonite blocks in three directions, including vertical, radial, and hoop directions.

(1) Total pressure evolution

Under the THMC-coupled condition, the stress evolution in the compacted bentonite can be influenced by several factors, including gravity, the thermal expansion induced by high temperature, and the swelling pressure generated by bentonite saturation with water penetration.

Figure 2.24 shows the stress evolution in bentonite at sections II, III, VI and VII. It can be seen that the variation of the total stress is rather limited or negligible in the initial stage, which is caused by the initial gaps between sensors and blocks, and bentonite blocks and pellets. The stress inside the bentonite increases from the bottom to the top and from the area near the water tube to the interior gradually. After more than 2 years of water injection, the stress in the inner part increases quickly, and becomes higher than the outer part gradually. This indicates the water seeps into the inner part.

The highest vertical stress of 3.8 MPa is recorded by sensor 36 in the middle of section VI located on the top of the heater after 1512 days. At the bottom of the heater, the highest vertical stress of 2.3 MPa is also recorded by sensor 15 in section II after 1512 days. The swelling pressure of GMZ bentonite tested by this facility

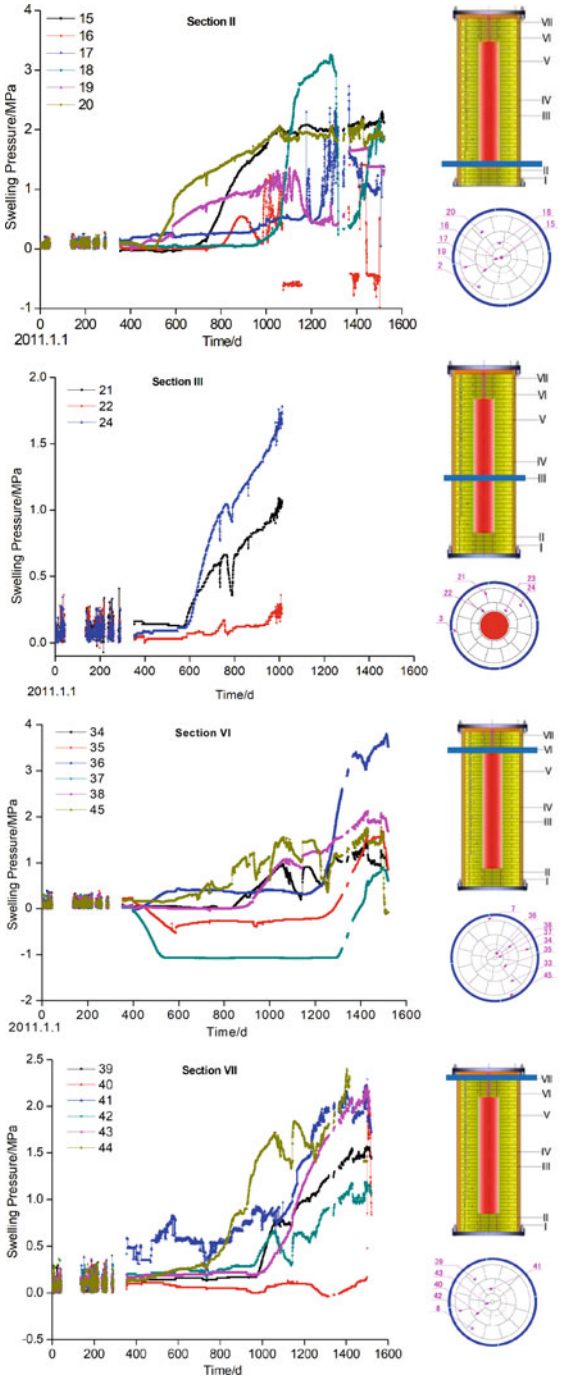

Fig. 2.24 Stress evolution at sections II, III, VI, and VII of China-Mock-up

is 3.8 MPa, while the conventional swelling pressure under the dry density of 1600 kg/m^3 is 3.17MPa. This can be explained as follows: as the heater moves up by 7.57 mm, the gap between the bentonite blocks as well as the gap between the sensor and the blocks at the top of the heater is squeezed, indirectly leading to the increase of local dry density of bentonite. Besides, the thermal expansion of the heater may be another reason.

In the higher level of bentonite blocks above the heater, the highest vertical stress of 2.4 MPa is recorded by sensor 44 in section VII after 1403 days. This can be explained as follows: the saturation process of whole barrier has not finished yet; stress release is induced by the initial gaps between the bentonite blocks and pellets, and the gaps between the sensors and the blocks.

The highest hoop stress of 3.26 MPa is recorded by sensor 18 within the inner ring in section II located on the bottom of the heater after 1284 days. The highest radical stress of 2.73 MPa is recorded by sensor 17 within the inner ring in section II located on the bottom of the heater after 1365 days. The highest radical stress is lower than the vertical stress and the hoop stress.

(2) Stress distribution

According to the data of the stress sensor in three directions, the stress distribution on July 8, 2012 (1 year after operation) is obtained, as shown in Fig. 2.25. After the water injection, water is concentrated at the bottom due to the gravity effect, and the initial gaps between bentonite and steel tank, and bentonite and heater. Besides, the saturation process is vertically non-uniform which brings difficulties to the definition of boundary condition in numerical studies. Because of the low hydration rate and inhomogeneous saturation process in the vertical direction, the stress variation is relatively limited and inhomogeneous. The stress is higher at the bottom of the heater which may be related to the gravity of the heater. Since the mass of the heater is 1000 kg, the pressure under the heater by its weight is 1.24 MPa, and the radical stress and hoop stress around the heater are lower, indicating that water has not penetrated to the inner part of the bentonite.

The stress distribution on October 8, 2013 (2 years after the operation) is obtained, as shown in Fig. 2.25. The maximum stress in the area below the heater may be due to the gravity effect of the heater itself, as well as the full penetration of water in the bottom area of the facility, resulting in the maximum stress. The stress around the heater is lower, which may be due to the stress release caused by the initial gaps between the bentonite blocks and pellets with the heater and steel tank, and the gaps between the sensors and blocks. It also indicates that the water has not penetrated to the bentonite near the heater (the bentonite has very low permeability and a long time is required for water to seep into the inner parts).

The stress distribution on July 8, 2014 (more than 3 years after operation) is shown in Fig. 2.25. It indicates that bentonite at the bottom of the heater is nearly saturated. The stress is still higher at the bottom of the heater due to the gravity. The lower dry density of the bentonite pellets results in low radical stress and hoop stress near the steel tank and heater.

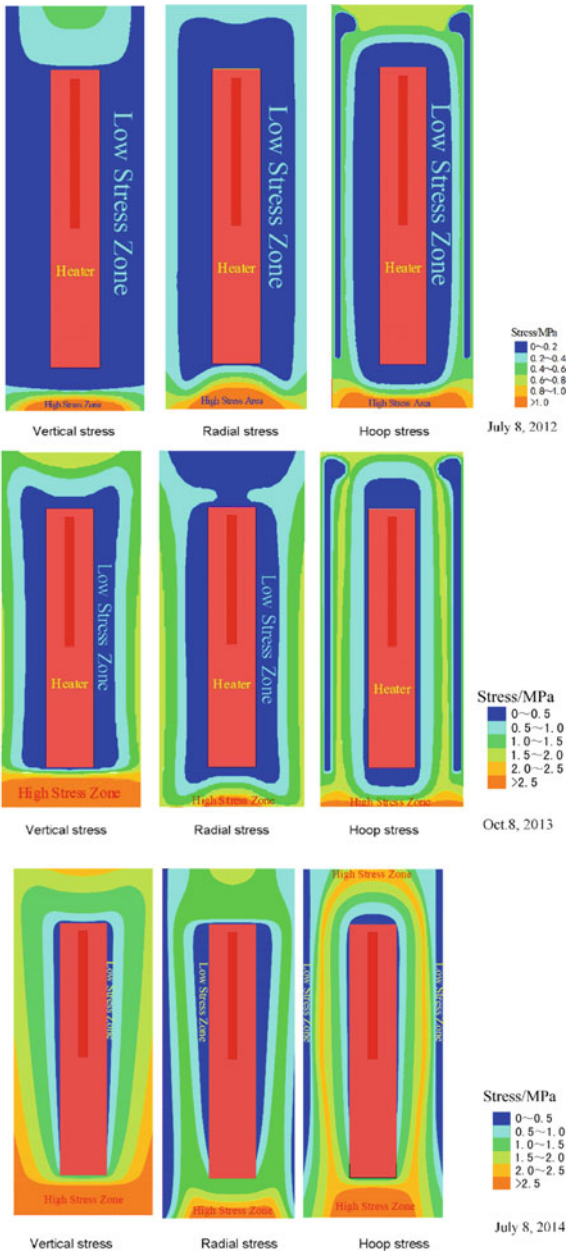

Fig. 2.25 Stress distribution in the China-Mock-Up on July 8, 2012 (top), October 8, 2013 (mid), July 8, 2012 (bottom)

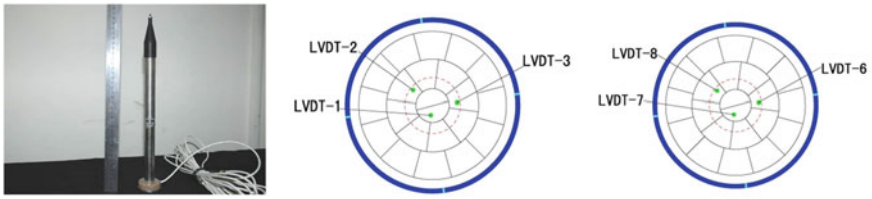

Fig. 2.26 Displacement sensor and its location in measuring sections

2.2.4.4 Displacement Evolution of Heater

According to the reference concept for HLW disposal in China, the canister is completely supported by the surrounding buffer material. Therefore, the mechanical performance of buffer material may affect the overall stability of the canister. To evaluate this potential influence, six LVDT sensors were installed on the top and bottom of the heater to monitor its vertical displacement.

As shown in Fig. 2.26, the Linear Variable Differential Transformer (LVDT) sensors HTGGA-20 from KING SENSOR (China) are used. The selected displacement sensor has a fairly small size, which can reduce the interference to the whole system as much as possible. The lengths of LVDT sensors at the bottom and top of the heater are 250 mm and 300 mm, respectively. The measuring range of the displacement sensor is ±20 mm and the accuracy is more than 0.1%. The diameter of the main part of the LVDT sensor is 22 mm. The LVDT sensors were specifically constructed of steel 316L with a rubber sleeve on top to improve its corrosion resistance and water tightness.

Figure 2.27 shows the vertical displacements measured by six LVDT sensors. The positive value recorded by the LVDT6 to LVDT8 indicates that the sensor is in the compression state and the heater moves upward. The negative value recorded by the LVDT1 to LVDT3 indicates that the sensor is in the tensile state and the heater moves upward. Because the electric components of the LVDT6–LVDT8 sensors were directly connected to the heater, coupled with the THMC harsh environment, LVDT6–LVDT8 failed one after another after water injection and the temperature of the heater gradually reached 90°C.

Four phases of movement evolution of the heater can be observed: (a) phase I: the heater moves downward and upward slowly with a maximum downward displacement of 0.06 mm and a maximum upward displacement of 0.29 mm in 188 days; (b) phase II: when the water injection begins, and the heater temperature increases to 90°C in 346 days, the heater moves upward 2.6 mm quickly; (c) phase III: when the temperature is kept at 90°C with continuous water injection, the heater moves upward continuously, while the movement rate gradually decreases to a stable displacement of 5.6 mm with some fluctuations in 730 days; and (d) phase IV: the heater moves upward slowly again with the progress of water injection. A maximum upward displacement of the heater (8.64 mm) is recorded by LVDT3 at day 1590. The six LVDT sensors obtained similar data in different directions from phase I to phase III. The

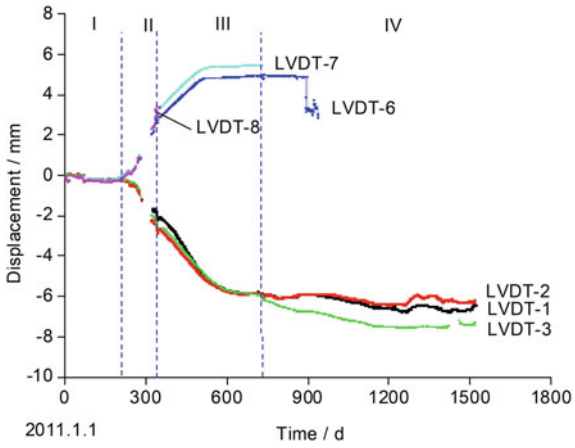

Fig. 2.27 Displacement evolution of the heater

difference between LVDT6 and LVDT7 maybe caused by the bentonite penetration into the gap between the steel plate screwing the LVDT6 to LVDT8 and the top lid of the steel tank. The difference among LVDT1, LVDT2, and LVDT3 maybe caused by the bentonite penetration into the gap between the steel plate screwing the LVDT1 to LVDT3 and the bottom of the heater. The penetration point of bentonite is probably near the LVDT6, LVDT1, and LVDT2, respectively.

The heater is completely supported by the compacted bentonite in China-Mock-Up. Therefore, the mechanical performance of compacted bentonite may affect the movement evolution of the heater. When the weight and load of the heater are 1 ton and 1.24 MPa, the compacted bentonite under the heater is consolidated and subject to volumetric/deviatoric creep. During the heating, the thermal expansion of the heater and bentonite occurs. The swelling of bentonite may be the main cause of the upward movement of the heater.

Note: The positive value indicates that the LVDT is in the compressed state, and the negative value indicates that the LVDT is in the tensile state.

(1) Effect of Temperature and RH on the Heater Displacement

The temperature of heater and the evolution of compacted bentonite recorded by different sensors indicate that the displacement of the heater is directly related to the evolution of temperature and RH in bentonite (Fig. 2.28). RH sensors (H2 and H4) are located in the bentonite blocks at sections I and II under the heater, respectively. The RH sensor of H20 is located in the bentonite block at section VI above the heater.

In phase I, when the temperature increases to 30°C and remains constant, the heater moves upward slightly and remains stable with some fluctuations due to the thermal expansion on the heater and bentonite.

In phase II, when the temperature increases to 90°C gradually, the heater moves upward quickly because of the continuous thermal expansion of heater and bentonite. The slow increase in RH can be observed by the RH sensor of H2. This suggests

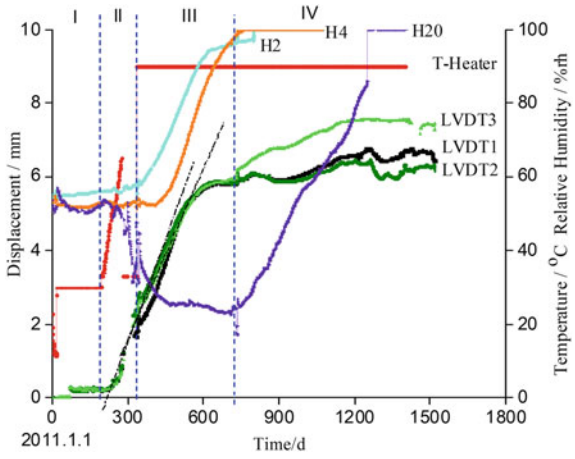

Fig. 2.28 Displacement evolution of the heater with temperature and RH in the bentonite

that the bentonite under the heater is wet and the swelling of the bentonite occurs. The decrease of RH can be observed by RH sensor of H20. It can be seen that heat transferred from the heater leads to the drying effect on the bentonite above the heater and the volume of the bentonite may be reduced.

In phase III, the temperature is kept at 90°C, and the rapid increase of RH is observed by RH sensors of H2 and H4. It suggests that the bentonite under the heater is wet and swelling quickly. The displacement curves have the same trend with the RH curves of H2. As the bentonite under the heater becomes saturated, the heater gradually stops moving upward. The decrease of RH can be observed by the RH sensor of H20. It indicates that the bentonite above the heater is dried constantly. The upward movement of the heater at phase III is mainly caused by the swelling of bentonite under the heater.

In the phase IV, the rapid increase of RH can be observed by the RH sensor of H20 after 700 days, indicating that the bentonite above the heater is wet and swells quickly. Because the total mass of bentonite in the test tank remains unchanged and the volume of the bentonite above the heater swells, the bentonite above the heater pushes the bentonite around the heater to the bottom of the heater and induces the upward movement of the heater again.

(2) Effect of Stress in Bentonite on the Heater Displacement

Figure 2.29 shows the displacement evolution of the heater with the stress change in bentonite. Stress sensor S15 is placed under the heater in section II. Stress sensor S36 is placed above the heater at section VI. Stress sensor S32 is placed around the heater in hoop direction at section V. A possible reason is that the bentonite under heater might be consolidated and has volumetric/deviatoric creep under the load of 1.24 MPa caused by the self-weight of the heater.

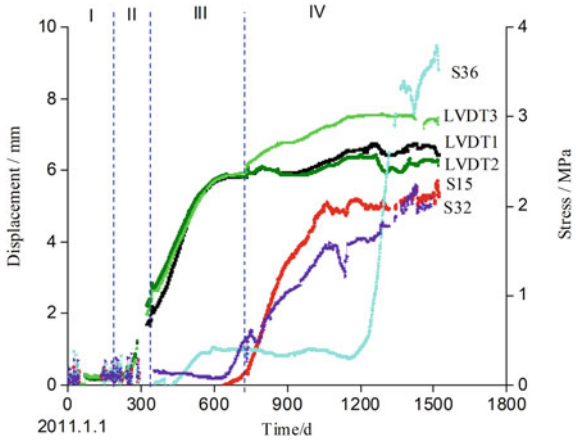

Fig. 2.29 Displacement evolution of the heater and stress in the bentonite blocks

In phase I, a maximum downward displacement of the heater (0.06 mm) is recorded at day 46. A possible reason is that the bentonite under heater might be consolidated and has volumetric/deviatoric creep under the load of 1.24 MPa caused by the self-weight of the heater.

In phase II, the stress recorded by S15 located in section II under the heater and the stress recorded by S36 located in section VI above the heater increase slightly with some fluctuations. The upward movement of the heater at phase II is partly caused by the bentonite swelling.

In phases III and IV, the stress recorded by S15 indicates that the stress in bentonite under the heater increases quickly from Day 700 to Day 1060. After that, the stress is kept at 2 MPa with a fluctuation. The stress recorded by S32 which is located in section V around the heater increases quickly from Day 646 to Day 1426. This is because the location of S32 is near the water tube than S15 and S36. Based on the stress and RH, it is deduced that the bentonite under the heater is saturated after Day 1060. The stress under the heater adjusts with the stress increase around the heater and the weight of heater. After Day 700, the heater moves upward slowly again with the saturation of bentonite under the heater and around the heater. The data fluctuation of LVDT1 and LVDT2 has the same trend as that of stress sensors S15 and S32.

The stress recorded by S36 increases during phase III, then fluctuates and increases quickly after 1200 days. This indicates that the heater moves upward and induces increased pressure in the bentonite above heater. The stress fluctuates with the heater movement. The stress above the heater exceeds the stress under the heater after 1296 days, then the stress above the heater pushes the heater to move downward. With the downward movement of the heater, the stress above the heater decreases. As the water penetrates to bentonite and the bentonite swells continuously, the stress in the bentonite increases again. The bentonite above the heater pushes the bentonite around the heater to the bottom of the heater and induces the upward movement of the heater again. The fluctuation of LVDT3 has the same trend as the stress sensor

S36 after 1296 days. A maximum upward displacement of the heater (8.64 mm) is recorded after 1590 days. With the saturation of bentonite and stress redistribution in bentonite, the heater remains stable with a minor fluctuation. Therefore, the upward movement and fluctuation of the heater at phase IV are mainly caused by the bentonite swelling and stress redistribution.

After the bentonite in the disposal pit is fully saturated, the canisters may move downward due to the weight of canisters as phase I. However, with the in situ stress, the canisters probably remain stable with a minor fluctuation. More tests about the movement of canisters in the disposal pit should be conducted in the future.

2.2.5 Summary

As a large-scale mock-up facility, the China-Mock-Up was used to investigate the THMC behavior of GMZ bentonite based on a preliminary concept of the HLW repository in China. This facility was built in 2010 and has been operated continually in the laboratory of BRIUG. Through the China-Mock-Up test, a large number of data about the evolution of compacted bentonite and the suitability evaluation of buffer material under THMC-coupled conditions have been obtained for the first time. Based on the currently recorded results, several preliminary conclusions can be drawn as follows:

(1) The temperature within the bentonite increases and varies with time and environmental conditions. Considering that the saturation process may change the thermal conductivity, the temperature distribution is influenced by the coupling mechanism between the thermal conduction and the saturation process in the mock-up test.

(2) The saturation process of the compacted bentonite is strongly influenced by the drying effect of the heater and the wetting effect of the water penetration. The bentonite has a low permeability, and a long time is required for water to penetrate into the inner parts. The RH fluctuations are generated by a complex mechanism, including saturation process, vapor generation and drying effect. Prior to 1600 days, the relative humidity of all RH sensors in the bentonite is 100%.

(3) The stress evolution in the compacted bentonite is affected by the gravity of heater and water, the thermal expansion induced by high temperature, the swelling pressure of bentonite generated by water penetration, stress release induced by the initial gaps between the bentonite blocks and pellets, the gaps between the sensors and the blocks, and also the upward displacement of the heater. The highest vertical stress of 3.8 MPa is recorded in the middle of section VI located on the top of heater after 1512 days. The highest hoop stress of 3.26 MPa and radical stress of 2.73 MPa are recorded within the inner ring in section II located at the bottom of heater after 1284 days and 1365 days, separately.

(4) The movement evolution of heater is affected by the consolidation and volumetric/deviatoric creep under the load of 1.24 MPa caused by the self-weight of the heater, the thermal expansion of heater and bentonite, the swelling of bentonite under the heater, around the heater, and above the heater in turn. A maximum

downward displacement (0.06 mm) and upward displacement (8.64 mm) of the heater are recorded on Days 46 and 1590. With the saturation and stress redistribution of bentonite, the heater remains stable with a minor fluctuation.

Based on the analysis of the existing experimental data, it is considered that the China-Mock-Up test is a valuable data source for improving the understanding of the THM process in EBS, and establishing the reliable numerical method for predicting the long-term THM-coupled behavior of EBS. With the progress of the experiment, the conclusions will be further examined and refined.

References

Ahn, J., & Apted, M. (2010). *Geological repository systems for safe disposal of spent nuclear fuels and radioactive waste*. Cambridge, UK: Woodhead Publishing Limited.

CAEA, C. A. E. A. (2006). *R&d guidelines for the geological disposal of high-level radioactive waste in China*. Beijing, China: CAEA Technical report.

Chen, B., Qian, L., Ye, W., Cui, Y. J., & Wang, J. (2006). Soil-water characteristic curves of Gaomiaozi bentonite. *Chinese Journal of Rock Mechanics and Engineering, 25*(4), 1054–1058.

Chen, B., Chen, J. Q., & Cao, Y. C. (2012). Influence of joint on self-sealing behavior of highly compacted bentonite in engineering barrier. *Chinese Journal of Rock Mechanics and Engineering, 31*(3), 618–624.

Cui, Y., Tang, A., Qian, L., Ye, W., & Chen, B. (2011). Thermal-mechanical behavior of compacted GMZ bentonite. *Soils and Foundations, 51*(6), 1065–1074.

Ju, W., Liang, C., Rui, S., & Xingguang, Z. (2018). The Beishan underground research laboratory for geological disposal of high-level radioactive waste in china: Planning, site selection, site characterization and in situ tests. *Journal of Rock Mechanics and Geotechnical Engineering,10*(3), 411–435.

Liu, Y., & Cai, M. (2007). Thermal conductivity of buffer material for high-level waste disposal (in Chinese). *Chinese Journal of Rock Mechanics and Engineering, 26*(S2), 3891–3896.

Liu, Y., & Wen, Z. (2003). Study on clay-based materials for the repository of high level radioactive waste (in Chinese). *Journal of Mineralogy and Petrology, 23*(4), 42–45.

Liu, Y., Cai, M., & Wang, J. (2007). Compressibility of buffer material for HLW disposal in China (in Chinese). *Uranium Geology, 23*, 91–95.

Liu, Y., Wang, J., Cao, S. F., Ma, L. K., Xie, J. L., & Zhao, X. G. (2013). A large-scale THMC experiment of buffer material for geological disposal of high level radioactive waste in China. *Rock and Soil Mechanics, 34*(10), 2756–2762.

Ma, H., Wang, J., Man, K., Chen, L., & Gong, Q. (2020). Excavation of underground research laboratory ramp in granite using tunnel boring machine: Feasibility study. *Journal of Rock Mechanics and Geotechnical Engineering, 12*(6), 1201–1213.

Villar, M., Martín, P., Bárcena, I., García-Siñeriz, J., Gómez-Espina, R., & Lloret, A. (2012). Long-term experimental evidences of saturation of compacted bentonite under repository conditions. *Engineering Geology, 149–150*, 57–69.

Wang, J. (2010). High-level radioactive waste disposal in China: Update 2010. *Journal of Rock Mechanics and Geotechnical Engineering, 2*(1), 1–11.

Wang, J. (2014). On area-specific underground research laboratory for geological disposal of high level radioactive waste in China. *Journal of Rock Mechanics and Geotechnical Engineering, 6*(2), 99–104.

Wang, J., Chen, L., Su, R., & Zhao, X. G. (2018). The Beishan underground research laboratory for geological disposal of high-level radioactive waste in China: Planning, site selection, site

characterization and in situ tests. *Journal of Rock Mechanics and Geotechnical Engineering, 10*(3), 411–435.

Xie, J., Cao, S., Gao, Y., Ma, L., & Liu, Y. (2018). Exploration of Gaomiaozi bentonite deposit and excavation of natural sodium bentonite (in Chinese). *China Mining Magazine, 140*, 125–129.

Ye, W.-M., Schanz, T., Lixin, Q., Wang, J., & Arifin, Y. (2007). Characteristics of swelling pressure of densely compacted Gaomiaozi bentonite GMZ01 (in Chinese). *Yanshilixue Yu Gongcheng Xuebao/Chinese Journal of Rock Mechanics and Engineering, 26*, 3861–3865.

Ye, W., Cui, Y., Qian, L., & Chen, B. (2009). An experimental study of the water transfer through confined compacted GMZ bentonite. *Engineering Geology, 108*(3), 169–176.

Ye, W.-M., Wan, M., Chen, B., Chen, Y., Cui, Y.-J., & Wang, J. (2009). Effect of temperature on soil-water characteristics and hysteresis of compacted Gaomiaozi bentonite. *Journal of Central South University of Technology, 16*, 821–826.

Zhao, X., Wang, J., Cai, M., Ma, L., Zong, Z., Wang, X., Su, R., Chen, W., Zhao, H., Chen, Q., An, Q., Qin, X., Ou, M., & Zhao, J. (2013). In-situ stress measurements and regional stress field assessment of the Beishan area, China. *Engineering Geology, 163*, 26–40.

Chapter 3
Experimental Basis

Chun-Liang Zhang, Ju Wang, Stephan Kaufhold, Yuemiao Liu, Oliver Czaikowski, Janis Pingel, Thorsten Schäfer, Yasmine Kouhail, Muriel Bouby, Frank Heberling, Nikoletta Morélova, Madeleine Stoll, Stephanie Kraft, Nadine Gill, Claudia Joseph, and Horst Geckeis

3.1 Geotechnical Investigation on GMZ

Chun-Liang Zhang, Ju Wang, Stephan Kaufhold, Yuemiao Liu, Oliver Czaikowski

A research programme has been conducted jointly by GRS together with BRIUG and BGR to characterize GMZ bentonite as buffer material in comparison with the well-known MX80 bentonite. With help of newly developed test methods, geotechnical properties and behaviour of the bentonites were determined, including chemical and mineralogical composition, water retention capacity, swelling capacity, water permeability, gas migration, self-sealing capacity, deformability, and thermal effects. A wide range of valuable results were obtained and are presented in detail in (Zhang et al., 2022). The essential results are extracted and represented here.

C.-L. Zhang · O. Czaikowski
Gesellschaft für Anlagen- und Reaktorsicherheit (GRS) gGmbH, 38122 Braunschweig, Germany

J. Wang · Y. Liu
Beishan Underground Research Laboratory for HLW Disposal, Beijing Research Institute of Uranium Geology, Beijing 100029, China

S. Kaufhold
Federal Institute for Geosciences and Natural Resources (BGR), 30655 Hannover, Germany

J. Pingel · T. Schäfer (✉)
Friedrich-Schiller-University Jena, Institute of Geosciences, Applied Geology, 07749 Jena, Germany
e-mail: thorsten.schaefer@uni-jena.de

Y. Kouhail · M. Bouby · F. Heberling · N. Morélova · M. Stoll · S. Kraft · N. Gill · C. Joseph · H. Geckeis
Karlsruhe Institute of Technology, Institute for Nuclear Waste Disposal (INE), 76094 Karlsruh, Germany

H. Shao et al. (eds.), *Thermo-Hydro-Mechanical-Chemical (THMC) Processes in Bentonite Barrier Systems*, Terrestrial Environmental Sciences,
https://doi.org/10.1007/978-3-031-53204-7_3

3.1.1 Sample Materials

Two types of the natural GMZ bentonite, GMZ01 and GZM02, were extracted from the deep and shallow positions of the bedded deposit in the northern China—Inner Mongolia autonomous region. As reference for comparison, the commercial MX80 bentonite from Wyoming in USA was taken, too.

The sample materials GMZ01 and GMZ02 were powder with fine grains $d < 74$ μm, whereas MX80 was granulated by crushing compacted blocks of a dry density of 2.0 g/cm^3 to grains $d = 0.2$–2 mm. Their initial water contents were measured after drying at 105 °C for 2 days to values of 10.3% at GMZ01, 8.0% at GMZ02 and 12.6% at MX80, respectively. The grain densities were determined on the dried samples using a helium gas pycnometer. Similar values were obtained to 2.67 g/cm^3 for MX80, and 2.66 g/cm^3 for GMZ01 and GMZ02.

The chemical components, exchangeable cations and cation exchange capacity of bentonite GMZ01 and GMZ02 were determined by BRIUG and summarized in Tables 3.1 and 3.2, respectively. The mineralogical compositions were determined by BGR by means of X-ray diffraction and Rietveld analysis. The mineralogical analysis was performed on the samples without preheating (A) and with preheating at 105 °C for 14 days (B) to examine the effect of the heat treatment. The measured results show that the bentonites consist predominantly of montmorillonite amounting to 86% in MX80, 71–74% in GMZ01 and 56% in GMZ02, respectively (Table 3.3). Accessory minerals are quartz, cristobalite, plagioclase, K-feldspar, etc. It is to be pointed out that the preheating did not affect the mineralogical compositions of the bentonites.

Table 3.1 Chemical components of bentonites GMZ01 and GMZ02

Sample	Al_2O_3	SiO_2	P_2O_3	CaO	K_2O	TiO_2	FeO
GMZ01	14.2	68.4	0.1	1.0	0.7	0.1	0.3
GMZ02	14.2	70.7		1.1	2.5	0.1	
Continuing	TFe_2O_3	MgO	Na_2O	MnO	SO_3	Ignition loss	
GMZ01	2.5	3.3	1.6	0.0		7.7	
GMZ02	1.2	2.4	1.5		0.0	5.4	

Table 3.2 Exchangeable cation and cation exchange capacity (CEC) of bentonites GMZ01 and GMZ02

Sample	Exchangeable cation		(mmol/100g)		CEC
	$E(K^+)$	$E(Na^+)$	$E(1/2Ca^{2+})$	$E(1/2Mg^{2+})$	(mmol/100g)
GMZ01	1	35	22	13	76
GMZ02	1	29	21	10	65

Table 3.3 Mineralogical components of bentonites GMZ01, GMZ02 and MX80

Bentonite	GMZ01		GMZ02		MX80	
Mineral content (%)	A	B	A	B	A	B
Montmorillonite	71	74	56	56	86	86
Quartz	14	12	17	17	6	6
Cristobalite	6	6	3	3	1	1
Plagioclase	6	6	6	7	2	3
K-Feldspar	3	2	8	7	3	1
Clinoptilolite			6	6		
Mica			4	4		
Gypsum					<1	2
Pyrite					<1	<1
Apatite					<1	<1

A: samples without preheat treatment
B: samples preheated at 105 °C for 14 days

For hydraulic testing, synthetic Beishan site groundwater (BSW) was manufactured. Its density and viscosity were measured at 20–50 °C as shown in Fig. 3.1. Both parameters decrease with increasing temperature. The viscosity of BSW is consistent with that of the distilled water (H_2O), which can be approached (UPC, 2015) by

$$\mu_w = A\, exp\left(\frac{B}{273.15 + T}\right) \tag{3.1}$$

where μ_w is the dynamic viscosity of the water (Pa·s), T is the temperature (°C), and the parameters $A = 2.05 \times 10^{-6}$ Pa·s and $B = 1805.5$ K.

3.1.2 Experimental Results

3.1.2.1 Water Retention

As a key property, water retention capacity of the bentonites was determined using vapour transfer technique. Loose and compacted specimens were placed in desiccators, in which the relative humidity was adjusted by different salt solutions. The loose specimens with an initial weight of 50 g each were placed in bowls, while the compacted ones were confined in stainless-steel cells of 50 mm diameter and 20 mm height. The compacted GMZ01 and GMZ02 specimens had dry densities of 1.7 and 1.8 g/cm^3, respectively, which are consistent with the designed buffer blocks (Liu et al., 2014). The compacted MX80 specimens had a dry density of 1.5 g/cm^3, which is nearly the same as that emplaced in a horizontal drift at Mont-Terri Rock Laboratory (Müller et al., 2018). These compacted specimens in the cells were

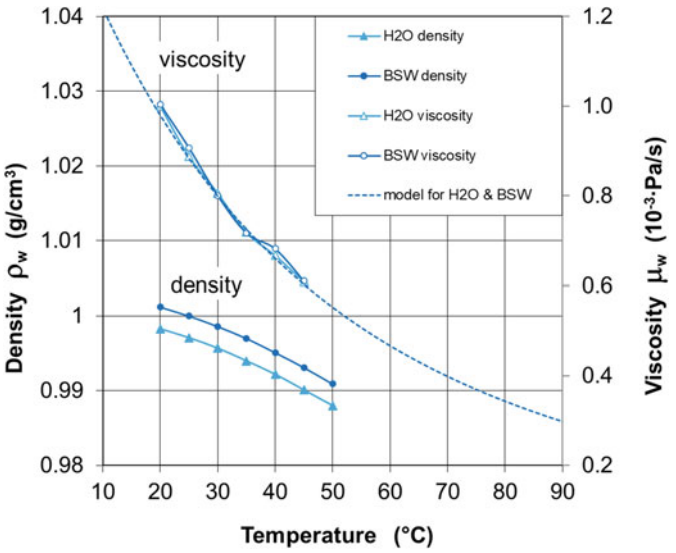

Fig. 3.1 Density and viscosity of the synthetic (BSW) and distilled water (H_2O)

covered with sintered porous discs allowing exchange of water vapour in- and outside. Under applied vapour-pressure or suction gradients between the specimens and the surrounding air, water molecules migrate from the humid air into the pore space in relatively dry specimens, or inversely. Whereas the relative humidity in each desiccator was continuously recorded by transistor psychrometer sensors, the amount of water uptake was measured by weighing the specimens at time intervals of 1–2 months until equilibrium. The relationship between relative humidity and suction is determined by the psychrometric law (Fredlund and Rahardjo, 1993).

$$s = -\frac{\rho_w R T}{M_w} \ln(RH) \tag{3.2}$$

where T is the absolute temperature, R is the universal gas constant, ρ_w and M_w are the density and the molecular mass of water, respectively. A range of RH–values of 22–100% was applied, corresponding to $s = 207$ to 0 MPa at the testing temperature of 24 °C.

The amounts of water uptake reached at equilibrium are depicted in Fig. 3.2 as a function of suction. As expected, water content of each bentonite increases with decreasing suction to a maximum at zero suction. The constant volumes of the compacted specimens limited the water uptake at low suctions $s < 5$–10 MPa. Therefore, each loose bentonite can take more water. The maximum water content reached at $s \approx 0$ increases with increasing montmorillonite content (f_m) due to its high capacity of water adsorption (Bradbury and Baeyens, 2002b; Yong et al., 2012; Birgersson et al., 2017; Villar et al., 2020).

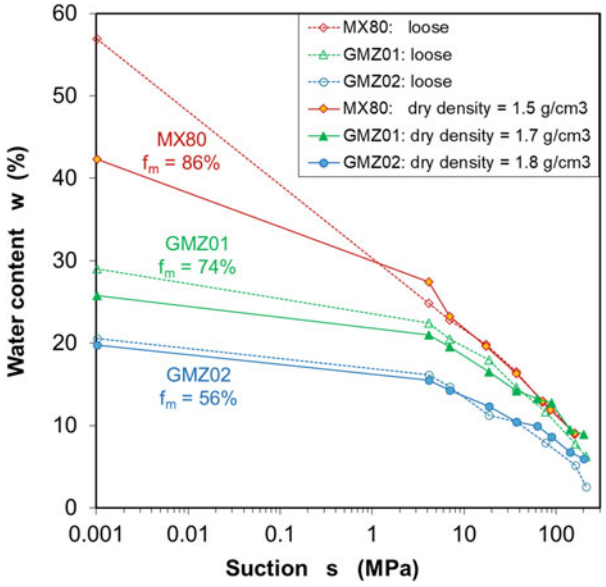

Fig. 3.2 Water retention curves of the bentonites in free and constraint conditions

There is a broad consensus that three types of water exist in bentonite: interlayer water, double-layer water and free water. The interlayer water is adsorbed on internal surfaces of montmorillonite units and immobile. The double-layer water exists in electrical double layers associated with external surfaces of the clay stacks, which is bounded and immobile too. The free water appears in interparticle pore space surrounding the clay stacks and other mineral particles. The distributions and proportions of the different types of water in a bentonite depend on the amount of permanent charge, exchangeable cations, soluble components, dry density (porosity) and water content (Kaufhold et al., 2010; Jenni et al., 2019). According to the calculations (Muurinen et al., 1987; Bradbury and Baeyens, 2002b), the free water content in the saturated bentonite MX80 is smaller than 5% at dry densities of 1.2–1.8 g/cm^3. In comparison, the bentonites GMZ01 and GMZ02 with such densities must comprise more free water due to their smaller montmorillonite contents.

3.1.2.2 Swelling Pressure

A test setup was developed and used for sequential measurements of swelling pressure, water permeability and gas migration of the bentonites. It consists of 14 stainless-steel cells, a syringe pump, hydraulic lines and instruments. Different kinds of specimens were prepared for testing as shown in Fig. 3.3. More than 40 specimens were compacted in the cells to a same size of 50 diameter and 15 mm height but to different dry densities of 1.3–1.8 g/cm^3. Moreover, the specimens of GMZ01

Fig. 3.3 Different kinds of specimens prepared using GMZ01 bentonite

pellets were produced by crushing compacted blocks (dry density = 1.7 g/cm^3) to grain sizes of 2–4 mm and loosely emplaced to a low dry density of 0.87 g/cm^3. The assembled blocks consisted of a central vertical gap of 3 mm width and had an average dry density of 1.65 g/cm^3. A mixture of pellets-blocks was prepared to a height of 15 mm for each layer and to an average dry density of 1.31 g/cm^3. All specimens were installed in the cells and heated at 105 °C for 2–3 days to match the initially heated and dried conditions in HLW buffer.

Figure 3.4 shows the development of swelling pressure with water uptake observed on some compacted specimens, loose pellets, assembled blocks and pellets-blocks mixture (cf. Fig. 3.3). The specimens took up water quickly for the first 3–5 days due to high suction effect and then slowly over time. Over 2–3 weeks, full saturation was reached at all the specimens. In correspondence to the water uptake, swelling pressure built up in the bentonites. They exhibited a typical swelling pressure evolution with a double-peak shape, independent of the initial inner structures. Generally, the double-peak evolution is attributed to variations of micro- and macrostructures in the compacted bentonite during saturation process (Pusch et al., 1990; Zhu et al., 2013; Imbert and Villar, 2006). The initial increase in swelling pressure is a direct consequence of water uptake and associated expansion of montmorillonite interlayers (interlayer swelling pressure). The interlayer expansion also destabilizes the macrostructure between clay particles. As the local swelling pressure reaches the first peak, the macrostructure in the wetted area becomes weaker, leading to a pressure relaxation. Simultaneously, the hydration in the electrical double layers between clay particles results in overlapping of thin water films at narrow spaces and generates repulsive forces (double-layer swelling pressure). This increases the global swelling pressure again to a constant value as the bentonite is fully saturated.

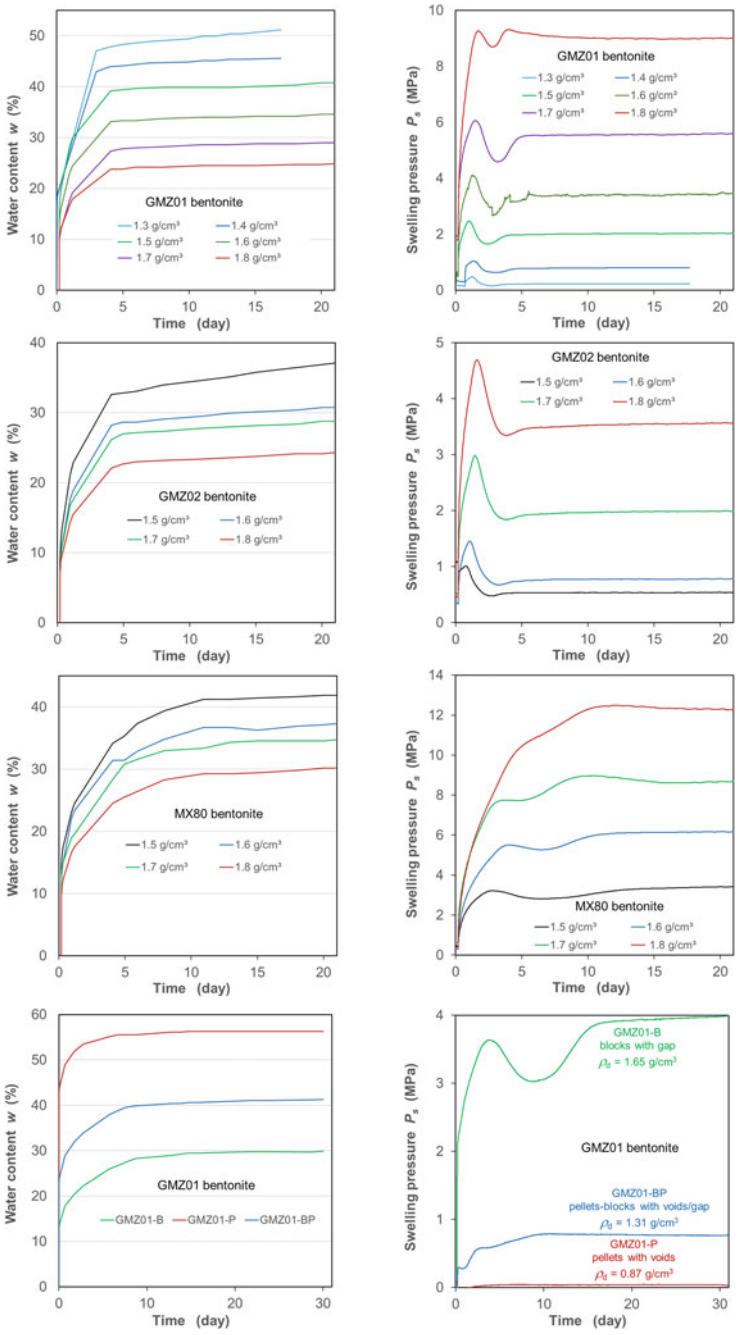

Fig. 3.4 Development of swelling pressure with hydration observed on the different bentonite specimens

The final swelling pressures P_s of all the specimens are summarized in Fig. 3.5 as a function of dry density ρ_d together with some data from literature. The data indicate strong dependencies of the swelling pressure on the dry density ρ_d and the montmorillonite content f_m, which can be approached by an empirical model

$$P_s = \alpha \ f_m^n \ exp\,(\beta \ \rho_d) \tag{3.3}$$

where α, β and n are the parameters. Fitting the present data yields the parameter values of $\alpha = 0.0006$ MPa, $\beta = 6$ cm^3/g and $n = 3.7$. The model curves represent the mean lines through the scattered data for each kind of bentonite. This model can also match the P_s-ρ_d curve of FEBEX bentonite with a montmorillonite content $f_m = 90\%$ (Villar et al., 2010). It can also be seen that the data resulted from the synthetic groundwater (BSW) are consistent with those from the deionized water (H_2O) for GMZ01 (Zhang et al., 2019; Xu et al., 2017) and for MX80 (Bucher and Müller-Vonmoos, 1989; Karnland et al., 2008; Seiphoori, 2015).

It is interesting to point out that the swelling pressure data obtained from GMZ01 pellets and blocks with the large voids/gaps are consistent with those of the compacted homogeneous specimens. This is the consequence of homogenization of the inner structure in the pellets due to the swelling of clay particles with hydration. Figure 3.6 pictures the homogenized pellets and the sealed gap between blocks, compared with the initial states (Fig. 3.3b, c). Because of the low density of the pellets, the large voids between the particles could not be completely sealed. In contrast, the gap between the blocks could be completely sealed by the high swelling of the dense bentonite matrix.

3.1.2.3 Water Permeability

After the specimens were fully saturated, the water injection pressure was stepwise increased from 0.1 to 1.5 MPa, while water outflow was measured using the scaled burette at atmospheric pressure. Each pressure step lasted over days to a month for reaching steady flow. The hydraulic gradient across a specimen is calculated by

$$i = \frac{P_w - P_o}{\rho_w g \ L} \tag{3.4}$$

where P_w and P_o are the up- and downstream pressures (kPa), ρ_w is the water density (kg/m^3), g is the gravitational acceleration (9.81 m/s^2) and L is the specimen length (m). The calculated i-values vary in a range of 60–1000. The application of the different hydraulic gradients aimed at validating Darcy's law for the compacted bentonites. During steady flow, hydraulic conductivity K_h (m/s) and/or intrinsic permeability K_w (m^2) can be determined according to Darcy's law (Liu, 2017)

$$K_h = \frac{v}{i} = \frac{Q_w \ \rho_w \ g \ L}{A \ (P_w - P_o)} \tag{3.5}$$

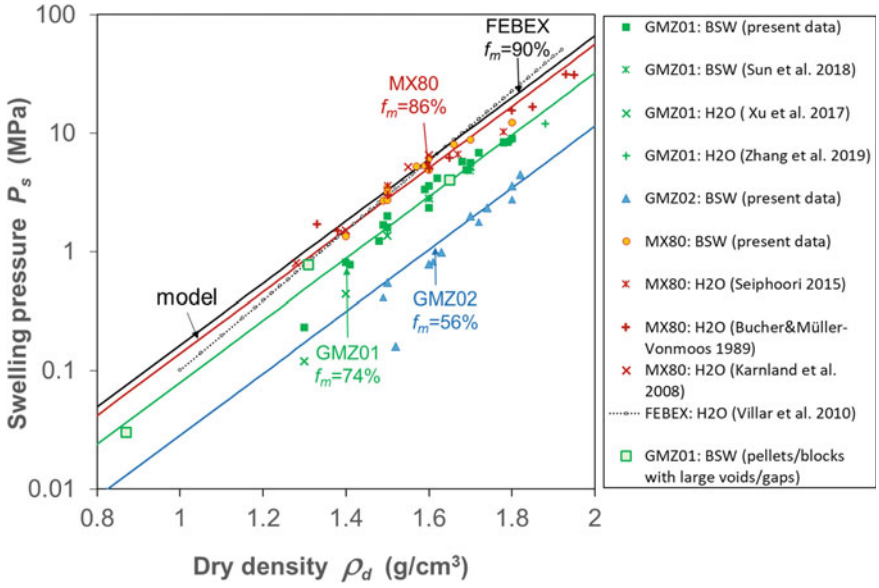

Fig. 3.5 Summary of swelling pressure data for the various bentonites

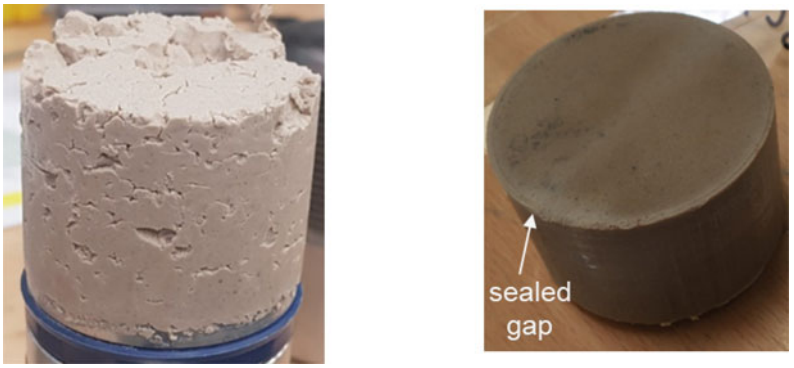

Fig. 3.6 Pictures of **a** homogenized pellets and **b** self-sealed gap between blocks of GMZ01 bentonite after water flow through a month

$$K_w = \frac{Q_w \ \mu_w \ L}{A \ (P_w - P_o)} = K_h \frac{\mu_w}{\rho_w \ g} \tag{3.6}$$

where v is the average velocity (m/s) of water flux Q_w (m^3/s) through the section A (m^2), μ_w is the water viscosity (Pa·s), P_w and P_o are the up- and downstream pressures (Pa).

Figure 3.7 depicts water flow velocities v measured across the specimens at different hydraulic gradients. At GMZ01 and GMZ02 specimens with dry densities of

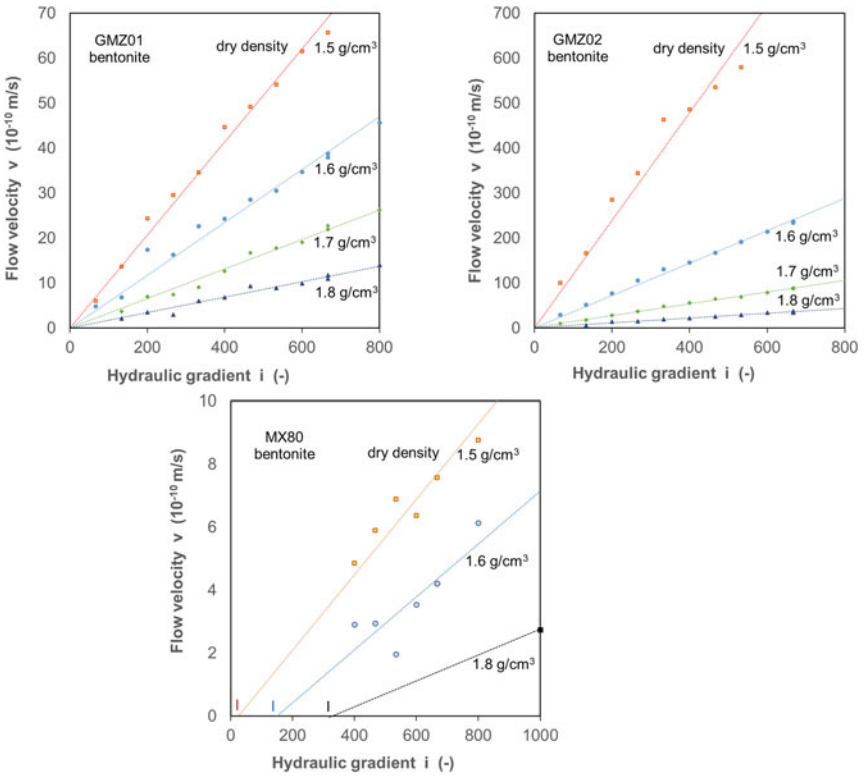

Fig. 3.7 Water flow velocities measured at different hydraulic gradients

1.5–1.8 g/cm^3, the flow velocity is linearly related with the hydraulic gradient and the *v-i* lines pass through the origin of the coordinate system. This confirms Darcy's law for the compacted bentonites GMZ01 and GMZ02. In contrast, the *v-i* lines for the compacted MX80 specimens are even though linear but do not pass through the origin of the coordinate system. The intersection of the line with *i*-axis is the threshold gradient *I*, which are estimated to be ~20 at $\rho d = 1.5$ g/cm^3, ~150 at $\rho d = 1.6$ g/cm^3 and ~300 at $\rho_d = 1.8$ g/cm^3, respectively. The existence of threshold gradients should be attributed to the immobile state of the strongly bound water in the dense bentonite. At low hydraulic gradients $i < I$, the bound water cannot be moved.

The slope of the *v-i* line is equal to the hydraulic conductivity K_h (Eq. 3.5) and the corresponding water permeability K_w can be derived (Eq. 3.6). The measuredK_w-data are summarized in Fig. 3.8 as a function of total porosity φ. As expected, the permeability decreases with decreasing porosity and with increasing montmorillonite content, which can be approximately approached by

$$K_w = \kappa \ (1 - f_m)^m \ exp(\omega \phi) \tag{3.7}$$

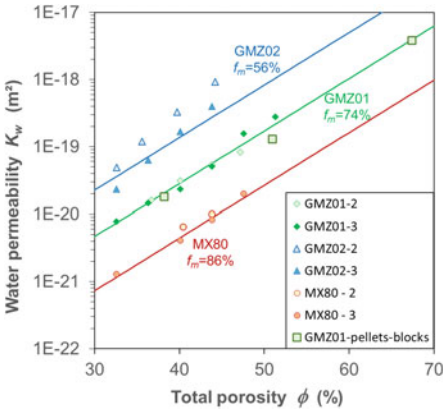

Fig. 3.8 Summary of water permeability data for the bentonites as a function of total porosity and montmorillonite content

where α, β and η are the parameters. Fitting the data yields $\alpha = 8 \times 10^{-22}$ m^2, $m = 3.2$ and $\omega = 20$. The calculated curves agree well with the data.

In fact, the water permeability is determined by effective porosity rather than total porosity. The effective porosity mostly consists of macropores containing free water. The size and connectivity of the macropores are dominated by the swelling pressure of the neighbouring clay particles. Therefore, the water permeability shall be related to the swelling pressure, as shown in Fig. 3.9. It is evidence that the water permeability of the bentonites decreases linearly with increasing swelling pressure. Additionally, the water permeability also decreases with increasing montmorillonite content, which determines the proportions of free and bound pore water. The relationships can be expressed by

$$K_w = \gamma \ (1 - f_m)^{\eta} \ P_s \tag{3.8}$$

where γ and η are the parameters. $\gamma = 1.2 \times 10^{-18}$ m^2 and $\eta = 2$ are determined based on the data. A comparison indicates a reasonable agreement between the model and the data.

As mentioned earlier, the loose pellets and assembled blocks of GMZ01 bentonite became homogenized under swelling effect. Even though some big voids remained in the saturated pellets (Fig. 3.6a), the water permeability of the whole specimen is still very low. This is because the permeability is mainly governed by the narrowed throats of the pathway network.

3.1.2.4 Gas Penetration

Gas penetration testing followed with some water-saturated specimens. Before testing, the water remaining in the inlet and outlet reservoirs was removed by vacuum pumping. Helium gas was then injected to the specimens at controlled flow rates of 0.02–0.2 ml/min, while gas outflow was accumulated in a steel vessel with a volume of 380 ml. Gas pressures in the up- and downstream were monitored by pressure

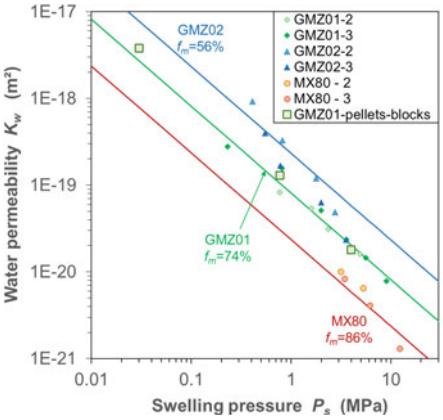

Fig. 3.9 Water permeability of the bentonites in relation with swelling pressure and montmorillonite content

transducers. Stress reaction was recorded by the load cell at the opposite side. The gas injection lasted for sufficient time periods to examine long-term gas flow process and to determine gas breakthrough pressure and permeability. The gas outflow rate can be estimated from the pressure difference across the specimen with elapsed time (Gutiérrez-Rodrigo et al., 2021)

$$Q_g = V_g \frac{P_g\left(t_j\right) - P_g\left(t_i\right)}{P_m} \frac{1}{\Delta t} \tag{3.9}$$

where Q_g is the mean gas flux (m^3/s), V_g is the volume of the outlet reservoir (m^3), $P_g(t_j)$ and $P_g(t_i)$ are the in- or outlet gas pressures (Pa) at time points j and i, P_m is the average gas pressure between the measurement interval $\Delta t = t_j$—t_i (s). Effective gas permeability K_g (m^2) is then estimated by Darcy's law:

$$K_g = \frac{2\ Q_g\ \mu_g\ P_o\ L}{A\ \left(P_g^2 - P_o^2\right)} \tag{3.10}$$

where μ_g is the dynamic viscosity of helium gas (1.96×10^{-5} Pa·s).

Test data are illustrated in Fig. 3.10 for the homogeneous specimens and in Fig. 3.11 for the homogenized pellets and sealed blocks (cf. Fig. 3.6) in terms of applied gas flow rate (Q_g), induced up- and downstream pressures (P_g, P_o), axial total stress (σ_a) and outflow rate (Q_o) versus elapsed time. It is evident that the gas penetration process was qualitatively quite similar with multiple gas breakthrough events and unstable post-breakthrough flow, but quantitatively different in each specimen due to the different material properties and gas injection rates.

The gas injection led to a gradual build-up of the upstream pressure, accompanied by an increase of the total stress over the initial swelling pressure. This implies that the water-saturated bentonites were gas tight and subjected to compression by the gas pressure against the rigid boundary. As a peak pressure P_{gb} was reached, gas

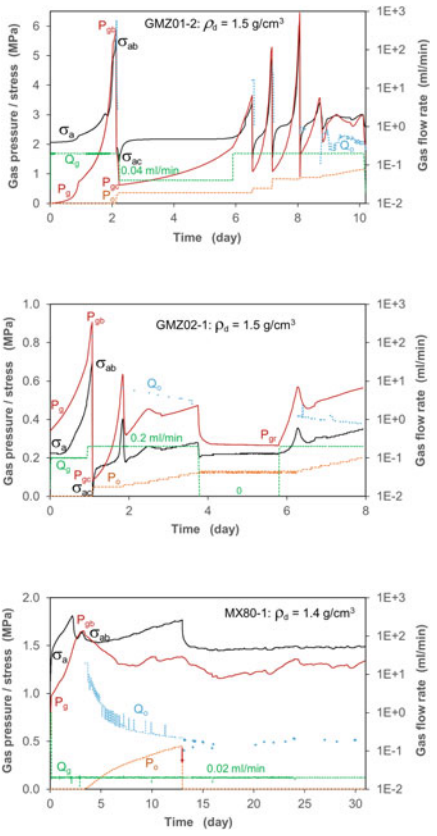

Fig. 3.10 Gas penetration in the water-saturated and homogeneous bentonite specimens

breakthrough occurred, yielding a rapid gas release and hence a rapid drop of the upstream pressure as well as a rapid rise of the downstream backpressure. When the upstream pressure dropped down to a minimum value P_{gc} and the backpressure P_o became constant, the gas flow ceased due to self-sealing of the pathways. The upper peak P_{gb} is usually defined as the gas breakthrough pressure, whereas the lower peak P_{gc} is referred to as the gas seal pressure. In correspondence to the drop of the gas pressure from P_{gb} to P_{gc}, the total stress decreased from σ_{ab} to σ_{ac}. Following the first gas breakthrough/ sealing event, further gas injection caused multiple rising/dropping of the upstream pressure, reflecting opening/closing cycles of the pathway network. The temporal disconnections of the network tended to disappear with time and then a continual gas flow followed. In the closed downstream, the backpressure increased with gas accumulation, leading to an increase in average pore pressure ($P_{gp} = (P_g + P_o)/2$) and a decrease in pressure gradient ($\Delta P_g = P_g - P_o$). The unsteady pressure conditions caused variations in features of the pathway network (aperture, connectivity, etc.) and thus the gas flowed unsteadily.

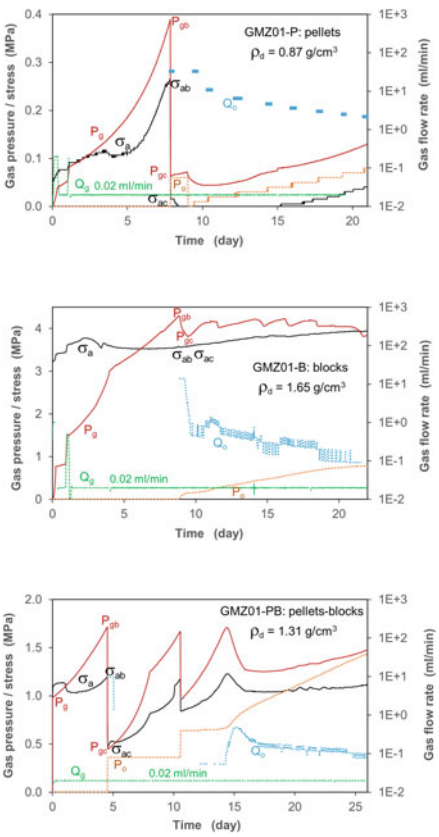

Fig. 3.11 Gas penetration in the water-saturated, homogenized pellets and sealed blocks

Extensive investigations (e.g. Pusch et al. (1987); Sellin (2014); Harrington et al. (2017); Levasseur et al. (2020)) suggested that gas entry and penetration in water-saturated bentonite is governed by dilating local pores in weak regions to form micro-fissures, which needs a high gas pressure exceeding the sum of the minor principal stress and tensile strength of the material. This can be expressed as

$$P_{gb} \geq \sigma_{\min} + \sigma_T \tag{3.11}$$

where σ_{min} is the minor principal stress and σ_T is the tensile strength of the material. In case of the oedometer conditions, the radial stress should be the minor one $\sigma_r = \sigma_{min}$, which can be assumed being nearly equal to the axial one, $\sigma_r = \sigma_{min} \approx \sigma_a$. Thus above Eq. (3.11) can be rewritten by

$$P_{gb} \geq \sigma_{rb} + \sigma_T \approx \sigma_{ab} + \sigma_T \tag{3.12}$$

The tensile strength can be estimated by $\sigma_T = P_{gb} - \sigma_{ab}$, which depends on the confining stress. A linear relationship is here assumed, $\sigma_T = b \times \sigma_{ab}$. Thus, equation (3.12) can be expressed by

$$P_{gb} \geq (1 + b)\, \sigma_{ab} \tag{3.13}$$

and the gas breakthrough boundary condition is defined by

$$P_{gb} = \sigma_{ab} + \sigma_T = (1 + b)\, \sigma_{ab} \tag{3.14}$$

The first gas breakthrough pressures observed on each specimen are depicted in Fig. 3.12a as a function of the total stress. Fitting the data from GMZ01, GMZ02 and MX80 specimens yields the parameter $b = 0.09$. It is obvious that this model matches the data well. Additionally, the model can also predict the gas breakthrough pressures observed in other lab tests (Graham et al., 2016; Harrington et al., 2017) and in a full-scale buffer test Lasgit (Cuss et al., 2014), as shown in Fig. 3.12b. It is to be noted that this gas breakthrough criterion is adequate for water-saturated bentonite under volume-constrained conditions. If the boundary is not rigid, the bentonite specimen is allowed to deform by gas pressuring, which can result in micro-fissuring at pressures below the confining stresses. This has been evidenced in tests on MX80 bentonite in oedometer cell under controlled axial load (Zhang, 2021) and on GMZ01 bentonite in triaxial cell under isostatic load (Cui et al., 2021).

Effective gas permeability K_g was determined from the data of gas outflow Q_o for each specimen. Figure 3.13 shows some typical results of evolution of gas permeability in correlation with effective stress ($\sigma_{eff} = \sigma - P_{gp}$). It is obvious that the gas permeability in $\log(K_g)$ varies inversely with the periodic variation of the effective stress. In fact, the effective stress controls the geometric features of the network and thus the permeability. Final K_g-values at the end of each test are depicted in Fig. 3.14 as a function of effective stress, which can be approximately approached by

$$K_g = K_{go}\, exp\left(-\xi\, \sigma_{eff}\right) \tag{3.15}$$

where K_{go} is the gas permeability at $\sigma_{eff} = 0$ and ξ is a parameter. Fitting the data yields $K_{go} = 7 \times 10^{-17}$ m^2 and $\xi = 4$, with which the model curve matches the data well.

After testing, the residual water content was determined on each specimen. Most of the tested specimens showed the full saturation after gas flowing through, except for the pellets and pellets-blocks mixture. The full saturation implies that no or negligible amount of pore water were displaced out by gas injection and the gas penetration was caused by generating and dilating micro-fissures. In contrast, the desaturation of the pellets indicates that the water in some large voids (Fig. 3.6a) was partially removed by the injected gas.

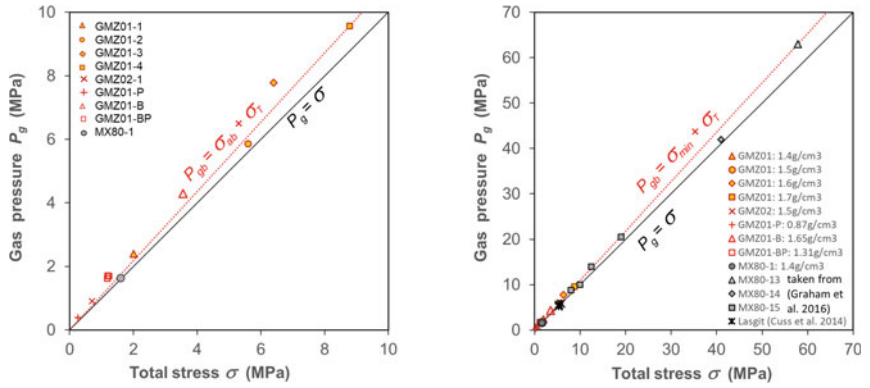

(**a**) present data (**b**) compared with literature data

Fig. 3.12 Relationship of gas breakthrough pressure with total stress: **a** obtained from the saturated specimens of GMZ01, GMZ02 and MX80 bentonites and **b** compared with literature data from small-scale specimens (Graham et al., 2016) and full-scale buffer of MX80 bentonite (Cuss et al., 2014)

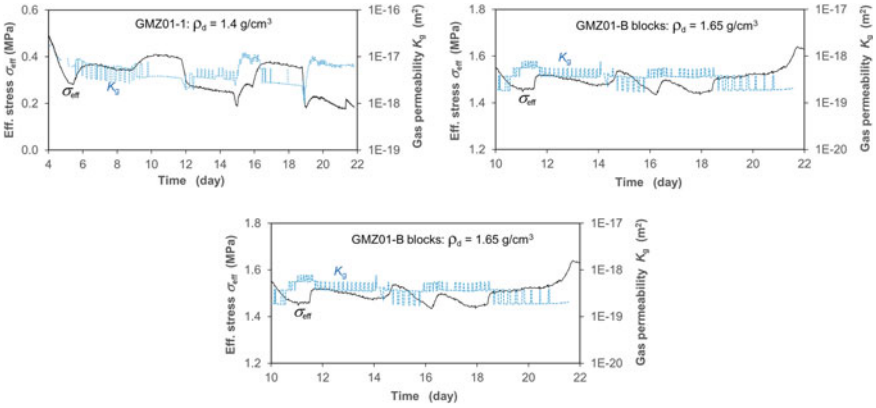

Fig. 3.13 Evolution of gas permeability in correlation with effective stress

3.1.2.5 Thermal Effects

Two coupled load rigs were used for thermal testing. Each rig allows two specimens in stainless-steel cells of 120 mm diameter and 160 mm height one upon another. They are installed in separated thermal chambers and can be heated up to 110 °C. Each specimen is covered with sintered porous plates and connected to thin holes through the upper load piston and the lower basic plate for fluid flow. A syringe pump is used for fluid injection at the bottom, while fluid outflow is measured at the top by means of scaled burette at atmospheric pressure. Gas testing is carried out by injecting helium gas at controlled flow rates, during which gas outflow is accumulated

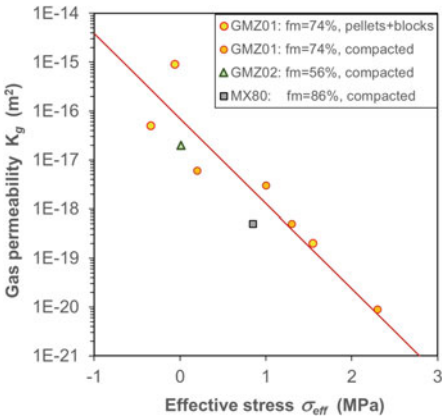

Fig. 3.14 Gas permeability of the compacted bentonites as a function of effective stress

Table 3.4 Initial characteristics of the bentonite specimens for thermal testing

Specimens	GMZ01a-b	GMZ02a-b
Height/Diameter (mm)	25/120	23/120
Bulk density (g/cm^3)	1.86	2.0
Dry density (g/cm^3)	1.71	1.85
Porosity (%)	35.7	30.6
Water content (%)	8.1	7.0
Saturation degree (%)	39	42

in a steel vessel and the outlet pressure is recorded. Axial load is applied by means of another syringe pump. Axial deformation is monitored using two linear variable differential transducers (LVDTs) mounted between the upper piston and the cell top.

Two specimens of each bentonite GMZ01 and GMZ02 were pre-compacted in the cells to respective dry densities of 1.71 and 1.85 g/cm^3. Their initial characteristics are summarized in Table 3.4.

A test procedure was carried out with sequence steps:

I. Application of axial stress $\sigma_a = 4$ MPa, under which the temperature was increased to 90 °C at GMZ01a/02a and 30 °C at GMZ01b/02b, respectively.
II. Hydration followed by infiltration of the synthetic water BSW into the specimens at atmospheric pressure, whereby their water uptake and axial strain were monitored.
III. Unloading to $\sigma_a = 2$ MPa and then reloading to $\sigma_a = 4$ MPa again, under which axial strain and water permeability of the saturated specimens were recorded.
IV. Gas injection at controlled flow rates to determine gas breakthrough pressure and permeability of the specimens at different temperatures.

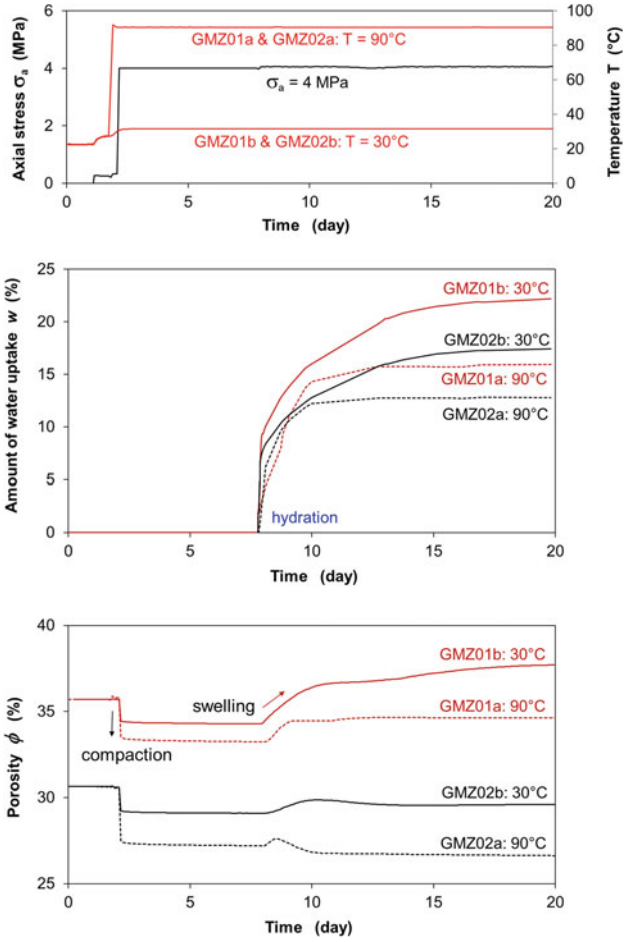

Fig. 3.15 Thermo-mechanical compaction and swelling with hydration observed on bentonite specimens at temperatures of 30 and 90 °C and axial load of 4 MPa

V. Examination of self-sealing of gas pathways by measuring water permeability of a specimen at $\sigma_a = 4$ MPa and T = 100–30 °C.

Figure 3.15 illustrates the water uptake and the porosity variation of the specimens during hydration. Initially, the specimens were thermo-mechanically loaded to T = 90 °C at GMZ01a/02a and 30 °C at GMZ01b/02b and to $\sigma_a = 4$ MPa over 7 days. The load resulted in a rapid compaction in the beginning and then followed by a slight reduction in porosity with time at each specimen. The compaction at the high temperature is relatively larger due to more thermal mobilization of the pore water, which reduces the cohesion between clay particles and thus easier collapse of the pore structure.

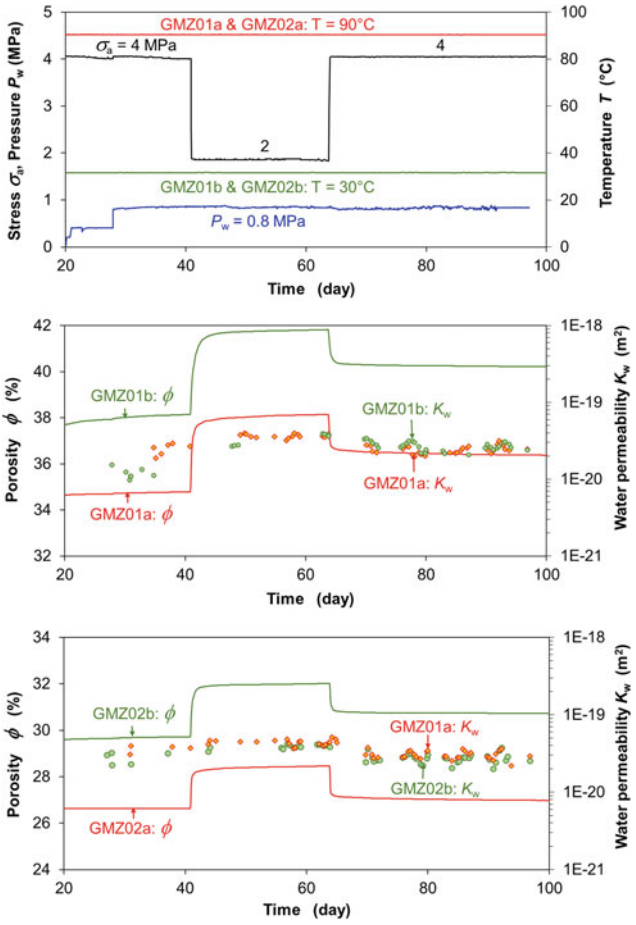

Fig. 3.16 Deformation and water permeability changes of saturated bentonite specimens at temperatures of 30 and 90 °C and axial loads of 2–4 MPa

As water was introduced into the specimens, a hydration process began quickly with rapid water uptake and then slowed down with time until fully saturated. The full saturation was reached relatively earlier at 90 °C but the amount of water uptake was relatively lower than at 30 °C. This indicates that the water absorption capacity of the bentonites decreases with increasing temperature. Furthermore, the water uptake caused a gradual swelling of GMZ01 bentonite to a porosity increase of 1.5% at 90 °C and 3.5% at 30 °C over 12 days, respectively. Obviously, the swelling capacity decreases with increasing temperature. Compared to GMZ01, GMZ02 showed the lower capacities of water absorption and swelling because of its lower montmorillonite content.

Thermal effects on deformation and water permeability of the saturated bentonites are shown in Fig. 3.16. Keeping the applied temperatures and axial stress,

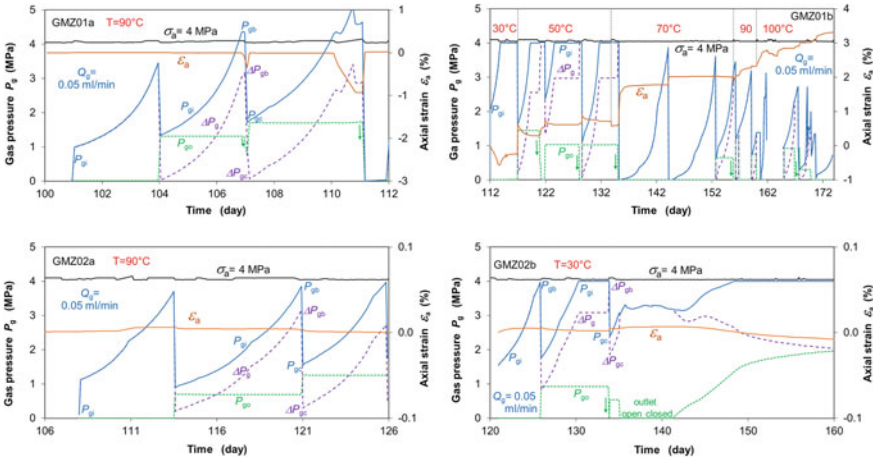

Fig. 3.17 Gas pressures and associated axial strains observed on the water-saturated bentonite specimens at axial load of 4 MPa and different temperatures of 30–100 °C

the water injection pressure was increased to $P_w = 0.4$ and 0.8 MPa. This caused a slight increase in porosity at GMZ01a/b but not at GMZ02a/b. When the stress was lowered to 2 MPa, all specimens expanded in the beginning and then tended to constant. Subsequent reloading caused reconsolidation. The deformation of each bentonite appeared quite similar at the different temperatures, indicating a negligible temperature influence on deformation. Moreover, the tests also showed insignificant temperature influence on water permeability of the bentonites. However, the permeabilities obtained from GMZ01a/b are about one order of magnitude lower than that of GMZ02a/b. This is attributed to the different montmorillonite contents. The higher montmorillonite content in GMZ01 means the higher fraction of absorbed immobile pore water and thus the lower effective porosity.

Results of the gas penetration tests are illustrated in Fig. 3.17. Under the constant load and temperature, gas injection led to a gradual build-up of the upstream pressure P_{gi} until breakthrough occurred at a peak P_{gb}. The breakthrough yielded a rapid gas release and hence a rapid drop of the upstream pressure to a minimum P_{gc} as well as a rapid rise of the backpressure P_{go}. When P_{go} maintained constant, no gas flowed through the specimen due to sealing of the gas pathways. The gas breakthrough/sealing event repeated itself with continued gas injection, reflecting a periodic process of the path opening/closing under interactions between gas pressure and confining stress.

The tests showed influences of different factors on the gas breakthrough and seal pressures P_{gb} and P_{gc}. For instance, GMZ01a/02a at 90 °C showed that both the pressures P_{gb} and P_{gc} *increase* with increasing backpressure P_{go}. The breakthrough pressure can exceed the confining stress at elevated backpressures (e.g. GMZ01a at 90 °C). When the injection pressure was limited to $P_g = 3.9$ MPa slightly below the confining stress at GMZ01b/02b, no gas breakthrough was observed when $P_{go} > 0$.

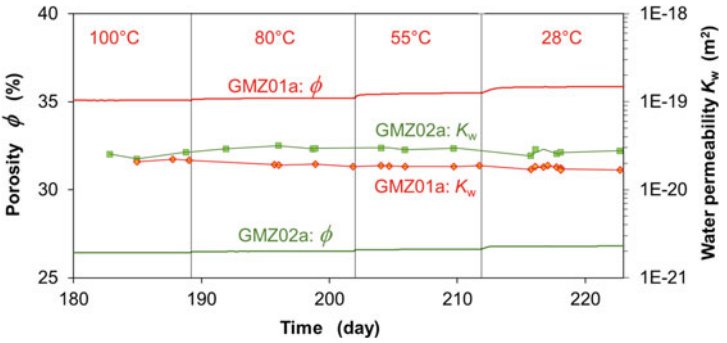

Fig. 3.18 Water permeabilities measured on bentonite specimens after gas penetration

This means that the gas backpressure shall be taken in Eq. (3.11) by

$$P_{gb} \geq \sigma_{\min} + P_{go} + \sigma_T \tag{3.16}$$

$$P_{gb} - P_{go} \geq \sigma_{\min} + \sigma_T \tag{3.17}$$

where $P_{gb} - P_{go} = \Delta P_{gb}$ can be taken as the effective gas breakthrough pressure.

Thermal effect on gas penetration in the water-saturated bentonites was examined on specimen GMZ01b by increasing temperature from 30 to 50, 70, 90 and 100 °C. It was observed that the gas breakthrough pressure decreased with increasing temperature. This is attributed to the thermally reduced viscosity and absorption forces in the pore water.

The tests also showed some influences of gas pressure on deformation of the bentonites, particularly at gas breakthrough event. The increase in gas injection pressure can dilate the pore space and then create micro-fissures for gas flowing. After breakthrough, the release of the gas pressure increases the effective stress, leading to the closing and sealing of the pathways.

Figure 3.18 shows the self-sealing effect of the gas pathways by measuring water permeabilities of two specimens GMZ01a/02a after gas penetration. The data obtained at decreased temperatures of 100, 80, 55 and 28 °C indicate no significant influence of temperature on water permeability. Average values are determined to $K_w = 2 \times 10^{-20}$ for GMZ01a and 3×10^{-20} m^2 for GMZ02a, which are closely consistent with those obtained before the gas generation (cf. Fig. 3.16).

3.1.3 Conclusions

As the buffer material for the potential repository in China, two types of GMZ bentonite were investigated in comparison with the well-known MX80 bentonite. It was found out that the geotechnical properties and behaviour of the bentonites are

dominated by the montmorillonite content and the dry density. Major findings are listed as

(1) The water absorption capacity increases with increasing montmorillonite content. The maximum water content is reached at zero suction but can be limited at low porosities.
(2) The swelling pressure builds up with hydration, which is characterized by a typical double-peak pattern due to variations of the inner structure. The maximum swelling pressure at full saturation increases exponentially with increasing montmorillonite content and dry density.
(3) Threshold hydraulic gradients were observed on compacted MX80 bentonite at dry densities above 1.5 g/cm^3, but not on GMZ01 and GMZ02. The water permeability decreases exponentially with increasing montmorillonite content and linearly with swelling pressure.
(4) Gas penetration into the water-saturated bentonites under rigid boundary conditions requires high overpressures that exceed the total stress and tensile strength of the material to create local microcracks for gas passage. After gas breakthrough, the pathway network tends to self-seal under swelling effect of the surrounding bentonite.
(5) Large voids/gaps remaining in the bentonite pellets and assembled blocks tend to disappear with homogenization process during hydration and swelling.
(6) Various thermal effects were observed: (a) increasing temperature reduces the water absorption capacity and thus the swelling capacity; (b) the hydraulic conductivity is influenced by temperature due to thermally induced variations in viscosity and density of the flowing water, whereas the intrinsic water permeability is almost independent of temperature but dependent on thermally induced variation in effective porosity; (c) increasing temperature increases the mobility of adsorbed pore water and thus lowers the pressure threshold for gas penetration and (d) no negative thermal impact on the bentonite buffer performance was found.

3.2 Mineralogical Investigation on GMZ01/GMZ02

S. Kaufhold

3.2.1 Sample Material and Methods

Samples GMZ 01 and GMZ 02 were received from GRS in 2019 and characterized using a set of methods which are introduced in the following.

The mineralogical composition was determined based on X-ray diffraction (XRD), infrared spectroscopy (IR) and simultaneous thermal analysis (STA). The chemical

composition was determined both by X-ray fluorescence (XRF) and C-/S-analysis (LECO).

XRD patterns were recorded using a PANalytical X'Pert PRO MPD Θ–Θ diffractometer (Co-Kα radiation generated at 40 kV and 40 mA), equipped with a variable divergence slit (20 mm irradiated length), primary and secondary soller, diffracted beam monochromator, point detector and a sample changer (sample diameter 28 mm). The samples were investigated from 1° to 75° 2Θ with a step size of 0.03° 2Θ and a measuring time of 12 sec per step. For specimen preparation the back loading technique was used.

From XRD patterns the mineralogical composition was calculated by using the Rietveld software AutoQuan® (AQ; Bergmann and Kleeberg (1998)). After a detailed qualitative analysis, appropriate structural models were selected and applied to all samples. The montmorillonite (smectite) content was calculated by using the structural model published by Ufer et al. (2004). Refined values were obtained based on the AutoQuan® results by considering the chemical composition and the variability of clay minerals. Additionally, the montmorillonite content was calculated by considering the CEC assuming 15% variable charge as well as a layer charge density of −0.30 eq/formula unit according to Kaufhold et al. (2002). The CEC was measured using the Cu-Triethylenetetramine method (Kahr et al., 1996; Lorenz et al., 1999).

For measuring mid (MIR)-infrared spectra the KBr pellet technique was applied. Spectra were collected on a Thermo Nicolet Nicolet iS50 FTIR spectrometer (MIR beam splitter: KBr, detector DTGS TEC). The resolution was adjusted to 2 cm^{-1}. Details about the analytical procedure allowing to quantify the mineralogical composition were published by Kaufhold et al. (2012). The spectrometer was built by Nicolet Instruments, Madison, Verona Road, Wisconsin, USA.

Thermoanalytical investigations were performed using a Netzsch 449 F3 Jupiter thermobalance equipped with a DSC/TG sample holder linked to a Netzsch QMS 403 C Aeolus mass spectrometer (MS). 100 mg of powdered material previously equilibrated at 53% relative humidity (RH) was heated from 25 to 1150 °C with a heating rate of 10 K/min. The devices were manufactured by Netzsch (Selb, Germany).

The organic carbon (Corg) content was measured with a LECO CS-444-Analysator after dissolution of the carbonates. Carbonates had been removed by treating the samples several times at 80 °C with HCl until no further gas evolution could be observed. Samples of 170–180 mg of the dried material were used to measure the total carbon (Ctotal) content. Total inorganic carbon (Ccarb) was calculated by the difference of Ctotal and Corg. The samples were heated in the device to 1800–2000 °C in an oxygen atmosphere and the amount of CO2 and SO2 was detected by an infrared detector. The device was built by LECO (St. Joseph, Michigan U.S.A.).

3.2.2 Results

Results of XRD analysis are shown in Fig. 3.19 and the mineralogical composition as determined by Rietveld is given in Table 3.5.

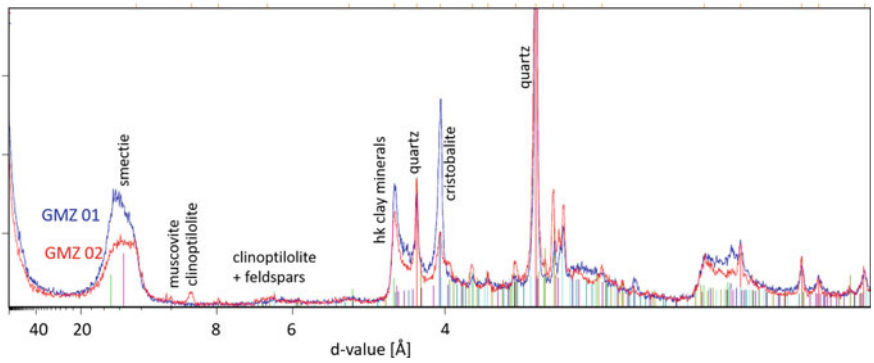

Fig. 3.19 XRD pattern and qualitative analysis of the two samples

Table 3.5 Cation exchange capacity (CEC) and mineralogical composition of the two samples according to Rietveld refinement, IR spectroscopy, and after correction of the XRD and IR results using XRF

		GMZ01	GMZ02	GMZ01	GMZ02	GMZ01	GMZ02
		Rietveld refinement		IR (Kaufhold et al., 2012)		XRF corrected	
Smectite	[mass%]	73	56	59	46	70	52
Quartz	[mass%]	13	17	11	15	12	16
Muscovite	[mass%]		4		4		3
Plagioclase	[mass%]	6	7	8	8	6	7
K-feldspar	[mass%]	2	7	3	10	3	7
Cristobalite	[mass%]	6	3	19	14	9	9
Clinoptilolite	[mass%]		6		3		6
Kaolinite	[mass%]			0.5		0.5	
CEC	[meg/100g]	75	50	75	50	75	50

According to XRD-Rietveld refinement and CEC results, sample GMZ 01 contains more smectite than GMZ 02. Assuming a mass of a formula unit accounting for 365 g/mol (which is a reasonable assumption because of low Fe content), 15% variable charge, a layer charge density (LCD) accounting for 0.33 eq/FU, it is possible to explain 70 mass% smectite and a CEC of 75 meq/100g (sample GMZ 01). The combination of 52 mass% smectite and a CEC of 50 meq/100g could be explained by a somewhat lower layer charge density (0.30 eq/FU) of sample GMZ 02. This comparison, however, is not suitable to determine the layer charge density which, therefore, has to be investigated in future.

Sample GMZ 02 contains less smectite than GMZ 01 but more feldspar and quartz. This sample also contains muscovite and clinoptilolite which were not found in sample GMZ 01. The chemical composition is given in Table 3.6.

Table 3.6 Chemical composition of both samples based on XRF and LECO analysis

		GMZ01	GMZ02			GMZ01	GMZ02			GMZ01	GMZ02
LECO											
C_{org}	[mass%]	0.02	0.02	As	[mg/kg]	3	<3	Rb	[mg/kg]	40	100
C_{carb}	[mass%]	0.01	0.01	Ba	[mg/kg]	252	271	Sb	[mg/kg]	<20	<19
S_{total}	[mass%]	0.03	0.03	Bi	[mg/kg]	<6	<5	Sc	[mg/kg]	<26	<24
XRF				Ce	[mg/kg]	<52	<52	SM	[mg/kg]	<23	<23
SiO_2	[mass%]	64.4	66.9	Co	[mg/kg]	<8	<7	Sn	[mg/kg]	<17	<16
TiO_2	[mass%]	0.1	0.2	Cr	[mg/kg]	<11	<20	Sr	[mg/kg]	350	453
AI_2O_3	[mass%]	13.4	13.2	Cs	[mg/kg]	<54	<51	Ta	[mg/kg]	<11	<11
Fe_2O_3	[mass%]	2.6	1.9	Cu	[mg/kg]	<6	<6	Th	[mg/kg]	20	20
MnO	[mass%]	0.0	0.01	Ga	[mg/kg]	30	26	U	[mg/kg]	9	<8
MgO	[mass%]	3.1	2.3	Hf	[mg/kg]	<17	<17	V	[mg/kg]	<16	28
CaO	[mass%]	0.9	1.1	La	[mg/kg]	<47	<47	W	[mg/kg]	<11	<10
Na_2O	[mass%]	1.5	1.6	Mo	[mg/kg]	<7	<7	Y	[mg/kg]	50	47
K_2O	[mass%]	0.6	1.7	Nb	[mg/kg]	55	45	Zn	[mg/kg]	45	47
P_2O_5	[mass%]	0.0	0.1	Nd	[mg/kg]	<39	<39	Zr	[mg/kg]	78	91
LOI	[mass%]	13.2	10.8	Ni	[mg/kg]	<6	7				
Sum main elements		99.8	99.8	Pb	[mg/kg]	21	34				

The main elemental composition of both samples is similar and corresponds well to the mineralogical composition: The higher SiO_2 content of GMZ 02 corresponds to the higher quartz content, the higher K_2O content of GMZ 02 corresponds to the higher muscovite content and the higher MgO content of sample GMZ 01 corresponds to the higher smectite content. The C- and S-contents are low in both samples which according to Kaufhold and Dohrmann (2016) can be considered a favourable property for HLRW bentonites. Moreover, the measured values are almost identical to those measured by Briug (Zhang et al., 2022).

The main elemental composition was quantitatively compared with the mineralogical composition by assuming ideal chemical compositions of the minerals. Based on this ideal composition and the mineral contents determined by Rietveld refinement and IR, a theoretical chemical composition was obtained which was compared with the measured one. For the main component smectite, the exchangeable cations measured by Briug (Zhang et al., 2022) were considered. Both samples showed negative CaO and Na_2O contents but positive SiO_2 contents which suggests that the content of clay minerals and feldspar could be lower by 2–4 mass% and that of quartz and cristobalite 2–4 mass% higher. This finding is in-line with IR spectroscopy which provided significantly less smectite (−10 mass%) and more cristobalite (+10 mass%). Comparing the XRD and IR results with the chemical composition as explained above suggests that the real values are in between both methods. Results obtained by this chemical correction are given in Table 3.5 (right). Overall, however, a good correlation of the theoretical mineralogical composition and the XRD results indicates the validity of Rietveld refinement results.

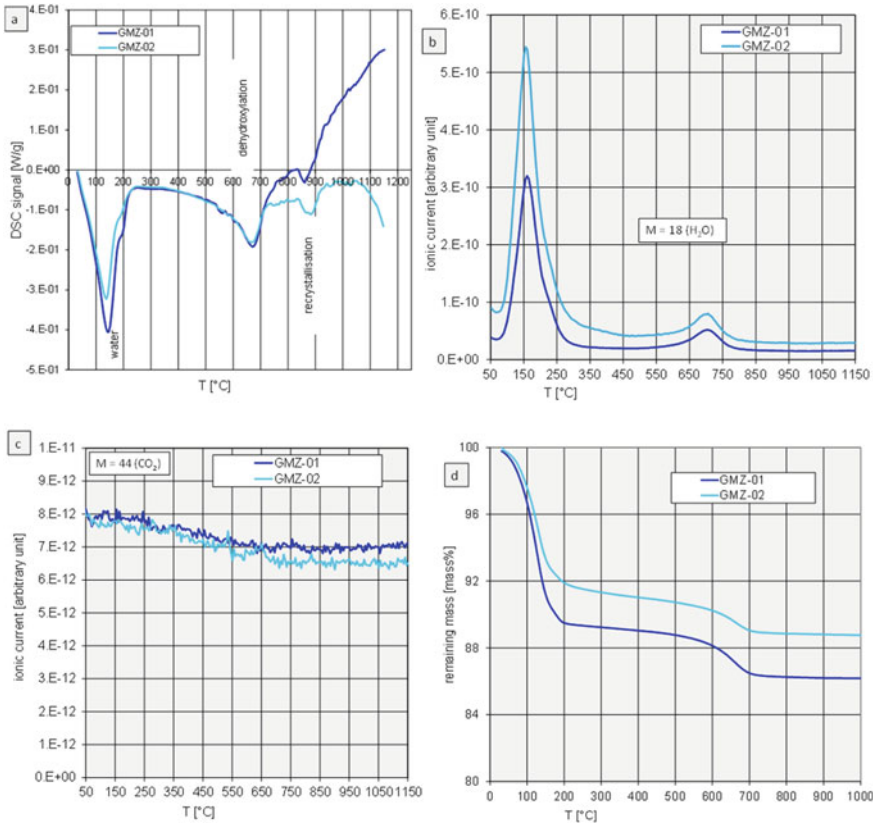

Fig. 3.20 Thermal analysis of the two bentonites (**a** calorimetric curves, DSC; **b** mass spectrometry mass 18; **c** mass spectrometry mass 44; **d** thermal gravimetry, TG)

The trace elemental composition of both samples is quite similar. The somewhat higher Rb content of sample GMZ 02 can be explained by the higher muscovite content (muscovite is known to incorporate Rb). All other trace elements are quite low in concentration. The low concentration of the transition metals, as an example, can be explained by the low Fe content of the material.

Differential scanning calorimetry expectedly showed an endothermic peak at about 130 °C (Fig. 3.20a) corresponding to dehydration. The shoulder at higher T points towards a mixed interlayer composition. At 573 °C a small peak was observed which can be explained by the transition of α- to β-quartz. The dehydroxylation (DHX) temperature is at about 670 °C which is commonly explained by cis-vacant smectites. This DHX temperature is typical of Fe-poor smectites (Kaufhold et al., 2017) which, therefore, is in accordance with the chemical data presented above.

The IR spectra of the samples are shown in Fig. 3.21. The quantitative data is shown in Table 3.5. By IR less smectite was found in both samples but higher cristobalite

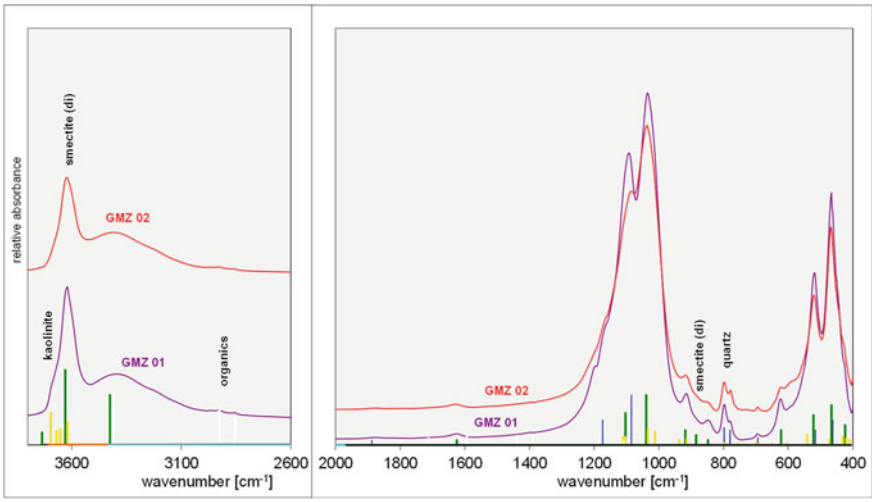

Fig. 3.21 IR spectra of both GMZ samples (green: dioctahedral smectite, yellow: kaolinite, white: organic material, blue: quartz)

contents. Comparing this data with the chemical composition, however, shows that too few SiO_2 is present in the samples to validate the high cristobalite contents. Therefore, the XRF-corrected XRD-Rietveld numbers (Table 3.5) are closer to the Rietveld results. IR spectroscopy, on the other hand, proved the presence of a trace of kaolinite (0.5 mass%) in sample GMZ 01. Such small amounts are below the XRD detection limit and hence could only be identified by IR. A couple of bands are indicative of some organic materials present but they are rather low in intensity. Accordingly no CO_2 was found in the mass spectrometer curve (Fig. 3.20c) which points to organic matter contents well below 0.1 mass% (which in turn corresponds to the LECO data, Table 3.6).

3.3 Geochemistry (Bentonite)

Janis Pingel, Thorsten Schäfer, Yasmine Kouhail, Muriel Bouby, Frank Heberling, Nikoletta Morélova, Madeleine Stoll, Stephanie Kraft, Nadine Gill, Claudia Joseph, Horst Geckeis

Bentonites are considered as reference buffer materials for high-level radioactive waste repository concepts notably in crystalline rock. In this regard, they represent essential barriers in the repository near-field. Within this section, various investigations on GMZ bentonite (see Sect. 3.2), which is discussed for Chinese disposal concepts, are described:

- related to the potential erosion behaviour when contacted with simulated granitic or natural groundwaters,
- dealing with radionuclide (^{3}H, ^{36}Cl, ^{137}Cs, ^{60}Co) diffusion through a magnetite/GMZ layer simulating radionuclide migration under conditions where the waste container is corroded.

Experimental results are partly compared with results obtained for similar investigations using Wyoming bentonite (MX80).

3.3.1 Erosion Experiments

A repository concept in crystalline rock relies on the bentonite barrier in different respects: (1) the swelling clay restricts the transport of water and potentially corroding groundwater constituents such as sulphide to the canister surface and (2) in case of canister failure it acts as a strong sorbent against radionuclide transport. Together with the corrosion-resistant container, the bentonite buffer represents an essential barrier responsible for the isolation and containment of highly radioactive material. In Scandinavian safety case considerations, the potential erosion of the bentonite buffer due to the intrusion of low mineralized glacial melt or meteoric water is considered a relevant scenario (SKB, 2011).

Within the present study GMZ bentonite erosion is examined

(1) for raw and homoionized GMZ (GMZ 01 and GMZ 02) samples contacted with natural low mineralized groundwater from the Grimsel Test Site (GTS, Switzerland) ($I = 1.6$ mmol L^{-1}; see composition in Schäfer et al. (2004), Table 1) and
(2) by contacting raw and impurified bentonite (GMZ 01) with a simulated groundwater from the Beishan site ($I = 39$ mmol L^{-1}; $[Ca^{2+}] = 2$ mmol L^{-1}; see composition in Table 3.9).

3.3.1.1 GMZ Erosion in Low Mineralized Water

Experiments conducted Five erosion experiments were conducted within the scope of this work (see Table 3.7). Experiments were set up with pellets of natural GMZ 01, GMZ 02 bentonite (comp. Sect. 3.2), or GMZ 01-derived clay fraction sodium-homoionized smectite (Na-smc) mixed with different quantities of accessory minerals (SF800 quartz, $Ø = 2\,\mu m$ (HPF, 2015); AGR40 bassanite, $Ø = 10.8\,\mu m$ (CASEA,

Table 3.7 Overview of major properties for the conducted erosion experiments. A more detailed overview of the mineralogical composition of the raw bentonites can be found in Sect. 3.2

	raw GMZ 01	raw GMZ 02	90/10 (GMZ 01)	2 wt.% bassanite (GMZ 01)	5 wt.% bassanite (GMZ 01)
Bulk density (g/cm^3)	1.85	1.84	1.78	1.76	1.77
Smectite cont. (wt.%)	73	56	90	88	85
Accs. quartz (wt.%)	13	17	10	10	10
Accs. bassanite (wt.%)	–	–	–	2	5

2013). Here, the aim was to investigate the different swelling and erosion behaviour of the natural (raw) bentonites compared to the impact of accessory minerals on the artificial Na-smc. With that, 10 wt.% quartz was chosen for each of the three artificial samples as it resembles a typical amount of quartz in many natural bentonites (see Sect. 3.2 or e.g. (IAEA, 2013)). In the case of the accessory bassanite, the goal was to supply the systems with an additional interior calcium source for the cation exchange process to positively influence the system concerning erosion resistance and therefore barrier integrity. Samples were placed into an artificial Plexiglas-built parallel plate, non-sloped chamber of 85 mm diameter and 1 mm aperture and were continuously flushed for 77 days with a constant flow rate of 50 ± 1 µl/min of low mineralized (calcium concentration: 5.73 ± 0.46 mg/L) natural Grimsel Ground Water (GGW), extracted from the LIT Pinkel surface packer at the Grimsel Test Site (GTS). Sample water was extracted from the individual setups periodically and was stored refrigerated for further treatment or analysis, respectively. Hydrochemical (IC, ICP-OES, pH, electrical conductivity) and particle characterization analyses (NTA; Nanoparticle Tracking Analysis—Malvern Panalytical NanoSight NS300) were conducted continuously on sampling aliquots. Swelling pressure time-resolved evolution was monitored in situ (TekScan® pressure sensors). Sample pellets, in turn, were made from ca. 1 g material with a target bulk density of 1.8 ± 0.05 g/cm^3, referring to previously conducted experiments, e.g. (Kiviranta and Kumpulainen, 2011; Svensson et al., 2011; Bouby et al., 2020).

Results

Swelling and pressure evolution

In the case of the GMZ 01 bentonite, the expanded material showed a mostly homogeneous distribution with an insinuated tear-shaped form towards the outlet (see Fig. 3.22). Thereby, highly visible erosion streaks emerged from the beginning of the experiment. A maximum swelling radius was achieved with ca. 30 ± 4 mm after

56 days (see Fig. 3.23). Initial contact pressure (total force measured relative to the contact area upon the pressure sensor) peaked at up to 532 kPa but continuously declined afterwards, reaching zero pressure after 56 days. The expanded GMZ 02 showed a rather diffuse transition between its internal sections. However, as for the GMZ 01 bentonite, visible erosion streaks were observed from the start of the experiment towards the outlet. A maximum radial swelling was reached at 21 ± 1 mm after 35 days. Due to the comparably lower smectite content, an initial contact pressure peak was measured with 449 kPa, reaching zero pressure after 28 days. With an initially similar swelling pace as observed for the raw GMZ bentonites, maximum radial swelling was reached at 16 mm after 10 days for the 90/10 (GMZ 01) sample. Furthermore, visible erosion started after 7 days, perceptibly visible as an emerging whitish ring at the gel/water interface. Subsequently, significant amounts of clay were washed out after 28 days, leaving a whitish framework of quartz grain skeleton within the chamber. While the erosion process was retarded compared to the 90/10 (GMZ 01) sample, a similarly pronounced erosion event was observed for the 2 wt.% bassanite (GMZ 01) sample, starting after ca. 14 days, although, the gel/water interface seemed to be fringier in the latter case. In contrast, no significant erosion was observed for the 5 wt.% bassanite (GMZ 01) setup. Due to a higher calcium supply by the total mass of dissolving bassanite and an inferior swelling capability of Ca-montmorillonite, the swelling was severely reduced, reaching a maximum swelling distance of ca. 7 ± 0.5 mm. Regarding the contact pressure, the artificial samples were measured with much less pronounced values than the raw GMZ bentonites, peaking between 200 and 300 kPa. Furthermore, samples showed a continuous pressure decline afterwards, albeit slower than the raw GMZ bentonites. Here, zero pressures were reached after 14 or 28 days in the case of the 90/10 (GMZ 01) and 2 wt.% bassanite (GMZ 01) samples, respectively. Of all samples, though, the 5 wt.% bassanite sample was the only stabilizing at around 100 kPa, reaching no zero pressure values during the experiment.

Hydrochemical propagation

No significant pH changes in eluates were observed for the raw GMZ bentonites over time, ranging at ca. ± 0.2 with respect to the applied GGW (see Fig. 3.24). Concerning the artificial samples, though, especially the erosive 90/10 (GMZ 01) and 2 wt.% bassanite (GMZ 01) samples were measured with more pronounced pH value decrease during the erosion events (pH ~ 6.9). While pronounced conductivity increase was measured for the initial phases of Ca-carrier setups at up to 195 µS/cm for the 5 wt.% bassanite (GMZ 01) sample, no significant variances were measured for the other setups. Thus, no direct correlation between the electrical conductivity and erosion events could be traced. Eventually, all samples adjusted within proximity of the applied GGW concerning pH: 7.4 ± 0.1 and electrical conductivity: 112 ± 3 µS/cm. Note that all experiments were conducted under atmospheric conditions, thus affecting the pH of the applied GGW.

Due to the cation exchange process, calcium was stripped from the applied GGW for all samples. Thereby, the most pronounced concentration decrease was

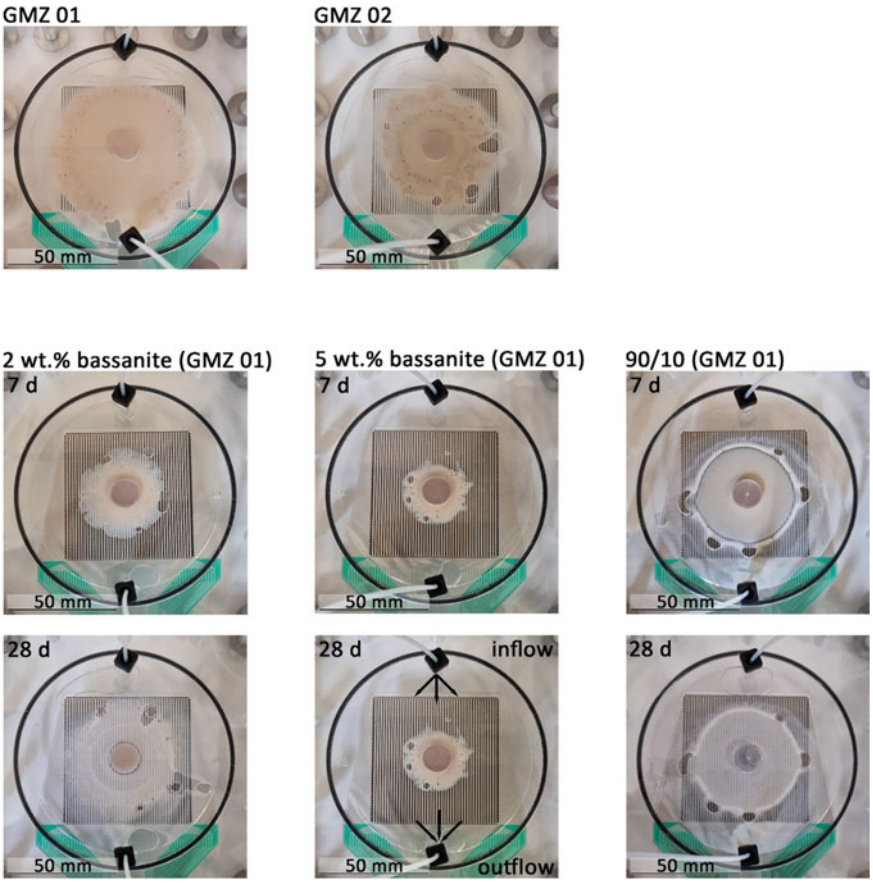

Fig. 3.22 Top view on applied samples after 7 or 28 days, respectively

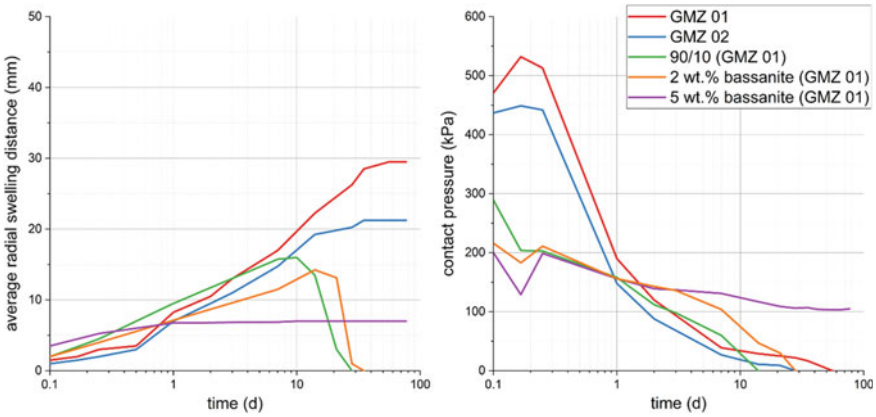

Fig. 3.23 Radial swelling distance (left) and contact pressure (right) over time

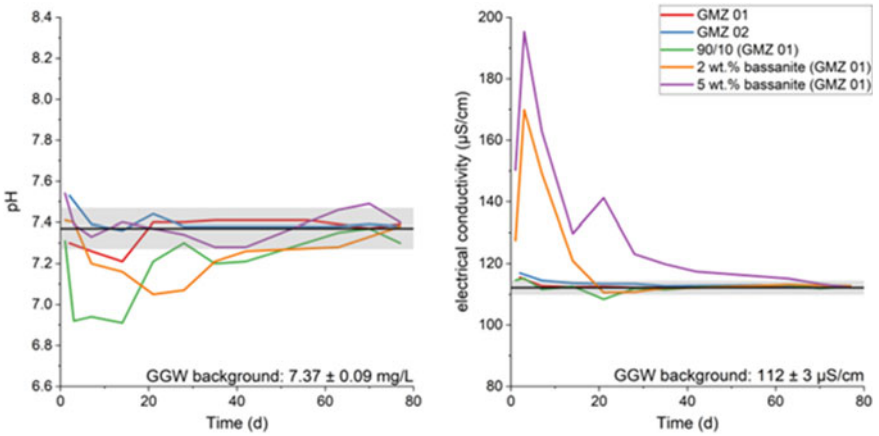

Fig. 3.24 All setups pH and electrical conductivity evolution over time

measured for the 90/10 (GMZ 01) sample (see Fig. 3.25), where almost all calcium was extracted from the aqueous phase (Ca ≈ 0.3 mg/L), correlating to the observed erosion event between days 7 and 28 (see Fig. 3.25). Decreasing concentrations were also measured for the 2 wt.% bassanite (GMZ 01) setup (Ca ≈ 1.3 mg/L) and the GMZ 01 setup (Ca ≈ 3.0 mg/L) after 21 and 35 days, respectively. However, these were less pronounced due to the release of calcium by the dissolving artificial Ca-carrier (dissolution rate ca. 4.5 ± 0.5E-4 mol/g·s (Brandt and Bosbach, 2001) or the initial $Na^{+}/Ca^{2+}/Mg^{2+}$ surface charge in the case of the raw bentonites. In contrast, the 5 wt.% bassanite (GMZ 01) sample even experienced a slight concentration increase, however within the measurement uncertainty area, likely due to the higher amount of added bassanite and, thus, calcium release.

Unlike calcium, the artificial samples were measured with pronounced concentration peaks in the case of sodium during the initial phases of the respective experiments. Due to the cation exchange of the Na-smc, sodium concentration peaked at up to 34.9 mg/L after 3 days in the case of the 5 wt.% bassanite (GMZ 01) setup. Over time, concentrations decreased as the cation exchange proceeded in favour of Ca^{2+}, and subsequently, less sodium was released. While slightly raised values were measured at the beginning of the raw GMZ bentonite setups, lower initial surface cation Na-occupancy (see Sect. 3.2) and exchange capacity (see Table 3.8) resulted in the inferior release or exchange, respectively.

While slightly increased values were measured for magnesium and potassium at the beginning of each experiment, values did not exceed 0.5 mg/L with respect to the applied GGW (Mg = 0.014 mg/L, K = 0.141 mg/L). While the GMZ 02 and artificial Na-smc experiments adjusted within proximity of the applied GGW shortly after the beginning, the GMZ 01 setup was measured with an additional magnesium and potassium peak, coinciding with the concentration decrease at around 35 days.

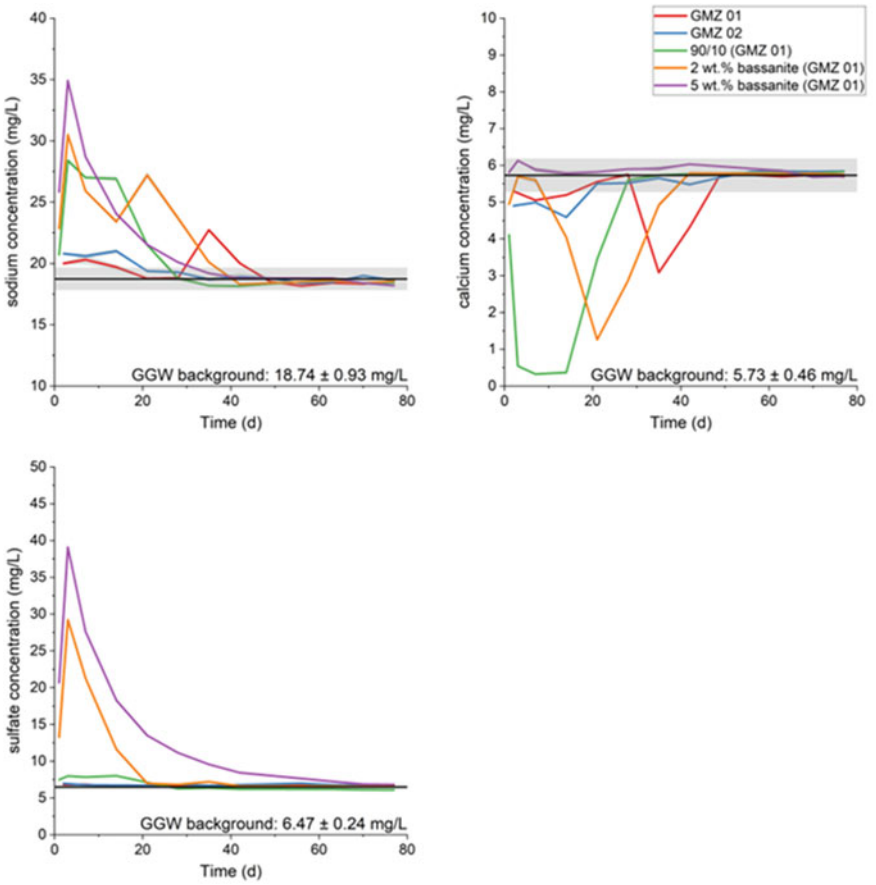

Fig. 3.25 Sodium, calcium and sulphate concentration over time for all setups

In the case of silicon and aluminium, increased concentration values were correlated with the respective particle releases of all setups, especially pronounced for the 90/10 (GMZ 01) and the 2 wt.% bassanite (GMZ 01) experiment.

While different amounts of bassanite were added for the 2 wt.% and 5 wt.% bassanite experiments, different high sulphate peaks of ca. 30 and 40 mg/L were measured during the initial phase of the experiments. As the added bassanite slowly dissolved, both setups adjusted within proximity of the applied GGW (6.47 $\pm$ 0.24 mg/L) after ca. 21 and 70 days, respectively. As the GMZ 01 and GMZ 02 raw bentonites do not contain natural amounts of any soluble sulphate Ca-carrier like gypsum or anhydrite, no SO_4^{2-} release was measured during the experiments.

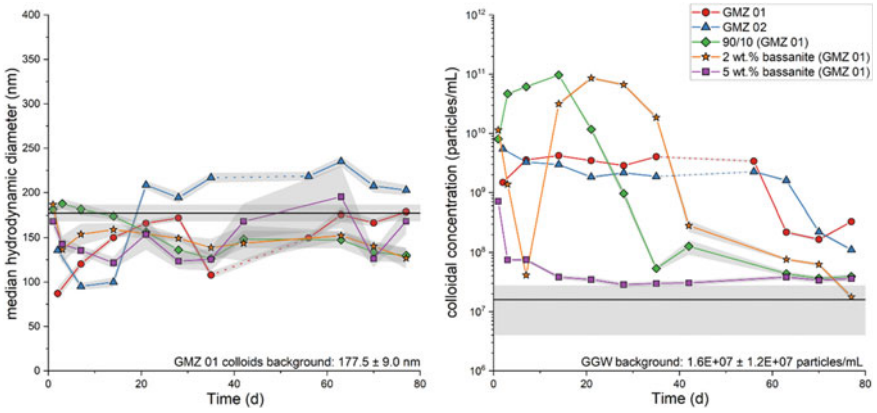

Fig. 3.26 Median hydrodynamic diameter (left) and colloidal concentration (right), measured by NTA. An intentional flow stop for GMZ 01 and GMZ 02 between days 35 and 56 is marked as dotted lines

Particle characterization

Concerning particle characterization in the eluates in contact with the bentonite source, similar median hydrodynamic diameters were measured for all setups conducted, ranging primarily between 100 and 200 nm (see Fig. 3.26), which is near the measured background of GMZ 01 colloids (177 ± 9 nm). While no dependencies regarding the swelling and erosion behaviour of the setups were observed, a slightly increasing trend was observed for all setups. This, however, is likely linked to an easier release of smaller particle size during the initial swelling phase of the experiments.

Distinct colloidal particle concentrations were measured for the different setups conducted. Thereby, the raw GMZ 01 and GMZ 02 setups were measured with a similar but stable colloidal release of ca. 2.4 ± 1.7E+09 particles/mL during the first 60 days of the experiments (see Fig. 3.26). Afterwards, a decline towards lower ca. 2.0E+08 particles/mL concentrations was likely induced by an intentional flow stop of 3 weeks (days 35–56) and a prolonged exchange time for the surface cations. In contrast, the 90/10 (GMZ 01) setup was measured with significantly increased concentration values during the erosion event, peaking at 9.7 ± 0.2E+10 particles/mL after 14 days. Afterwards, particle release decreased due to the significant washout of clay material. Thus, reaching concentration values within proximity of the applied GGW after ca. 35 days. In the case of the Ca-carrier experiments, 2 wt.% bassanite was non-sufficient to stabilize the system from erosion. Thus, increased particle concentrations of up to 8.6 ± 0.5E+10 per mL were measured. However, due to the released calcium, the process was retarded compared to the 90/10 (GMZ 01) setup. Eventually, though, a significant amount of clay was also washed out, decreasing the number of emitted colloids over time. Contrastingly, 5 wt.% bassanite successfully enhanced the system integrity by supplying sufficient amounts of

Table 3.8 CEC (meq/100g) and element concentration (%) of major exchangeable cations for different sections harvested after the respective experiments. The relative abundance was thereby calculated concerning the ion's mol-weight

	CEC (meq/100 g)	Na^+ (%)	Ca^{2+} (%)	K^+ (%)	Mg^{2+} (%)
GMZ 01 (raw)	75.6 ± 0.6	66.2 ± 2	21.2 ± 0.1	0.6 ± 0.1	11.4 ± 0.1
GMZ 02 (raw)	56.9 ± 0.8	67.2 ± 3.4	22.2 ± 0.1	1.0 ± 0.02	9.4 ± 0.3
100% Na-smc (GMZ 01)	88.5 ± 2.7	97.3 ± 1.7	1.9 ± 0.01	0.4 ± 0.01	1.35 ± 0.01
GMZ 01 (core)	78.9 ± 0.1	58.9 ± 3.8	26.1 ± 0.2	1.1 ± 0.03	13.1 ± 0.1
GMZ 01 (inner ring)	71 ± 4	25.4 ± 2.4	57.3 ± 0.1	0.7 ± 0.01	15.2 ± 0.1
GMZ 01 (outer ring)	67 ± 1.9	14.3 ± 2.1	78.1 ± 0.5	0.7 ± 0.04	5.4 ± 0.03
GMZ 02 (core)	32 ± 9.3	58.5 ± 8.6	25.3 ± 0.02	2.4 ± 0.3	13.4 ± 0.1
GMZ 02 (inner ring)	40.2 ± 2.2	44 ± 9	40.2 ± 0.2	2.7 ± 0.1	12.5 ± 0.04
GMZ 02 (outer ring)	47.7 ± 0.4	33.3 ± 7.7	53.5 ± 0.4	2.3 ± 0.1	10.2 ± 0.03
* GMZ 01 2 wt.% bassanite (inner ring)	15.4 ± 0.1	< 10.6	70.4 ± 0.1	0.7 ± 0.1	17.2 ± 0.1
* GMZ 01 2 wt.% bassanite (outer ring)	6.6 ± 0.1	< 11.2	68.5 ± 0.1	0.5 ± 0.1	18.6 ± 0.1
GMZ 01 5 wt.% bassanite (combined)	75.4 ± 0.4	0.8 ± 0.1	91.8 ± 0.3	1.6 ± 0.01	5.6 ± 0.02

* Error-prone data due to low amounts of harvested material

calcium, thus increasing the cation exchange in favour of Ca^{2+}. Subsequently, low amounts of colloids were released with concentration values close to the natural concentration of the GGW contact water.

By applying the NTA quantification approach of Mehrabi et al. (2017), mass balances were approximated for all experiments conducted. The approach thereby evaluates the NTA-based data by considering the particle size distribution histogram in a given size range (bins). Subsequently, the average number concentration of each bin was multiplied by its associated spherical particle diameter d_i and thereof its respective particle volume $\overline{v}_{c,i}$. With a typical montmorillonite density of (ρ = 2.35 g/cm^3, e.g. (Duda et al., 1990)), mass approximation was performed by summing each bin:

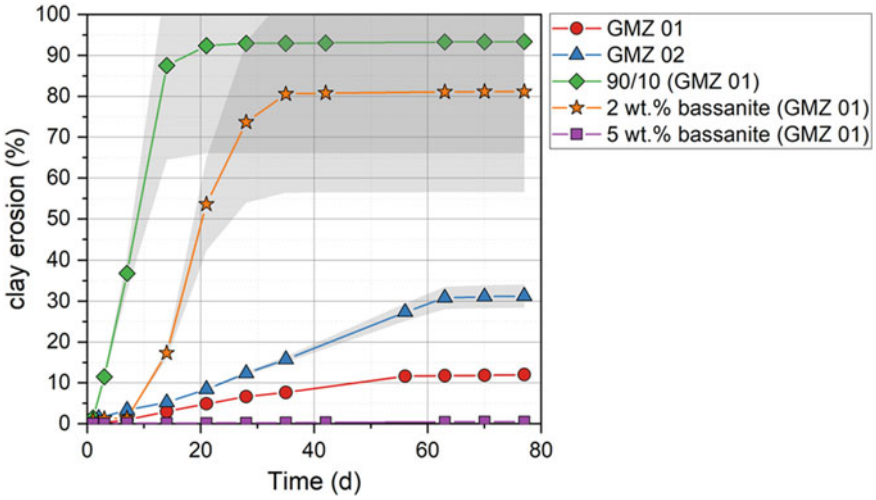

Fig. 3.27 Approximated clay erosion (%) as cumulative curves based on the calculation using Eq. 3.18

$$m_c = \rho \sum_{i=1}^{n} \left(\overline{v}_{c,i} \frac{1}{6} \pi d_i^3 \right) \tag{3.18}$$

In order to validate the method, a five-point calibration of GMZ 01 clay colloids was conducted, showing an overall uncertainty of ca. ± 10% concerning the target values.

Figure 3.27 shows the cumulative masses of all experiments conducted to have a high consensus with the observed clay erosion (comp. Fig. 3.22). While the highly erosive setups of 90/10 (GMZ 01) and 2 wt.% bassanite (GMZ 01) were calculated to have lost 94% and 81% ± 10% of their initial clay material, with most material being eroded within the first 20 to 35 days, the 5 wt.% bassanite (GMZ 01) setup was calculated to have lost a mere 0.5% of its initial clay material due to the enhanced calcium supply. In the case of the raw GMZ bentonites, the GMZ 01 was calculated with a lesser clay release of 12.6% compared to the GMZ 02, which eventually lost 32.6% of its original clay material during the experiment.

With respect to the increased Al, Si and Mg concentrations measured, which were especially pronounced for the 90/10 (GMZ 01) and 2 wt.% bassanite setups, Fig. 3.28 shows the hydrochemical data correlated with the respective colloidal mass. Thus, the NTA determined colloidal size fraction released during erosion (comp. Fig. 3.26) is clearly not removed during the pre-filtering with 0.45 µm cellulose acetate filters and partly measured in the acidified samples. Unfortunately, for these experiments no unfiltered aliquots for quantitative analysis of the erosion masses were measured. However, the clear correlation of structural elements (Al, Si, Mg) with the colloidal mass of the samples indicates the release of clay colloids. However,

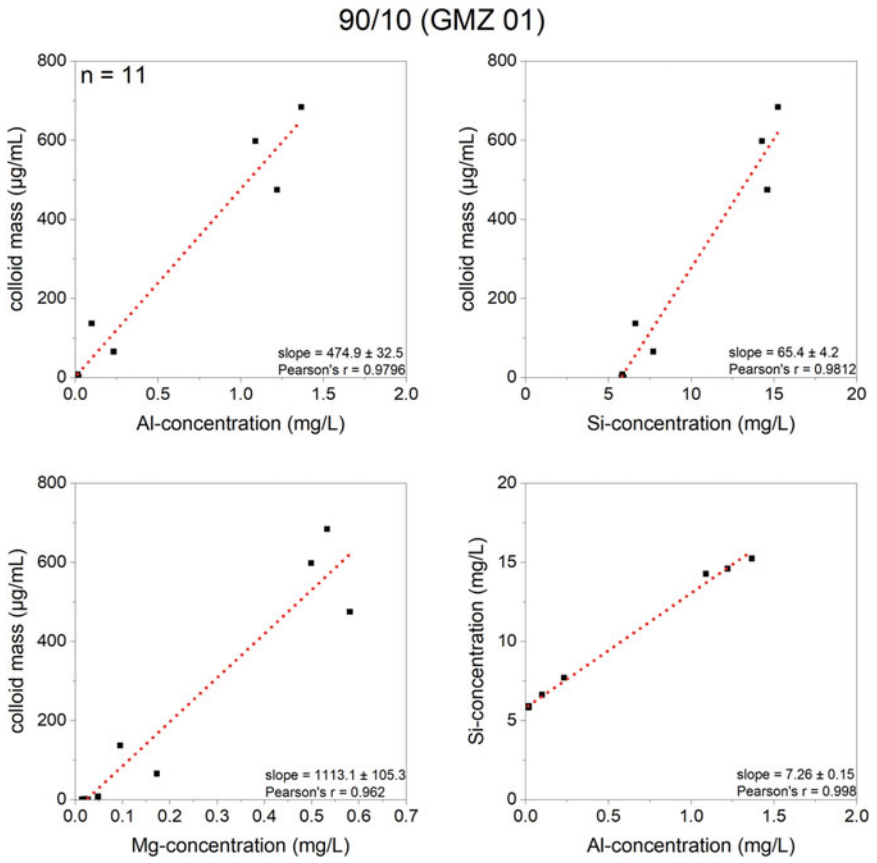

Fig. 3.28 Correlation diagrams of the Al, Si and Mg concentrations with the calculated erosion masses, exemplified for at 90/10 (GMZ 01) setup

as higher Si concentrations were measured with respect to the structural Al/Si ratio of montmorillonite (ca. 1:4), an additional but subordinated source of quartz colloids can be expected. In case of the raw bentonites, no such surplus of silicon was measured, though (Al/Si ratio of ca. 1:4).

Cation exchange capacity and ion occupancy

After each experiment, samples were harvested from the remnant material within the erosion chambers.

Thereby, different sample sections were collected (core, inner ring, outer ring) to investigate potential differences within the expanded material (see Fig. 3.29) concerning changes in cation exchange capacity (CEC) and occupancy of major cations at the montmorillonite surface. As only small amounts of sample material were originally emplaced (ca. 1 g), the Cu(II)-trien method after Lorenz et al. (1999) and adjusted by Dohrmann et al. (2012) was applied, as hence even small amounts of sample material

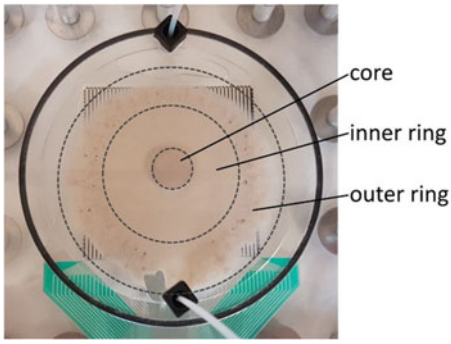

Fig. 3.29 Exemplified for the GMZ 01 bentonite after 28 days (comp. Fig. 3.22); the image highlights the different sections (core, inner ring, outer ring) harvested after the experiments

(<100 mg) can be used to determine the CEC. Table 3.8 compares measured CEC values and major cation concentrations for all harvested sample sections and the raw material.

CEC measurements of the raw bentonites determined values of 75.6 ± 0.6 meq/100g in the GMZ 01 bentonite and 56.9 ± 0.8 meq/100g in the GMZ 02 bentonite, which is in accordance with the data presented in Sect. 3.2. Furthermore, the initial occupancy of the surface cations was also determined by applying ICP-OES. Thus, showing the $Na^{+}/Ca^{2+}/Mg^{2+}$ exchangeable cation composition (CEC) of the raw GMZ bentonite material and the artificial montmorillonite being primarily Na-exchanged.

Due to the cation exchange process in contact with the applied GGW and/or bassanite dissolution, surface cations were exchanged differently for the harvested sections. Thereby, the setups solely flushed with GGW were measured to have had an increasingly higher surface cation exchange in favour of calcium towards the outer ring sections due to the selective sorption of calcium from the applied GGW and slow diffusion process through the compacted clay material. However, cations were not completely exchanged during the experiments, leaving $Na^{+}/Ca^{2+}/Mg^{2+}$ ratios of ca. 14/78/5% in the case of the GMZ 01 and 33/54/10% in the case of the GMZ 02 setup for their respective outer ring sections. Due to the significant clay erosion of the 90/10 (GMZ 01) setup, a single sample of the remaining quartz grains was harvested. Here, a low CEC value of ca. 3 meq/100g was measured, with major cations being below the detection limit of the ICP-OES. Differently, cation exchange was observed to be vice versa for the 2 wt.% bassanite setup, with slightly higher Ca values in the inner ring section. However, as a significant clay release was observed, no core section was harvested (comp. Fig. 3.22), and considerably reduced CEC values were measured. Due to the observed low swelling process of the 5 wt.% bassanite sample, only a single sample was harvested. While the sample CEC was measured to be similar in comparison to the raw bentonites, the exchange in favour of calcium was enhanced (91.8 ± 0.3%) due to applied GGW (external supply) and the bassanite-related calcium (inner supply), demonstrating the efficiency of stabilization against erosion in this sample.

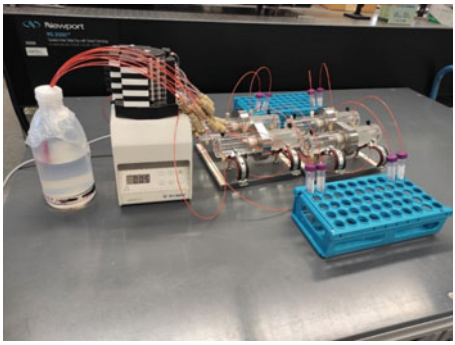

Fig. 3.30 Double-sided erosion test cells with bentonite pellets

Table 3.9 Composition of simulated Beishan groundwater acc. to Zhu et al. (2022) and as prepared (note that there is a difference of nominal and actual concentrations for Ca); n.a.: not analysed

Cations	mg L^{-1} acc. to ref.	mg L^{-1} acc. to analysis	Anions	mg L^{-1} acc. to ref.	mg L^{-1} acc. to analysis
Na^+	571	567 ± 3%	F^-	1.15	0.80 ± 3%
K^+	10.9	7.8 ± 1.2%	Cl^-	589.7	585 ± 5%
Mg^{2+}	20.5	21.2 ± 1.7%	NO_3^-	5.57	4.8 ± 4%
Ca^{2+}	86.8	80 ± 1%	SO_4^{2-}	590.9	570 ± 5%
pH	8.5		HCO_3^-	125	n.a.

3.3.1.2 GMZ Erosion in Simulated Beishan Groundwater

Experiments conducted Two GMZ bentonite pellets were prepared by hydraulic pressing (19 mm diameter, 10 mm height, dry density: 1,6 g/cm^3) and emplaced in separate compartments of a transparent double-sided erosion cell (see Bouby et al. (2020) and Fig. 3.30). The pellets were confined between a PEEK spacer and a porous stainless-steel filter (pore width: 20 μm) simulating a scenario of a fracture filled with porous fracture-filling minerals.

Synthetic porewater from Gansu Beishan (Table 3.9) was circulated for 155 days with a rate of 3 μL/min at pH = 8.5. Visual inspection through the transparent reaction cells shows that hydration of the bentonite is complete after 3 days.

Results Following the evolution of the porewater solution over time shows constant concentrations for most constituents. A slight decrease in Ca^{2+} and Mg^{2+} concentration by ~ 10 and 15%, respectively, suggests sorption to the GMZ bentonite. On the other hand, the Na^+ concentration in the circulating porewater increases by about 8% indicating an ion exchange reaction where Na^+ is released and Ca^{2+} is enriched in the bentonite. An initial decrease in K^+-concentration is followed by a continuous increase. The Sr^{2+} concentration is increasing as well steadily (not shown

in Fig. 3.31) over the entire observation period even though at a very low concentration level. All those findings point to an ongoing ion exchange reaction, which is not yet in equilibrium after 200 days, even though bentonite saturation was achieved after 3 days by visual inspection of the transparent cells. No variation could be seen for the anion concentrations and only a minor pH change from 8.54 to 8.37 is observed. Al(III) could be taken as a clay colloid erosion indicator (as, e.g. seen in Bouby et al. (2020)). Respective concentration data analysed by ICP-MS are, however, very much scattered and an elution peak during the initial bentonite swelling process is not detectable. A slightly transient increase of the Si concentration might be interpreted as a temporary release of clay colloids. Bentonites are, however, known to contain reactive and soluble silica components (see, e.g. Kaufhold et al. (2020)) so that the Si-elution peak could also be due to silicate leaching. However, no reactive silica species are reported for GMZ bentonite (see Kaufhold et al. (2020), Sect. 3.2). No other indicators for clay colloids were visible. The initial erosion rate determined with the same setup for raw MX80 bentonite and a low mineralized groundwater simulate ($I = 1.16$ mmol L^{-1}, $[Ca^{2+}] = 0.05$ mmol L^{-1}) after 342 days was at 0.043 $\pm$ 0.002 kg y^{-1} m^{-2} (Bouby et al., 2020). The findings made in experiments with simulated Beishan groundwater ($I = 39$ mmol L^{-1}, $[Ca^{2+}] = 2$ mmol L^{-1}) are in-line with previous studies suggesting that Na^{+} and Ca^{2+} concentrations larger than critical coagulation concentrations ($CCC_{Na} = 10$–100 mmol L^{-1}; $CCC_{Ca} = 0.1$–1 mmol L^{-1}, (García-García et al., 2007; Seher et al., 2020) prevent significant bentonite erosion. As a next step, the simulated Beishan groundwater will be exchanged against a low mineralized groundwater from the Grimsel Test Site in order to study GMZ bentonite erosion under the same conditions.

3.3.2 Diffusion Experiments

Different materials are considered for waste canisters in deep geological repositories (DGR) in crystalline rock. While Finland and Sweden foresee "corrosion-resistant" copper-coated canisters, other countries discuss as well "corrosion-acceptable" concepts consisting of thick, double-walled steel containers (e.g. outer shell made of carbon-steel, inner shell made of stainless steel) (see, e.g. Pospiskova et al. (2017)). In the latter case, the iron-based canisters are considered to corrode in contact with groundwater over a period of thousands of years partly at the elevated temperatures of the thermal phase. Under those conditions, secondary iron phases such as magnetite are expected to form and dissolved Fe(II) species may react with the bentonite (see, e.g. Chaparro et al. (2021); Féron et al. (2009); Kaufhold et al. (2020)). Thus, radionuclides released from the waste over longer time-scales would not be in contact with pristine bentonite only, but with a corrosion-induced alteration layer adjacent to the bentonite. In the present study, radionuclide diffusion through a magnetite/bentonite interface is studied in order to assess the long-term barrier function of an altered bentonite.

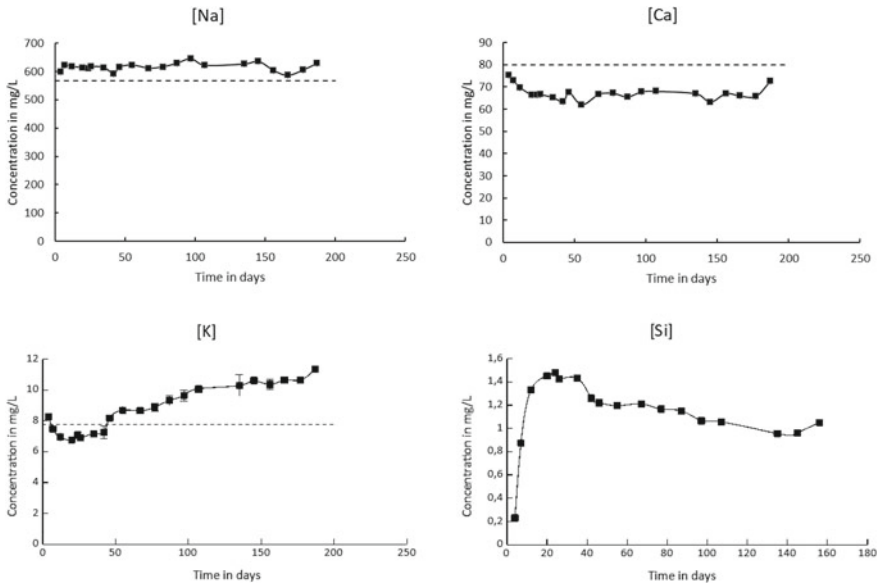

Fig. 3.31 Concentration evolution of some groundwater simulate constituents during the erosion experiment; dashed lines indicate the initial concentration level

3.3.2.1 Experiments

Four through-diffusion experiments (Fig. 3.32) through GMZ bentonite and through a mixed porous medium of magnetite and GMZ bentonite were performed using a pre-equilibrated synthetic pore water of Gansu Beishan (composition described in Table 3.10) at room temperature at a reservoir circulation flow rate of 0.4 mL/min. 0.4 mM $NaHCO_3$ were added to the porewater after the necessary percolation with argon to minimize dissolved oxygen. After a pre-equilibration step of 3 weeks in contact with bentonite in a glove box under Ar atmosphere, the composition of the pore water was measured by ICP-OES and ion chromatography, and pH and Eh were measured and reported in Table 3.10. The pore water in the high reservoirs of the mixed porous media was additionally equilibrated with magnetite at 12.5 mg/L.

Cylindrical pellets of GMZ 01 bentonite (25.64 mm diameter, 10 mm height or 8.04 mm height) and magnetite (25.6 mm diameter, 2.2 mm height) were compacted using a hydraulic press with a dry density of 1.6 and 1.7 g/cm^3, respectively. Magnetite was prepared acc. to Schwertmann and Cornell (2000). Briefly, equimolar aqueous solutions of $FeCl_2$ and $FeCl_3$ were mixed, and pH adjusted to 8.25–9 using a NaOH solution. The precipitate was washed and dialysed. The dried solid was poorly crystalline with crystallite sizes of ~ 10 to 17 nm. The magnetite pellets were compacted in a glove box under argon atmosphere. Stainless steel diffusion cells were packed with a pellet of GMZ 01 bentonite or magnetite and bentonite in each cell with a stainless-steel filter (type 316L, 10 μm pore size) at each end of the

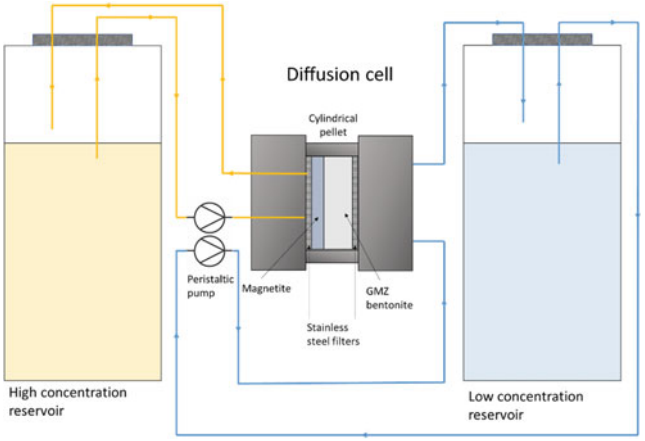

Fig. 3.32 Scheme of the setup of through-diffusion experiments

Table 3.10 Composition of the synthetic GMZ pore water in contact with groundwater from Gansu Beishan acc. to Wu et al. (2014) and after equilibration; n.a.: not analysed

Composition acc. to Wu et al. (2014)	Concentration (g L^{-1})	Composition* after equilibration with high conc. reservoir at start of the diff. experiment (g L^{-1})	Composition* in the high conc. reservoir at end of the diff. experiment (g L^{-1})
Na^+	1.102	1.346 ± 1%	1.200 ± 1%
K^+	0.015	0.019 ± 1%	0.019 ± 1%
Mg^{2+}	0.103	0.088 ± 5%	0.111 ± 1%
Ca^{2+}	0.484	0.358 ± 1%	0.458 ± 1%
Fe		0.0007 ± 9%	0.001 ± 2%
Si		0.008 ± 6%	0.005 ± 9%
NO_3^-	0.019	n.a.	n.a.
Cl^-	1.160	1.341 ± 5%	1.204 ± 5%
SO_4^{2-}	1.846	1.981 ± 5%	2.181 ± 5%
F^-	0.002	0.049 ± 5%	0.057 ± 5%
DIC	0.010	0.008 ± 2%	0.008 ± 2%
pH		7.36	7.24
Eh SHE (mV)		354 ± 50	257 ± 50

*Analytical data for solutions in the high concentration reservoir

cell. The magnetite/bentonite pellets were then pre-equilibrated for 4 weeks with the synthetic pore water.

The diffusion experiments through the bentonite and the mixed porous media of magnetite and GMZ bentonite were started in a glove box after the pre-equilibration by first using non-sorbing radiotracers (^{36}Cl and tritiated water HTO with an activity

of 1000 Bq/mL in the high concentration reservoirs) to investigate porosity and diffusion coefficients. The non-sorbing radiotracers were measured by liquid scintillation counting (LSC) using an LSC Ultima Gold XR cocktail (Perkin Elmer).

After out-diffusion of the non-sorbing tracers, the diffusion of the sorbing tracers $^{137}Cs(I)$ and $^{60}Co(II)$ was investigated. The experiments were carried out by using an activity of 10 kBq/mL of $^{137}Cs(I)$ (carrier free) or $^{60}Co(II)$ (carrier: 17 ng/mL Co) in the high reservoir of each cell. The low reservoirs were sampled periodically and the activities of $^{137}Cs(I)$ and $^{60}Co(II)$ were measured by gamma spectroscopy and diffusion coefficients were determined.

3.3.2.2 Results and Discussion

Figures 3.33, 3.34 and 3.35 contain experimental data of diffusion experiments performed so far. Only small variations in ion concentrations can be seen in the reservoir solutions after pre-equilibration of the simulated porewater (Wu et al., 2014) with the magnetite/bentonite samples (Table 3.10, 2nd column). Slightly increasing concentrations for Na^+, Cl^- and SO_4^{2-} suggest the dissolution of soluble compounds from the non-purified GMZ. On the other hand, a moderate initial decrease in Ca^{2+} concentration may point to an ion exchange process. Fe concentration establishes at a concentration level of ~0.01–0.02 mmol L^{-1}. Invariant pH points to an overall equilibrium during the diffusion experiment. The Eh value only slightly decreased during the experiment, showing that an overall redox equilibrium with magnetite within the entire diffusion setup was obviously not attained.

The effective diffusion coefficients and rock capacity factors were calculated from the analytical solution of Fick's second law using the experimental results of through-diffusion tests (see, e.g. Van Loon and Soler (2004)) and are summarized in Table 3.11. Note that in this simplified view, the heterogeneity of the magnetite/bentonite sample is not considered. Respective parameters have to be considered as a first indication for variations in diffusion properties in the bentonite due to the presence of magnetite. HTO diffusion parameters are comparable with the ones reported in Wu et al. (2014), with GMZ ($D_e = (1.12 \pm 0.06)$ x 10^{-10} m^2/s and $\alpha = 0.44 \pm 0.02$). From the HTO diffusion experiments, a slight increase of porosity can be stated for the magnetite/GMZ system as compared to the diffusion experiment with GMZ alone (0.536/0.448 for GMZ alone and 0.625/0.577 for magnetite/GMZ). This is to be expected as the magnetite will not undergo swelling as the bentonite does. The clear decrease of α derived from the Cl^--diffusion data as compared to the HTO experiment with GMZ is clearly due to the anion exclusion effect, restricting the accessible porosity of anions in the bentonite. It is remarkable that the anion exclusion effect strongly decreases in the magnetite/GMZ sample, i.e. the rock capacity factor increases. Such an effect was not expected and potentially points to some kind of a charge screening effect by dissolved Fe species, being released from the magnetite and interacting with bentonite.

Diffusion experiments with sorbing tracers $^{60}Co^{2+}$ and $^{137}Cs^+$ were only performed with GMZ/magnetite samples so far. Sorption coefficients (K_d-values)

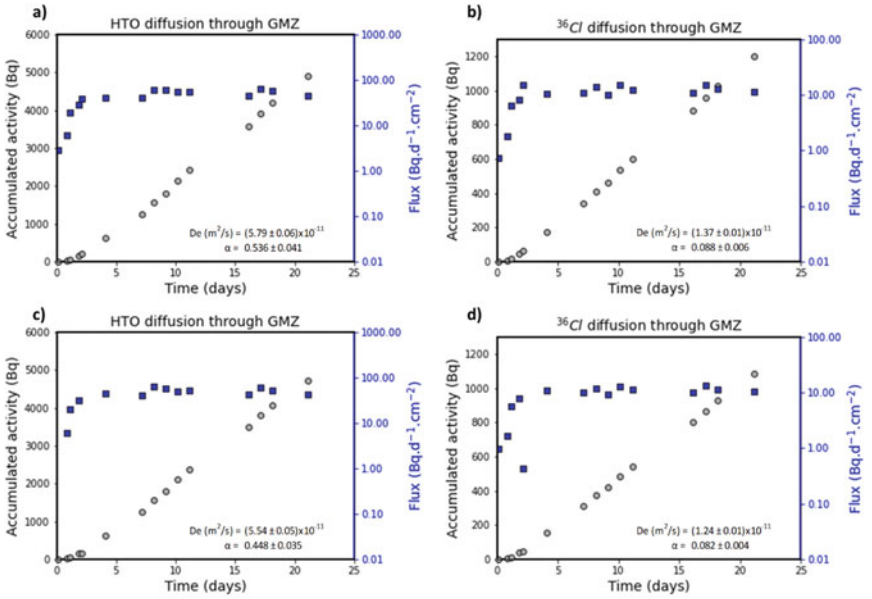

Fig. 3.33 Accumulated activity (in Bq) and flux (in $Bq.d^{-1}{\cdot}cm^{-2}$) as a function of diffusion time (in days) for HTO and ^{36}Cl through GMZ bentonite, effective diffusion coefficients and rock capacity factors in cell 1 (**a** & **b**)

derived from rock capacity factors α obtained from through-diffusion data should be considered preliminary for the same reason as discussed already above. Post-mortem analyses are under way to analyse diffusion profiles using the abrasive peeling technique (see Van Loon and Müller (2014)) and an improved diffusion modelling approach, taking the different material layers into account is currently tested.

The K_d-value for Cs derived from the rock capacity factor of this study matches perfectly with the sorption model from Bradbury and Baeyens (2002b), and the respective K_d-values derived therein for the diffusion in compacted bentonite (10 L/kg compared to 2.4 L/kg in the present study). Those results demonstrate that Cs-sorption does not differ much in a pure bentonite and a layered magnetite/bentonite system. The slightly lower K_d-value obtained from GMZ/magnetite experiments may as well point to a competing effect of dissolved Fe species. Cs-K_d-values reported in Molera and Eriksen (2002) are way higher (200–580 L/kg) but have been derived considering surface diffusion phenomena, so that those values cannot be compared with those in the present study.

A K_d-value derived for Co^{2+} from data obtained in diffusion experiments in magnetite/GMZ is way lower ($K_d = 4.2$) than expected according to sorption modelling and published experimental results obtained for Co^{2+} sorption/diffusion onto/in bentonite (Bradbury and Baeyens (2002a): 400 L/kg for Ni^{2+} and Molera and Eriksen (2002): 2400–2600 L/Kg; Missana et al. (2007): 14.000 L/kg). However, as pointed out earlier, data are not directly comparable (Ni^{2+} has been investigated in one case, a

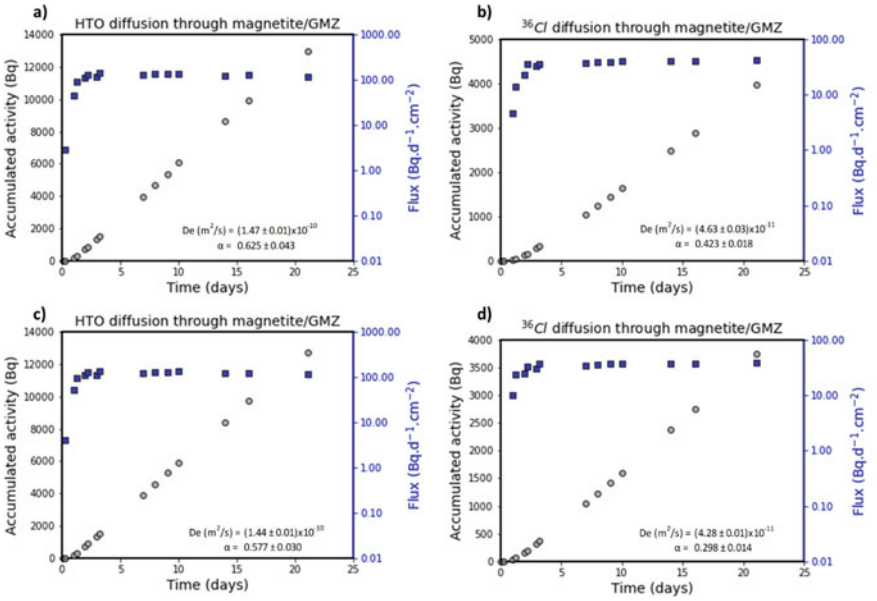

Fig. 3.34 Accumulated activity (in Bq) and flux (in $Bq.d^{-1}{\cdot}cm^{-2}$) in function of diffusion time (in days) for HTO and ^{36}Cl through the magnetite/GMZ bentonite interface, effective diffusion coefficients and rock capacity factors in cell 3 (**a** and **b**)

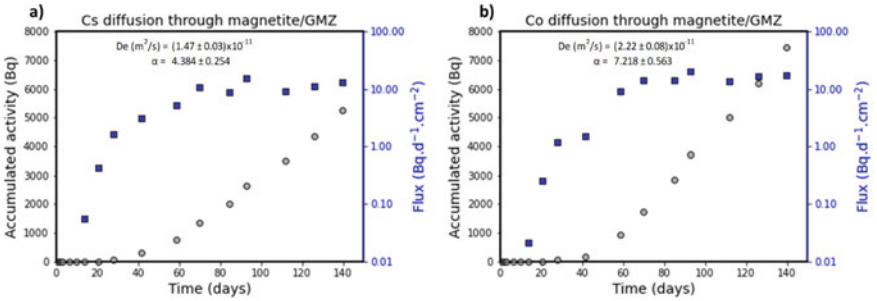

Fig. 3.35 Accumulated activity (in Bq) and flux (in $Bq.d^{-1}{\cdot}cm^{-2}$) in function of diffusion time (in days) for ^{137}Cs and ^{60}Co through the magnetite/GMZ bentonite interface, effective diffusion coefficients and rock capacity factors in cell 3 (**a**) and cell 4 (**b**)

surface diffusion approach has been applied in the other). Nevertheless, the quite low sorption value obtained in the present study may also be a consequence of competitive sorption of Fe species.

Data for Co^{2+} and Cs^{+} sorption onto magnetite have been reported by Ebner et al. (2001) (Cs ~20 L/kg, Co ~90 L/kg) and are also higher than found in our diffusion study. However, they were determined in 0.01 M $NaNO_3$. The higher ionic strength

Table 3.11 Effective diffusion coefficients and rock capacity factors of HTO, ^{36}Cl, ^{137}Cs and ^{60}Co through GMZ bentonite and magnetite/GMZ bentonite interface; note that parameters for the GMZ/magnetite samples are the result of a simplified modelling approach (see text for more details)

		Cell1	Cell2	Cell3	Cell4
		GMZ		GMZ/magnetite	
HTO	De(m^2/S)	$(5.79 \pm 0.06) \times 10^{-11}$	$(5.54 \pm 0.05) \times 10^{-11}$	$(1.47 \pm 0.01) \times 10^{-10}$	$(1.44 \pm 0.01) \times 10^{-10}$
	α	0.536 ± 0.041	0.448 ± 0.035	0.625 ± 0.043	0.577 ± 0.030
^{36}Cl	De(m^2/s)	$(1.37 \pm 0.01) \times 10^{-11}$	$(1.24 \pm 0.01) \times 10^{-11}$	$(4.63 \pm 0.03) \times 10^{-11}$	$(4.28 \pm 0.01) \times 10^{-11}$
	α	0.088 ± 0.006	0.082 ± 0.004	0.423 ± 0.018	0.298 ± 0.014
^{137}Cs	De(m^2/s)			$(1.47 \pm 0.03) \times 10^{-11}$	
	α			4.384 ± 0.254	
^{60}Co	De(m^2/s)				$(2.22 \pm 0.08) \times 10^{-11}$
	α				7.218 ± 0.563

conditions of the present experiments and the potential competition with dissolved Fe species might explain the differences.

References

Bergmann, J., & Kleeberg, R. (1998). Rietveld analysis of disordered layer silicates. *Materials Science Forum, 278–281*(PART 1), 300–305. Cited by: 59.

Birgersson, M., Hedström, M., Karnland, O., & Sjöland, A. (2017). Bentonite buffer: Macroscopic performance from nanoscale properties. In *Geological Repository Systems for Safe Disposal of Spent Nuclear Fuels and Radioactive Waste* (pp. 319–364). Elsevier.

Bouby, M., Kraft, S., Kuschel, S., Geyer, F., Moisei-Rabung, S., Schäfer, T., & Geckeis, H. (2020). Erosion dynamics of compacted raw or homoionic MX80 bentonite in a low ionic strength synthetic water under quasi-stagnant flow conditions. *Applied Clay Science, 198*, 105797.

Bradbury, M. H., & Baeyens, B. (2002a). A comparison of apparent diffusion coefficients measured in compacted kunigel v1 bentonite with those calculated from batch sorption measurements and De (HTO) data: A case study for Cs (i), Ni (ii), Sm (iii), Am (iii), Zr (iv) and Np (v). Technical report, NAGRA Technical Report, NTB 02-17.

Bradbury, M. H., & Baeyens, B. (2002b). Porewater chemistry in compacted re-saturated MX-80 bentonite: Physico-chemical characterisation and geochemical modelling. Technical report, PSI Bericht Nr. 02-10, ISSN 1019-0643.

Brandt, F., & Bosbach, D. (2001). Bassanite (CaSO4. 0.5 H2O) dissolution and gypsum (CaSO4. 2H2O) precipitation in the presence of cellulose ethers. *Journal of Crystal Growth, 233*(4), 837–845.

Bucher, F., & Müller-Vonmoos, M. (1989). Bentonite as a containment barrier for the disposal of highly radioactive wastes. *Applied Clay Science, 4*(2), 157–177.

CASEA. (2013). Datasheet alpha agr 40. *99755 Ellrich, Germany, CASEA GmbH, REMONDIS-Group.*

Chaparro, M. C., Finck, N., Metz, V., & Geckeis, H. (2021). Reactive transport modelling of the long-term interaction between carbon steel and MX-80 bentonite at 25°C. *Minerals, 11*(11), 1272.

Cui, L.-Y., Ye, W.-M., Wang, Q., Chen, Y.-G., Chen, B., & Cui, Y.-J. (2021). Insights into gas migration behavior in saturated GMZ bentonite under flexible constraint conditions. *Construction and Building Materials, 287*, 123070.

Cuss, R., Harrington, J., Noy, D., Graham, C., & Sellin, P. (2014). Evidence of localised gas propagation pathways in a field-scale bentonite engineered barrier system; results from three gas injection tests in the large scale gas injection test (lasgit). *Applied Clay Science, 102*, 81–92.

Dohrmann, R., Genske, D., Karnland, O., Kaufhold, S., Kiviranta, L., Olsson, S., Plötze, M., Sandén, T., Sellin, P., Svensson, D., et al. (2012). Interlaboratory CEC and exchangeable cation study of bentonite buffer materials: I. Cu (ii)-triethylenetetramine method. *Clays and Clay Minerals, 60*(2), 162–175.

Duda, R., Rejl, L., & Slivka, D. (1990). Minerals (in Czech). *Aventinum, Prague, from* https://www.mindat.org/loc-7944.html.

Ebner, A. D., Ritter, J. A., & Navratil, J. D. (2001). Adsorption of cesium, strontium, and cobalt ions on magnetite and a magnetite- silica composite. *Industrial & Engineering Chemistry Research, 40*(7), 1615–1623.

Féron, D., Crusset, D., & Gras, J. M. (2009). Corrosion issues in the French high-level nuclear waste program. *Corrosion, 65*(3), 213–223.

Fredlund, D. G., & Rahardjo, H. (1993). *Soil mechanics for unsaturated soils*. Wiley.

García-García, S., Wold, S., & Jonsson, M. (2007). Kinetic determination of critical coagulation concentrations for sodium-and calcium-montmorillonite colloids in NaCl and CaCl2 aqueous solutions. *Journal of Colloid and Interface Science, 315*(2), 512–519.

Graham, C. C., Harrington, J. F., & Sellin, P. (2016). Gas migration in pre-compacted bentonite under elevated pore-water pressure conditions. *Applied Clay Science, 132*, 353–365.

Gutiérrez-Rodrigo, V., Martín, P. L., & Villar, M. V. (2021). Effect of interfaces on gas breaktrough pressure in compacted bentonite used as engineered barrier for radioactive waste disposal. *Process Safety and Environmental Protection, 149*, 244–257.

Harrington, J. F., Graham, C. C., Cuss, R. J., & Norris, S. (2017). Gas network development in a precompacted bentonite experiment: Evidence of generation and evolution. *Applied Clay Science, 147*, 80–89.

HPF. (2015). *Sikron® quarz - stoffdaten*. Frechen: H.-T. M. E. Q. G.

IAEA. (2013). Characterization of swelling clays as components of the engineered barrier system for geological repositories. *IAEA-TECDOC-1718. Vienna, International Atomic Energy Agency.*

Imbert, C., & Villar, M. (2006). Hydro-mechanical response of a bentonite pellets/powder mixture upon infiltration. *Applied Clay Science, 32*(3-4), 197–209. cited By 123.

Jenni, A., Wersin, P., Mäder, U., Gimmi, T., Thoenen, T., Baeyens, B., Hummel, W., Ferrari, A., Marschall, P., & Leupin, O. (2019). Bentonite backfill performance in a high-level waste repository: A geochemical perspective. Technical report, University of Berne.

Kahr, G., Meier, L., Wolf, D., Starke, R., & Kleeberg, R. (1996). Einfache bestimmungsmethode des kationenaustauschvermögens von tonen mit komplexverbindungen des kupfer (ii)-ions mit triethylentetramin und tetraethylenpentamin. *Berichte der DTTG* (pp. 122–126).

Karnland, O., Nilsson, U., Weber, H., & Wersin, P. (2008). Sealing ability of wyoming bentonite pellets foreseen as buffer material-laboratory results. *Physics and Chemistry of the Earth, Parts A/B/C, 33*, S472–S475.

Kaufhold, S., & Dohrmann, R. (2016). Distinguishing between more and less suitable bentonites for storage of high-level radioactive waste. *Clay Minerals, 51*(2), 289–302.

Kaufhold, S., Dohrmann, R., Ufer, K., & Meyer, F. (2002). Comparison of methods for the quantification of montmorillonite in bentonites. *Applied Clay Science, 22*(3), 145–151. Cited by: 77.

Kaufhold, S., Hein, M., Dohrmann, R., & Ufer, K. (2012). Quantification of the mineralogical composition of clays using ftir spectroscopy. *Vibrational Spectroscopy, 59*, 29–39. Cited by: 69.

Kaufhold, S., Kremleva, A., Krüger, S., Rösch, N., Emmerich, K., & Dohrmann, R. (2017). Crystal-chemical composition of dicoctahedral smectites: An energy-based assessment of empirical relations. *ACS Earth and Space Chemistry, 1*(10), 629–636. Cited by: 6.

Kaufhold, S., Dohrmann, R., & Klinkenberg, M. (2010). Water-uptake capacity of bentonites. *Clays and Clay Minerals, 58*(1), 37–43.

Kaufhold, S., Schippers, A., Marx, A., & Dohrmann, R. (2020). SEM study of the early stages of Fe-bentonite corrosion-the role of naturally present reactive silica. *Corrosion Science, 171*, 108716.

Kiviranta, L., & Kumpulainen, S. (2011). Quality control and characterization of bentonite materials. Technical report, Posiva Oy. Working Report 2011-84.

Levasseur, S., Collin, F., Daniels, K., Dymitrowska, M., Harrington, J., Jacops, E., Kolditz, O., Marschall, P., Norris, S., Sillen, X., Talandier, J., Truche, L., & Wendling, J. (2020). Initial state of the art on gas transport in clayey materials. Technical report, Final version as of 30.11.2020 of deliverable D6.1 of the HORIZON 2020 project EURAD. EC Grant agreement no: 847593.

Liu, H.-H. (2017). *Fluid flow in the subsurface*. Springer.

Liu, Y., Ma, L., Ke, D., Cao, S., Xie, J., Zhao, X., Chen, L., & Zhang, P. (2014). Design and validation of the THMC china-mock-up test on buffer material for HLW disposal. *Journal of Rock Mechanics and Geotechnical Engineering, 6*(2), 119–125.

Lorenz, P., Meier, L., & Kahr, G. (1999). Determination of the cation exchange capacity (CEC) of clay minerals using the complexes of copper (ii) ion with triethylenetetramine and tetraethylenepentamine. *Clays and Clay Minerals, 47*(3), 386–388.

Mehrabi, K., Nowack, B., Dasilva, Arroyo Rojas, Y., & Mitrano, D. M. (2017). Improvements in nanoparticle tracking analysis to measure particle aggregation and mass distribution: A case study on engineered nanomaterial stability in incineration landfill leachates. *Environmental Science & Technology,51*(10), 5611–5621.

Missana, T., Garcı, M., et al. (2007). Adsorption of bivalent ions (Ca (ii), Sr (ii) and Co (ii)) onto FEBEX bentonite. *Physics and Chemistry of the Earth, Parts A/B/C, 32*(8–14), 559–567.

Molera, M., & Eriksen, T. (2002). Diffusion of 22Na+, 85Sr2+, 134Cs+ and 57Co2+ in bentonite clay compacted to different densities: Experiments and modeling. *Radiochimica Acta, 90*(9–11), 753–760.

Müller, H. R., Garitte, B., Vogt, T., Köhler, S., Sakaki, T., Weber, H., Spillmann, T., Hertrich, M., Becker, J. K., Giroud, N., et al. (2018). Implementation of the full-scale emplacement (Fe) experiment at the mont terri rock laboratory. *Mont Terri Rock Laboratory, 20 Years: Two Decades of Research and Experimentation on Claystones for Geological Disposal of Radioactive Waste* (pp. 289–308).

Muurinen, A., Pentilla-Hiltunen, P., Rantanen, J., & Uusheimo, K. (1987). Diffusion of uranium and chloride in compacted Na bentonite. In *Technical Report YJT-87-14*. Nuclear waste Commission of Finnish Power Companies Helsinki, Finland.

Pospiskova, I., Dobrev, D., Kouril, M., Stoulil, J., Novikova, D., Kotnour, P., & Matal, O. (2017). Czech national programme and disposal canister concept. *Corrosion Engineering, Science and Technology, 52*(sup1), 6–10.

Pusch, R., Hökmark, H., & Börgesson, L. (1987). Outline of models of water and gas flow through smectite clay buffers. Technical report, SKB Technical Report 87-10, Stockholm, Sweden.

Pusch, R., Karnland, O., & Hökmark, H. (1990). Gmm-a general microstructural model for qualitative and quantitative studies of smectite clays. Technical report, SKB Technical Report 90-43, Stockholm, Sweden.

Schäfer, T., Geckeis, H., Bouby, M., & Fanghänel, T. (2004). U, Th, Eu and colloid mobility in a granite fracture under near-natural flow conditions. *Radiochimica Acta, 92*(9–11), 731–737.

Schwertmann, U., & Cornell, R. M. (2000). *Iron oxides in the laboratory: Preparation and characterization*. WILEY-VCH, Weinheim, Berlin: Wiley.

Seher, H., Geckeis, H., Fanghänel, T., & Schäfer, T. (2020). Bentonite nanoparticle stability and the effect of fulvic acids: Experiments and modelling. *Colloids and Interfaces, 4*(2), 16.

Seiphoori, A. (2015). *Thermo-hydro-mechanical characterisation and modelling of Wyoming granular bentonite*. Switzerland: Nagra Wettingen.

Sellin, P. (2014). Experiments and modelling on the behaviour of ebs. *FORGE Reprot D,3*, 38.

SKB. (2011). Long-term safety for the final repository for spent nuclear fuel at forsmark. *Main report of the SR-Site project, Volume I, Technical Report, TR-11-01*. AB, Svensk Kärnbränslehantering.

Svensson, D., Dueck, A., Nilsson, U., Olsson, S., Sanden, T., Lydmark, S., Jaegerwall, S., Pedersen, K., & Hansen, S. (2011). Alternative buffer material. status of the ongoing laboratory investigation of reference materials and test package 1. *AB, Svensk Kärnbränslehantering*.

Ufer, K., Roth, G., Kleeberg, R., Stanjek, H., Dohrmann, R., & Bergmann, J. (2004). Description of x-ray powder pattern of turbostratically disordered layer structures with a rietveld compatible approach. *Zeitschrift fur Kristallographie, 219*(9), 519–527. Cited by: 129.

UPC. (2015). *User's guide of CODE_BRIGHT—A 3-d program for thermo-hydro-mechanical analysis in geological media*. Department of Geotechnical Engineering and Geosciences of Technical University of Catalonia (UPC), Barcelona, Spain.

Van Loon, L. R., & Müller, W. (2014). A modified version of the combined in-diffusion/abrasive peeling technique for measuring diffusion of strongly sorbing radionuclides in argillaceous rocks: A test study on the diffusion of caesium in opalinus clay. *Applied Radiation and Isotopes, 90*, 197–202.

Van Loon, L. R., & Soler, J. M. (2004). Diffusion of HTO, 36 Cl-, 125 i-and 22 Na+ in opalinus clay: Effect of confining pressure, sample orientation, sample depth and temperature. Technical report, PSI Bericht Nr. 04-03, February 2004.

Villar, M., Armand, G., Conil, N., de Lesquen, C., Herold, P., Simo, E., Mayor, J., Dizier, A., Li, X., Chen, G., Leupin, O., Niskanen, M., Bailey, M., Thompson, S., Svensson, D., Sellin, P., & Hausmannova, L. (2020). Initial state-of-the-art on thm behaviour of i) buffer clay materials and of ii) host clay materials. Technical report, Deliverable D7.1 HITEC. EURAD Project, Horizon 2020, No. 847593. 214 pp.

Villar, M. V., Gómez-Espina, R., & Lloret, A. (2010). Experimental investigation into temperature effect on hydro-mechanical behaviours of bentonite. *Journal of Rock Mechanics and Geotechnical Engineering, 2*(1), 71–78.

Wu, T., Wang, H., Zheng, Q., Zhao, Y. L., & Van Loon, L. R. (2014). Diffusion behavior of Se (iv) and Re (vii) in GMZ bentonite. *Applied Clay Science, 101*, 136–140.

Xu, L., Ye, W., & Ye, B. (2017). Gas breakthrough in saturated compacted gaomiaozi (GMZ) bentonite under rigid boundary conditions. *Canadian Geotechnical Journal, 54*(8), 1139–1149. cited By 27.

Yong, R. N., Nakano, M., & Pusch, R. (2012). *Environmental soil properties and behaviour*. CRC Press.

Zhang, C.-L., Wang, J., Kaufhold, S., Liu, Y., & Czaikowski, O. (2022). Buffering performance of GMZ and mx80 bentonites for geological disposal of high- level radioactive waste. Technical report, GRS report 702, ISBN 978-3-949088-93-3.

Zhang, C.-L. (2021). Deformation and water/gas flow properties of claystone/bentonite mixtures. *Journal of Rock Mechanics and Geotechnical Engineering, 13*(4), 864–874.

Zhang, F., Ye, W.-M., Wang, Q., Chen, Y.-G., & Chen, B. (2019). An insight into the swelling pressure of gmz01 bentonite with consideration of salt solution effects. *Engineering Geology, 251*, 190–196.

Zhu, H., Fu, H., Yan, P., Li, X., Zhang, L., Wang, X., & Chai, C. (2022). Study on the release of GMZ bentonite colloids by static multiple light scattering technique. *Colloids and Surfaces A: Physicochemical and Engineering Aspects*, 128374.

Zhu, C.-M., Ye, W.-M., Chen, Y.-G., Chen, B., & Cui, Y.-J. (2013). Influence of salt solutions on the swelling pressure and hydraulic conductivity of compacted gmz01 bentonite. *Engineering Geology, 166*, 74–80.

Chapter 4
Model Analysis

Aqeel Afzal Chaudhry, Thomas Nagel, Juan Zhao, Uwe Düsterloh, Jingbo Zhao, Liang Chen, Ju Wang, Yuemiao Liu, Shengfei Cao, Qi Zhang, Haibing Shao, Chaofan Chen, Tao Yuan, Renchao Lu, Cornelius Fischer, and Olaf Kolditz

4.1 THM-Modelling of the Mock-Up Test in OpenGeoSys

Aqeel Afzal Chaudhry, Thomas Nagel

4.1.1 Description of the TRM Model

We employ the ThermoRichardsMechanics (TRM) process, Wang et al. (2010) implemented in OpenGeoSys (OGS), Bilke et al. (2019). The process captures a non-isothermal porous medium with a solid phase, a liquid phase and a gas phase which is considered isobaric (Richards, 1931). Thus, the model is governed by three balance equations i.e., an energy balance, a mass balance of the liquid phase and the linear momentum balance of the mixture which are thus formulated based on three independent state variables i.e., temperature T, liquid pressure p_{LR} and solid

A. A. Chaudhry · T. Nagel
Technische Universität Bergakademie Freiberg, Geotechnical Institute, 09599 Freiberg, Germany

J. Zhao · U. Düsterloh
Clausthal University of Technology, Geomechanics and Multiphysical Systems, Erzstraße 20, 38678 Clausthal-Zellerfeld, Germany

J. Zhao · L. Chen · J. Wang · Y. Liu · S. Cao · Q. Zhang
Beishan Underground Research Laboratory for HLW Disposal, Beijing Research Institute of Uranium Geology, Beijing 100029, China

H. Shao · C. Chen · R. Lu · O. Kolditz (✉)
Helmholtz Centre for Environmental Research UFZ, 04318 Leipzig, Germany
e-mail: olaf.kolditz@ufz.de

T. Yuan · C. Fischer
Helmholtz Centre Dresden-Rossendorf HZDR, 01328 Dresden, Germany

H. Shao et al. (eds.), *Thermo-Hydro-Mechanical-Chemical (THMC) Processes in Bentonite Barrier Systems*, Terrestrial Environmental Sciences,
https://doi.org/10.1007/978-3-031-53204-7_4

displacement $\mathbf{u}_S$, respectively. In addition, the TRM process allows for the inclusion of liquid evaporation and a vapor diffusion model based on Philip and De Vries (1957a) is implemented. For the sake of brevity, we will not mention all the terms appearing in the equations in this section but focus on terms that are not standard in similar implementations or of particular importance for interpreting the results. For a detailed description of the TRM model summarized here as well as it's comparison to a non-isothermal two-phase two-component flow with mechanics model (TH^2M), published by Grunwald et al. (2022), the reader is referred to Pitz et al. (2022).

The heat balance equation is written as

$$\begin{aligned}&(\rho c_p)_{\text{eff}} \frac{\mathrm{d}T}{\mathrm{d}t} + L_0 \frac{\mathrm{d}\theta_{\text{vap}}}{\mathrm{d}t} - \operatorname{div}\left(\boldsymbol{\lambda}_{\text{eff}} \operatorname{grad} T\right) \\ &+ \operatorname{div}\left(\frac{L_0 \boldsymbol{J}_{\text{G}}^{\text{W}}}{\rho_{\text{GR}}^{\text{W}}}\right) + \operatorname{grad} T \cdot \left(c_{p\text{L}} \boldsymbol{A}_{\text{L}} + c_{p,\text{vap}}\, \boldsymbol{J}_{\text{G}}^{\text{W}}\right) = Q_T\end{aligned} \tag{4.1}$$

where $(\rho c_p)_{\text{eff}}$ is the effective volumetric heat capacity of the medium and can be obtained using the respective phase properties as

$$(\rho c_p)_{\text{eff}} = \phi S_{\text{L}} \rho_{\text{LR}} c_{p\text{L}} + (1-\phi)\rho_{\text{SR}} c_{p\text{S}} \tag{4.2}$$

At this stage, to avoid confusion, it is appropriate to point out that S_{L} represents the liquid saturation while "S" in the subscript indicates the corresponding property of the solid phase. The effective thermal conductivity $\boldsymbol{\lambda}_{\text{eff}}$ in Eq. 4.1 is considered to be saturation-dependent for bentonite in our case and can be written as a function of dry ($\boldsymbol{\lambda}_{\text{dry}}$) and wet / saturated ($\boldsymbol{\lambda}_{\text{wet}}$) thermal conductivity as

$$\boldsymbol{\lambda}_{\text{eff}} = \boldsymbol{\lambda}_{\text{dry}} + S_{\text{L}} \left(\boldsymbol{\lambda}_{\text{wet}} - \boldsymbol{\lambda}_{\text{dry}}\right) \tag{4.3}$$

Furthermore, L_0 in Eq. 4.1 is the volumetric latent heat of vaporization and can be written for water following (Saito et al., 2006) as

$$L_0 = \rho_{\text{LR}} \left(2.501 \cdot 10^6\ \text{J kg}^{-1} - 2369.2\ \text{J kg}^{-1}\,(T - 273.15\,\text{K})\right) \tag{4.4}$$

θ_{vap} in Eq. 4.1 is the water vapor content and is given following (De Vries, 1958; Saito et al., 2006) as

$$\theta_{\text{vap}} = \phi(1 - S_{\text{L}}) \frac{\rho_{\text{GR}}^{\text{W}}}{\rho_{\text{LR}}} \tag{4.5}$$

where the vapor density $\rho_{\text{GR}}^{\text{W}}$ can be deduced from Kelvin-Laplace equation as

$$\rho_{\text{GR}}^{\text{W}} = \rho_{\text{vap}}^{\text{W}} \exp\left(-\frac{p_{\text{cap}}}{\rho_{\text{LR}} R T}\right) \tag{4.6}$$

where p_{cap} is the capillary pressure, R is specific gas constant for water vapor and $\rho_{\mathrm{vap}}^{\mathrm{W}}$ is the saturated vapor density given as, (Harrison, 1965)

$$\rho_{\mathrm{vap}}^{\mathrm{W}} = 10^{-3}\,\mathrm{kg\,m^{-3}}\,\exp\left(19.819 - \frac{4975.9\,\mathrm{K}}{T}\right) \tag{4.7}$$

The fourth term on the left hand side of Eq. 4.1 represents the transport of latent heat while the last term represents the sensible heat transported by water and vapor per unit area. The term on the right hand side of Eq. 4.1 represents the heat source (or sink).

The mass balance equation for the liquid phase is given as

$$\begin{aligned}
&\rho_{\mathrm{LR}} S_{\mathrm{L}}(\alpha_{\mathrm{B}} - \phi)\beta_{p,\mathrm{SR}} \frac{\mathrm{d}p_{\mathrm{LR}}}{\mathrm{d}t} - \rho_{\mathrm{LR}} S_{\mathrm{L}}(\alpha_{\mathrm{B}} - \phi)\,\mathrm{tr}(\boldsymbol{\alpha}_{T,\mathrm{SR}})\frac{\mathrm{d}T}{\mathrm{d}t} \\
&+ \phi\left((1 - S_{\mathrm{L}})\frac{\mathrm{d}\rho_{\mathrm{GR}}^{\mathrm{W}}}{\mathrm{d}t} + S_{\mathrm{L}}\frac{\mathrm{d}\rho_{\mathrm{LR}}}{\mathrm{d}t}\right) + (\rho_{\mathrm{LR}} - \rho_{\mathrm{GR}}^{\mathrm{W}})\left[\phi + p_{\mathrm{LR}} S_{\mathrm{L}}(\alpha_{\mathrm{B}} - \phi)\right]\frac{\mathrm{d}S_{\mathrm{L}}}{\mathrm{d}t} \\
&+ \rho_{\mathrm{LR}} S_{\mathrm{L}}\alpha_{\mathrm{B}}\mathrm{div}\left(\frac{\mathrm{d}\boldsymbol{u}_{\mathrm{S}}}{\mathrm{d}t}\right) + \mathrm{div}\left(\boldsymbol{A}_{\mathrm{L}}^{\mathrm{W}} + \boldsymbol{J}_{\mathrm{G}}^{\mathrm{W}}\right) = Q_H
\end{aligned} \tag{4.8}$$

where α_{B}, $\beta_{p,\mathrm{SR}}$ and $\boldsymbol{\alpha}_{T,\mathrm{SR}}$ represent the Biot-Willis coefficient, intrinsic solid compressibility and the solid's linear thermal expansion tensor, respectively, whereas Q_H on the right hand side represents the fluid source (or sink).

The linear momentum balance of the overall mixture is given as

$$\mathrm{div}\left(\boldsymbol{\sigma}^{\mathrm{eff}} - \alpha_{\mathrm{B}}\chi(S_{\mathrm{L}})p_{\mathrm{LR}}\,\mathbf{I}\right) + \rho\mathbf{g} = \mathbf{0} \tag{4.9}$$

with

$$\dot{\boldsymbol{\sigma}}^{\mathrm{eff}} = \boldsymbol{\mathcal{C}} : (\dot{\boldsymbol{\epsilon}} - \dot{\boldsymbol{\epsilon}}_{\mathrm{pl}} - \dot{\boldsymbol{\epsilon}}_{\mathrm{th}} - \dot{\boldsymbol{\epsilon}}_{\mathrm{sw}}) \tag{4.10}$$

where $\boldsymbol{\mathcal{C}}$ is the fourth order elastic stiffness tensor while $\boldsymbol{\epsilon}$, $\boldsymbol{\epsilon}_{\mathrm{pl}}$, $\boldsymbol{\epsilon}_{\mathrm{th}}$ and $\boldsymbol{\epsilon}_{\mathrm{sw}}$ represent the total, plastic, thermal and swelling strains, respectively. Furthermore, $\chi(S_{\mathrm{L}})$ in Eq. 4.9 is the Bishop coefficient. The implementation in OGS-6 allows different possibilities to account for Richard coefficient, e.g., `BishopsPowerLaw` and `BishopsSaturationCutoff` which can be written respectively as

$$\chi(S_{\mathrm{L}}) = {S_{\mathrm{L}}}^{n}, \qquad \chi(S_{\mathrm{L}}) = \begin{cases} 1 & \text{for } S_{\mathrm{L}} \geq S_{\mathrm{cutoff}} \\ 0 & \text{for } S_{\mathrm{L}} < S_{\mathrm{cutoff}}\,, \end{cases} \tag{4.11}$$

where the exponent n and S_{cutoff} are the controlling parameters in each case. The swelling strain rate in Eq. 4.10 is given as

$$\dot{\boldsymbol{\epsilon}}_{\mathrm{sw}} = -\boldsymbol{\mathcal{C}}^{-1} : \dot{\boldsymbol{\sigma}}_{\mathrm{sw}} \tag{4.12}$$

Table 4.1 List of parameters to be specified for the anisotropic swelling model

Name	Symbol	Unit
Local coordinate system	$\mathbf{n}_i$	–
Maximum swelling pressures (principal directions)	$\hat{p}_{\mathrm{sw},i}$	Pa
Swelling exponents (principal directions)	$\lambda_{\mathrm{sw},i}$	–
Upper saturation limit for swelling law	$S_{\mathrm{max,sw}}$	–
Lower saturation limit for swelling law	$S_{\mathrm{min,sw}}$	–

where the anisotropic swelling stress is implemented as

$$\boldsymbol{\sigma}_{\mathrm{sw}} = -\sum_{i=1}^{3} \hat{p}_{\mathrm{sw},i} \left(S_{\mathrm{eff,sw}}^{\lambda_{\mathrm{sw},i}} - S_{\mathrm{eff,sw}\,0}^{\lambda_{\mathrm{sw},i}} \right) \mathbf{n}_i \otimes \mathbf{n}_i \tag{4.13}$$

where $\hat{p}_i$ is the maximum swelling pressure in direction $\mathbf{n}_i$. Furthermore,

$$S_{\mathrm{eff,sw}} = \frac{S_{\mathrm{L}} - S_{\mathrm{min,sw}}}{S_{\mathrm{max,sw}} - S_{\mathrm{min,sw}}} \quad \text{and} \quad S_{\mathrm{eff,sw}} \in [0, 1] \tag{4.14}$$

Instead of using Eq. 4.13 directly, the model is implemented in the rate form as

$$\dot{\boldsymbol{\sigma}}_{\mathrm{sw}} = -\sum_{i=1}^{3} \lambda_{\mathrm{sw},i}\, \hat{p}_{\mathrm{sw},i}\, S_{\mathrm{eff,sw}}^{\lambda_{\mathrm{sw},i}-1}\, \mathbf{n}_i \otimes \mathbf{n}_i\, \dot{S}_{\mathrm{eff,sw}} \tag{4.15}$$

The parameters required for this anisotropic swelling law implementation in OGS-6 are summarized in Table 4.1. For this study, we limited ourselves to the use of isotropic swelling model only.

Porosity evolution is dictated by the solid mass balance and drives a power-law permeability evolution:

$$\mathbf{k} = \sum_{i=1}^{3} k_{0,i} \left(\frac{\phi}{\phi_0} \right)^{\lambda^{k,i}} \mathbf{n}_i \otimes \mathbf{n}_i \tag{4.16}$$

4.1.2 Model Setup and Partial Assembly

The waste repository concept which is the design basis of the China mock-up experiment as well as the sketch showing the components of the lab experiment are depicted in Figs. 4 and 5 in Wang (2010b), respectively. The main components are a heating strip and heater body in the center, a temperature control system, highly-compacted GMZ bentonite blocks, crushed bentonite, a steel tank enclosing the bentonite blocks,

an insulation layer, a fluid injection system, sensors to measure temperature, stresses and relative humidity, gas collection and measurement system as well as a data acquisition system (Wang, 2010b). As from the numerical simulation perspective, not all of these components can or need to be modeled using the fully coupled THM process. It is common practice to either exclude many of these components like the heater body, steel tank or insulation layer from the numerical model or the thermal, hydraulic and mechanical processes are "switched off" by modifying material properties such as permeability or porosity, which is not without numerical or conceptual issues. To circumvent this problem, a new feature called partial domain deactivation was implemented in OGS-6 which, as the name indicates, allows to disable or exclude a subset of physical processes for selected sub-domains by making use of partial assembly of the finite element matrices. This features brings along several advantages: at the pre-processing stage, all the components can be included while creating the geometry or mesh without any concern to go through this whole process again if some component needs to be excluded at some later stage. Furthermore, this feature allows to reduce computational cost tremendously by reducing the number of degrees of freedom as the governing equation for the process to be deactivated is not solved for that particular sub-domain. The reduced computational cost becomes quite significant when the disabled process is related to a vector field like solid displacement. Defining the boundary conditions is also simplified as for example, if the hydraulic process is disabled for the outer most layer in a mesh, there is no need to define physically redundant boundary conditions on the outer boundary for fluid flow in such a case. Furthermore, there is no need to define artificial material parameters like a very small value of porosity or permeability for steel for example, which further helps to eliminate convergence problems or numerical instabilities caused by sharp material parameter jumps on the interfaces between adjoining domains. Overall, the physical description becomes more plausible and is closer to the actual problem while at the same time improving numerical behavior.

Figure 4.1 shows the sketch of the geometry used for this work (left) and the corresponding mesh (right). The hydraulic process is deactivated using the newly implemented sub-domain deactivation feature in OGS-6 for the domains representing the heater body, steel tank and insulation layer, in which no distinct fluid phase needs to be modeled. This is also shown by labeling the corresponding domains in Fig. 4.1a using TM which stands for Thermal-Mechanical process. The material properties used for bentonite are mostly taken from BRIUG (2013, 2014), those for the steel tank and insulation layer from Table 1 in Liu et al. (2014). For the heater body, we used the same properties as steel, except a higher value of the thermal conductivity ($80\,\mathrm{W\,m^{-1}\,K^{-1}}$). A higher value of permeability is used for the crushed bentonite layer, as well as a lowered water retention potential as compared to the bentonite blocks. We will come back to this later in the upcoming section. The initial condition for temperature is $T_0 = 20\,^{\circ}\mathrm{C}$ and the fluid pressure is initially set to $p_{\mathrm{LR},0} = -80\,\mathrm{MPa}$ which corresponds to an initial saturation of $S_{\mathrm{L}} = 0.5346$, while the initial horizontal and vertical displacements are kept at zero. As a result of malfunctioning of the lower part of heating strip in the experiment, the heating is imposed via the upper left half of the heater boundary only as shown in Fig. 4.1a,

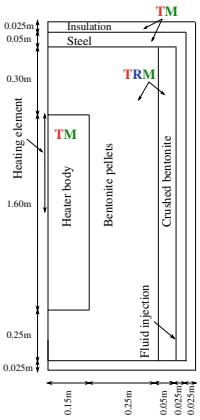

(a) Geometry consisting of multiple subdomains

(b) Triangular mesh used for the China Mock-up experiment

Fig. 4.1 Setup for the numerical experiment

where the temperature is raised from 20 °C to 30 °C in 100 d, from 30 °C to 90 °C in 60 d and then kept constant. In the actual lab experiment, the room temperature varied significantly throughout the entire duration of the experiment. We, thus, used the temperature recorded as the room temperature boundary condition on the outer boundaries. The fluid injection is done in two stages; in the first stage, the fluid is injected by using a Neumann boundary condition for the first 500 d through the lower part of the interface between the steel and crushed bentonite layer as shown in Fig. 4.1a and in the second stage by keeping the fluid pressure constant at 0.2 MPa on the whole vertical interface between the steel tank and the crushed bentonite layer. Furthermore, the horizontal displacements are fixed on the left boundary (axial symmetry) while the vertical displacement is fixed on the bottom edge.

4.1.3 Selected Results

Before proceeding further, it is important to mention that there are several sources of uncertainties related to the experiment, and we proceed with the discussion of the results in two stages. In the first stage, we briefly discuss selected results obtained using the material parameters and boundary conditions provided in the previous section, while in the second stage, we discuss the related uncertainties in more detail and how they affect the results, as well as, give our perspective for further research in this regard.

Figure 4.2 shows the distribution of temperature during the earlier heating stage i.e., the time to reach the peak temperature. The effect of heating through the upper

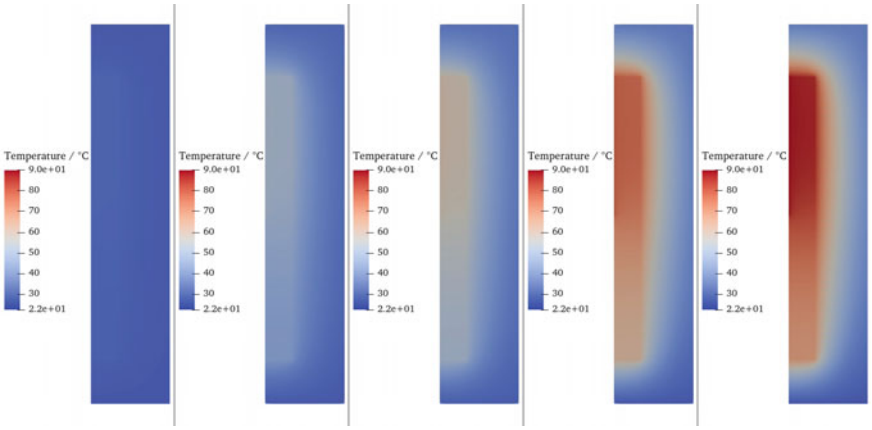

Fig. 4.2 Temperature profiles at times $t = [100, 115, 130, 145, 160]$ days (left to right). Only the domains representing the heater, bentonite pellets and crushed bentonite are shown here

part of the heater only, is clearly visible here and can also be seen in BRIUG (2014), even when a high value of thermal conductivity is used for the heater body. Therefore, it can be inferred that it is better to include the heater body in the numerical model, instead of applying the heat source as a boundary condition to the bentonite blocks directly. The latter would create an assymmetry in the temperature field that would be too strong compared to the measurements. In other words, heat conduction to the lower part of the heater is a significant effect for capturing heat transfer into the bentonite. We do not show any comparison of the distribution results with BRIUG (2014) as firstly, this type of plot merely gives a qualitative picture of the results and secondly, the considerable fluctuation in the room temperature makes it even harder to serve the purpose of a quantitative comparison. Figure 4.3 shows the saturation distribution in the domains representing the bentonite blocks and the crushed bentonite section at different times. As the fluid injection during the first stage is done through the lower part of the crushed bentonite section, the bottom right part shows higher saturation (gravity effects are also included). The saturation front moves faster in the crushed bentonite layer due to higher permeability as compared to the bentonite blocks. As the fluid pressure is raised to 0.2 MPa after 500 d, the crushed bentonite section gets fully saturated soon after and the saturation front moves to the left. But even after 1000 d, the bentonite blocks do not get fully saturated in the upper left region which can partly be attributed to the saturation starting from the bottom right as well as the drying effect of the heater in the upper left region.

Figure 4.4 shows the evolution of temperature with time at two different points which are at the same horizontal distance from the heat source but at different heights. For all the plots showing temperature evolution, we also show the heater temperature (dashed red line) and room temperature (dashed green line) to have a clear view of the effect of these boundary conditions. The OGS-6 results at the point in the top area match very well with the experimental results, especially during the later times, while

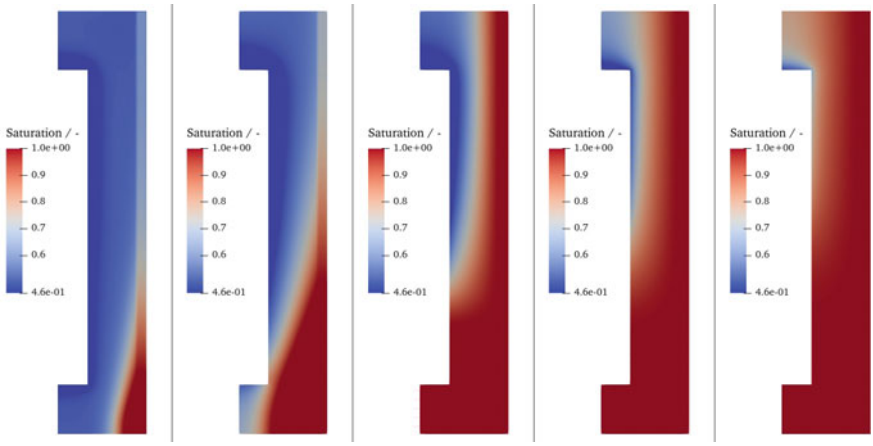

Fig. 4.3 Saturation profiles at times $t = [200, 400, 600, 800, 1000]$ days (left to right). Only the domains representing the bentonite pellets and crushed bentonite are shown here

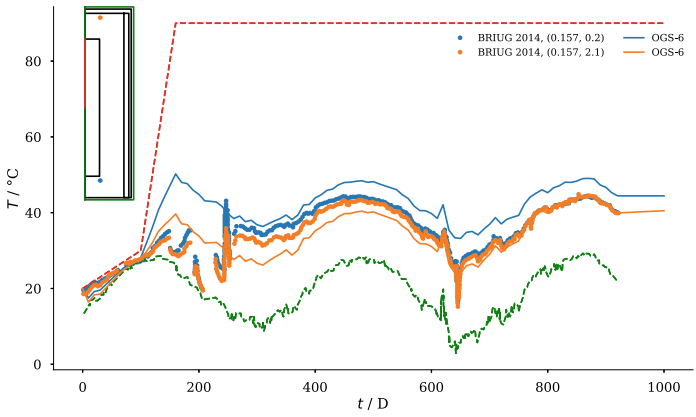

Fig. 4.4 Temperature evolution in time at points in the area near the heater. Dashed red and green lines show the heater and room temperature boundary condition, respectively. "BRIUG 2014" in figure legend refers to the experimental data

we see that OGS-6 shows higher temperatures for the point near the bottom side. Furthermore, it is to be noted that the influence of room temperature is relatively more dominant than the heater. The different temperature spreads between simulation and experiment show that the experiment is even more dominated by the lab temperature. Figure 4.5 shows the temperature evolution at points which are at a somewhat similar horizontal distance from the heater as well as outer boundary. It can be observed here again that the OGS-6 results in the upper region are in good agreement with the experimental results as compared to the lower region. But, in contrast to Fig. 4.4, the current parameterization gives relatively lower temperatures than the experimental

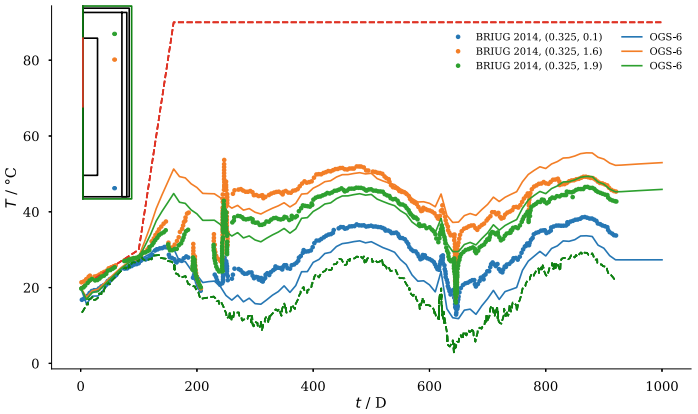

Fig. 4.5 Temperature evolution in time at points in the middle region between the heater and the outer boundary. Dashed red and green lines show the heater and room temperature boundary condition, respectively

results. Figure 4.6 shows the temperature evolution in the crushed bentonite region which is not only relatively nearer to the room temperature boundary but also is the area where the fluid injection takes place. The trend observed earlier can also be seen here as the OGS-6 results are able to reproduce the experimental results at the upper point very well, especially in the later stage which is also the time at which the fluid pressure is raised to 0.2 MPa. At the position in the lower area inside the crushed bentonite region, the model again gives slightly high temperatures.

Figure 4.7 shows the comparison of RH (relative humidity) evolution results between OGS-6 and the experimental data in the bottom region at three different points. At the point near the fluid injection boundary (green), the chosen settings for the numerical test, result in a good match with the experimental data while in the area away from the fluid source (orange and blue), the differences are relatively more pronounced but still the overall trend is captured well by the numerical test. In Fig. 4.8, which shows the RH evolution at two points in the central region ($y = 1.1$ m), the effect of desaturation by drying effect caused by the heater and the subsequent resaturation caused by the fluid injection can be observed near the heater boundary. This drying effect is not observed in the numerical results near the fluid injection boundary which is plausible given the temperature evolution. In the upper region as shown in Fig. 4.9, the numerical results are again in a better agreement with the experimental results, and show that the bentonite structure is still not fully saturated in the area near the heater.

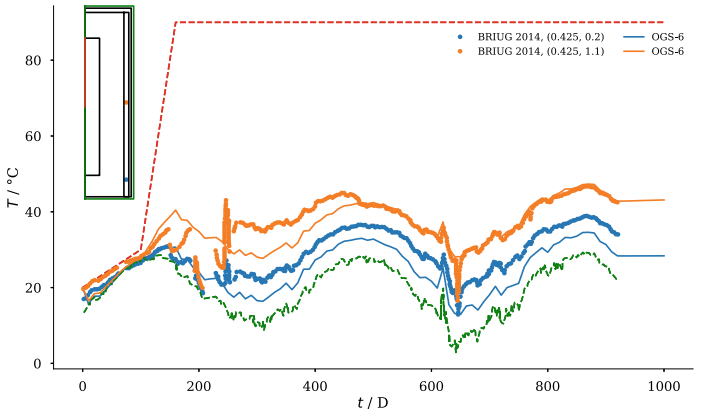

Fig. 4.6 Temperature evolution in time at points in the area near the outer boundary (crushed bentonite area). Dashed red and green lines show the heater and room temperature boundary condition, respectively

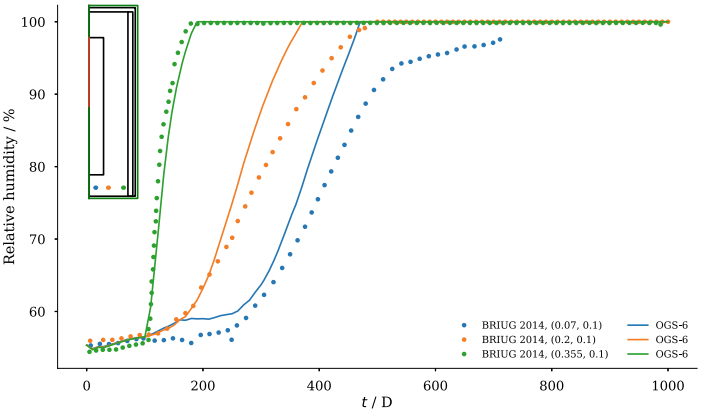

Fig. 4.7 Evolution of relative humidity in time in the lower region. Solid lines show the OGS-6 results while the experimental results are plotted using dots

4.1.4 Discussion in View of Uncertainties and Outlook

In previous work for the China-Mock-Up experiment, numerical simulations were performed in two stages: a thermal process is simulated and solely used to compare the temperature results with the experimental data while a thermal-hydraulic process is used to compare results for relative humidity only. Such a separation may not be appropriate due to the highly complex nature of the coupled THM problem at hand. The drying effect caused by the heater, for example, results in a change in the saturation which in turn changes the thermal conductivity, thus influencing the

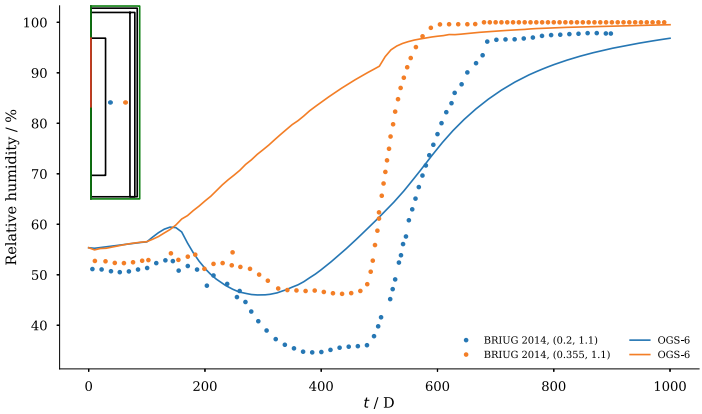

Fig. 4.8 Evolution of relative humidity in time in the middle region. Solid lines show the OGS-6 results while the experimental results are plotted using dots

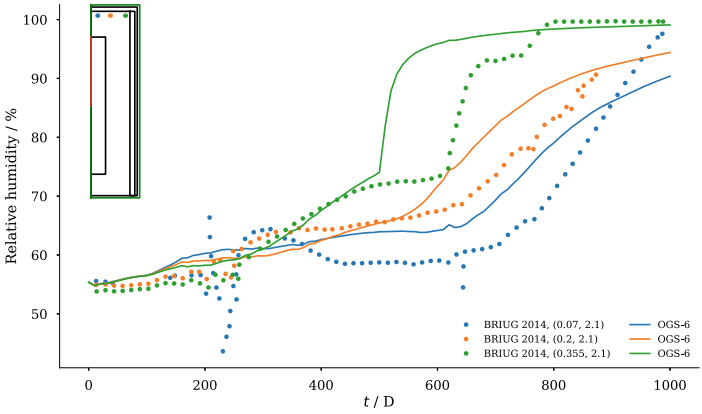

Fig. 4.9 Evolution of relative humidity in time in the upper region. Solid lines show the OGS-6 results while the experimental results are plotted using dots

temperature evolution and in turn the evolution of relative humidity following from both the temperature as well as fluid pressure. Thus, to analyze the results properly, both temperature and RH evolution must be calculated from a coupled model. As a consequence, the choice of material parameters as well as boundary conditions relevant to the fluid phase will strongly affect the temperature evolution. Similarly, the choice of material parameters which may only seem to affect the temperature evolution at first glance, like thermal conductivity, will also affect the RH evolution. To compare the RH results, only two observation points are usually discussed in the literature, namely the point shown with blue color in Fig. 4.8 and the point shown with green color in Fig. 4.9. Moreover, the data is plotted only for times less than 500 d (cf. also Fig. 4.18). We performed several numerical tests with different sets

of material parameters as well as different fluid injection boundary conditions and were able to reproduce the results for these two mentioned points for most of the tests during this early time period. As seen from our results, this early time period ends prior to the arrival of the saturation front, i.e., the phase during which most changes and non-linearities occur. It must thus be considered insufficient for a model validation. Based on available data, significant uncertainty about the sensor locations remains, especially when it comes to their radial/horizontal position, and makes an exact comparison difficult. In Figs. 10–16 showing the experimental results for RH in BRIUG (2014), the horizontal position of the sensors is not specified. The comparison of RH data shown in our work is based on the experimental data obtained from BRIUG (2014) and the visual guess of the sensor locations shown in Chen et al. (2014). This additional data for RH evolution helped us to further confirm that it is important to use different material parameters affecting fluid flow for the crushed bentonite and the bentonite blocks, especially for the intrinsic permeability which appeared to have a strong influence on the results. We will come back to the observations made regarding the significance of intrinsic permeability later. Based on this comparison of the RH results at more locations and over the entire duration of the experiment (which has not been published earlier to the best of our knowledge), we believe that future works should focus on material parameters relevant especially to the water transport process (both in the liquid and the gas phase) as well as the fluid flow boundary condition.

In our previous study (Chaudhry et al., 2021) on the sensitivity analysis of a coupled THM problem, we observed that temperature and fluid pressure are strongly sensitive to the choice of thermal conductivity and intrinsic permeability which is confirmed also for the present case. The thermal conductivity of the heater body, steel tank and insulation layer seem to strongly affect the temperature evolution and thus more information is needed about the actual materials used in the experiment. The only work to the best of our knowledge which accounts for the insulation layer in the numerical model is (Liu et al., 2014) where the thermal conductivity of the insulation is chosen as $0.04\,\mathrm{W\,m^{-1}\,K^{-1}}$. Thermal conductivities for insulation materials can reach up to $0.1\,\mathrm{W\,m^{-1}\,K^{-1}}$ and we observed that the temperature evolution is influenced by even a small change within this range. Intrinsic permeability on the other hand, showed a very strong influence on the evolution of RH. For example, the drying effect observed near the heater shown in Fig. 4.8 in blue color, becomes very pronounced if the intrinsic permeability of the bentonite pellets is reduced even slightly from $7 \cdot 10^{-21}\,\mathrm{m^2}$ to $5 \cdot 10^{-21}\,\mathrm{m^2}$. Furthermore, the choice of intrinsic permeability of the crushed bentonite layer appears to strongly dictate the horizontal and vertical direction of the movement of the saturation front. Thus, although an exact estimate of the value of intrinsic permeability of crushed bentonite may be difficult from experimental perspective but an informed expert guess can help the numerical implementation significantly. This is not a trivial issue because porosity and permeability exists at different scales: there are inter-block gaps acting as potential path ways and one may distinguish macro- and micro porosity in the blocks themselves. The present results indicate that it may be worth extending the model

description accordingly, provided meaningful information on material and structural characterization can be obtained.

When it comes to the intrinsic permeability of expansive porous media, not only is the reduction of uncertainties in the material parameters significant but also the choice and complexity of the numerical model in terms of secondary coupling. It is a well-known fact that the intrinsic permeability of swelling porous media can be influenced by changes in both the effective transport porosity which is the proportion of the pore space available for fluid flow and the micro porosity related to the swelling potential. The relationship between the intrinsic permeability and these porosity measures is non-linear and transient with an additional time scale. Considering the high sensitivity to intrinsic permeability mentioned earlier, the coupling of swelling to porosity to permeability is expected to contribute to the complex patterns observed in the China-Mock-Up test, in which the drying front and saturation front approach each other from opposite directions causing subsequent shrinkage and swelling of these regions locally with a simultaneous long-range interaction imparted by the mechanical process (e.g., compression of regions adjacent to a swelling region). As the TRM process in OGS-6 allows to account for dual porosity media, the dependence of intrinsic permeability on the transport porosity, and takes into account the mechanical coupling we plan to further investigate the China-Mock-Up test by considering such extended formulations.

Currently, three-dimensional simulations are employed to study the effect of different representations of the fluid boundary conditions in combination with heterogeneity in the bentonite fill. While current analyses were based on data published previously on the China Mock-Up experiment, more data has been acquired as part of this project. This data addresses some of the points discussed above in the context of uncertainty. In particular, information on micro and macroporosity as well as HM-coupled tests and data on the swelling behavior are available Sect. 3.1. Incorporating this data into the simulations outlined above and alleviating open issues related to the thermal and hydraulic boundary conditions is expected to further improve the results.

4.2 THM–Modelling of Mock-Up Test in FLAC3D-TOUGH2

Juan Zhao, Düsterloh Uwe

4.2.1 FLAC3D-TOUGH2-Simulator

The TUC-chair for Geomechanics and Multiphysics Systems used their self-developed FLAC3D-TOUGH2-simulator (FTK-simulator) for numerical simulations in this research project. The FTK-simulator is based on the

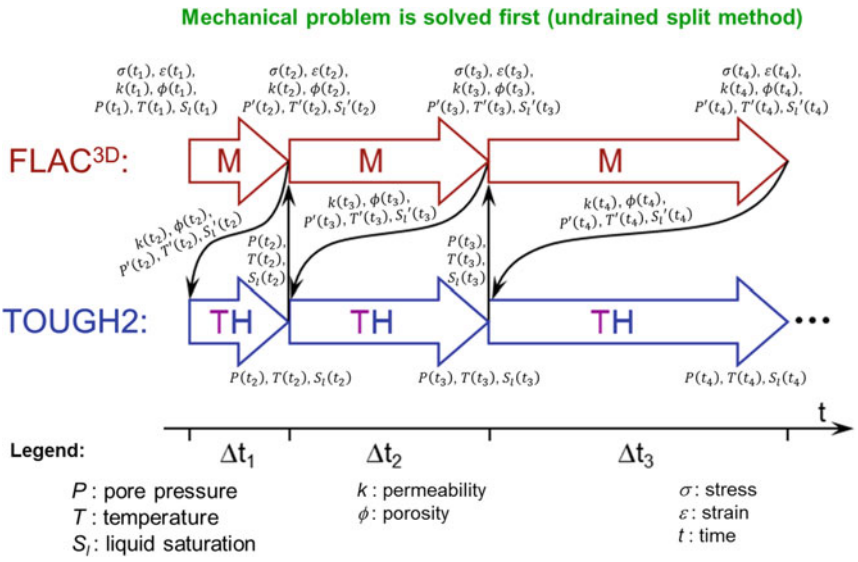

Fig. 4.10 FLAC3D-TOUGH2-coupled simulation processes

TOUGH-FLAC-simulator from Lawrence Berkeley National Laboratory (LBNL) and has been updated with the ability to handle finite strains and time-dependent rheology, specifically for the study of underground disposal of nuclear waste in various host rock formations, such as rock salt, claystone, and crystalline.

The FTK-simulator is a numerical tool that sequentially combines the TOUGH2-simulator and the FLAC3D-simulator according to the undrained split method. At the FTK-simulator, the TOUGH2 component handles the non-isothermal, multicomponent and multiphase flow sub-problem, while the FLAC3D-component handles the geomechanics sub-problem. The detailed process of this coupling method is shown in Fig. 4.10. In this method, the geomechanics sub-problem is solved first, assuming fluid mass and temperature remain constant. Pore pressure changes due to volumetric deformation are computed and the pore pressure induced by mechanical deformation is transferred to TOUGH2 during each FLAC3D-TOUGH2-communication step. Changes in porosity and permeability and geometry (large strain mode) are also transferred in these steps. TOUGH2 then solves the flow sub-problem, computes new pore pressures and variables to reach thermodynamic equilibrium (temperature, saturations). These new variables are transferred back to FLAC3D in each TOUGH2-FLAC3D-communication step to compute the new state of mechanical equilibrium. This process is repeated sequentially (Blanco-Martín et al., 2016).

4.2.2 Validation of the Implementation of the Barcelona Basic Model (BBM) into the FTK-Simulator Via Retrospective Analysis of a Bentonite Cube Test from DECOVALEX Project

The Barcelona Basic Model is a constitutive model for simulating the swelling behavior of bentonite when exposed to water. This process can significantly impact the long-term performance of a repository in crystalline/claystone rock, making this constitutive model crucial for accurate simulations. It has been implemented into the FTK-simulator at the TUC-chair for Geomechanics and multiphysics Systems. The implemented model code was first validated by performing retrospective analyses of simulation results from a swelling pressure test on a cube-shaped bentonite test specimen (shown in Fig. 4.11). This test was part of the FEBEX-experiment (Full-scale Engineered Barriers Experiment in Crystalline Host Rock) and has been studied as part of the DECOVALEX-project (Rutqvist et al., 2011; Alonso et al., 2005b).

The numerical simulation of the swelling behavior of a bentonite cube with an edge length of 20 mm, which has been clamped on all sides, during a 10-day gradual saturation process using the TOUGH-FLAC-simulator developed at Lawrence Berkeley National Laboratory (LBNL) is described in Rutqvist et al. (2011). The cube is assumed to have hydraulically tight side and top surfaces, corresponding to a bentonite cube installed in a cube-shaped steel tank with a permeable bottom surface, standing in a water reservoir. Note that wall friction effects are not considered in the simulation.

As described in Rutqvist et al. (2011), the water pressure in the reservoir is slightly above atmospheric pressure, at about $p = 0.52$ MPa. The initial pore gas pressure in the partially saturated bentonite cube is assumed to be the same as atmospheric pressure. The bentonite cubes initial water saturation is $S_l = 0.65$, which leads to a negative pore water pressure caused by the capillary pressure according to the initial partial saturation in the pore space of the bentonite. This creates an additional hydraulic gradient between the water reservoir and the pore space in the bentonite cube, which accelerates the upward Darcy-flow of water and the gradual rise of water within the bentonite cube.

Figure 4.12 illustrates the distribution of water saturation in the bentonite cube at time $t = 4$d, obtained using the TOUGH-FLAC-simulator (left) and the FTK-simulator (right). Both simulations show that the lower region of the cube is fully saturated at time $t = 4$d, while the upper region has a saturation of $S_l \approx 0.85$–0.9.

Figure 4.13(left) shows the simulation results of the time-dependent development of water saturation and gas pressure in the center and upper part of the bentonite cube, obtained using the TOUGH-FLAC-simulator as documented in Rutqvist et al. (2011) and the FTK-simulator. Figure 4.13 (right) shows the simulation results of the time-dependent development of swelling pressure in the upper part of the bentonite cube, obtained using the TOUGH-FLAC-simulator as documented in Rutqvist et al. (2011) and the FTK-simulator. It should be noted that, in addition to the Barcelona Basic Model for modeling THM-coupled processes in the bentonite, for compar-

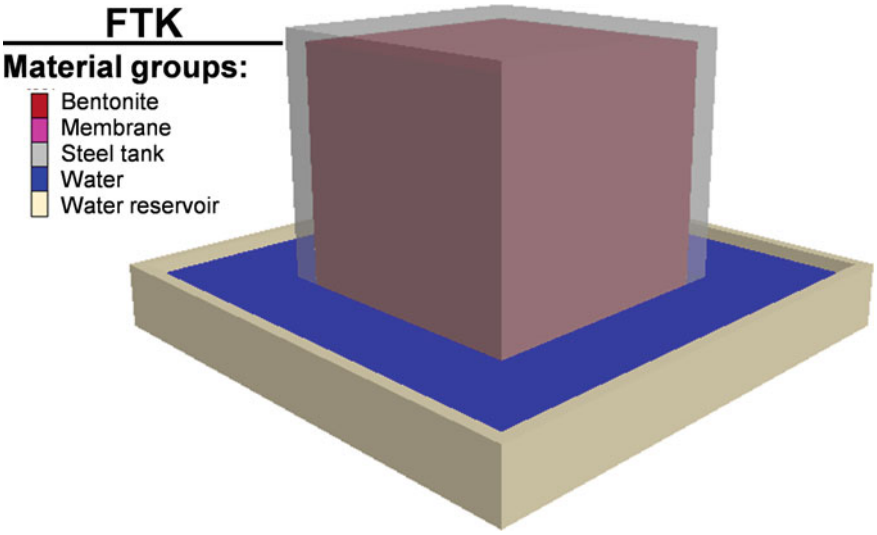

Fig. 4.11 Bentonite cube in water reservoir–FEBEX-experiment (Full-scale Engineered Barriers in Crystalline Host Rock)–DECOVALEX-project

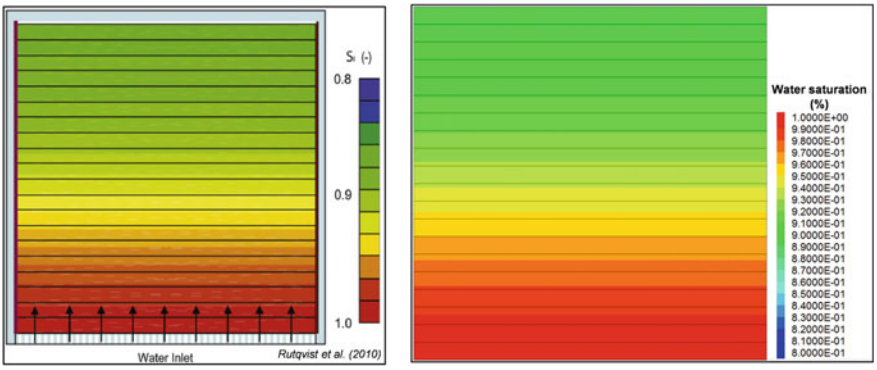

Fig. 4.12 Water saturation in bentonite cube–simulation results at t = 4d –TOUGH-FLAC-simulator (left) as presented in Rutqvist et al. (2011) and FTK-simulator (right)

ative consideration the Linear Elastic Swelling Model described in Nguyen et al. (2007) was also used in Rutqvist et al. (2011), but the swelling pressure development obtained with the Barcelona Basic Model is considered more realistic in Rutqvist et al. (2011).

From Fig. 4.13 (left), it is apparent that the bentonite cube reaches full water saturation at around t = 10d, with water saturation $S_l = 1$ in the upper region. As expected, saturation occurs earlier in the middle of the cube (red solid and dashed curves) than at the top of the cube (green solid and dashed curves). The water saturation increases monotonically over time, while the gas pressure reaches a maximum of about p_g

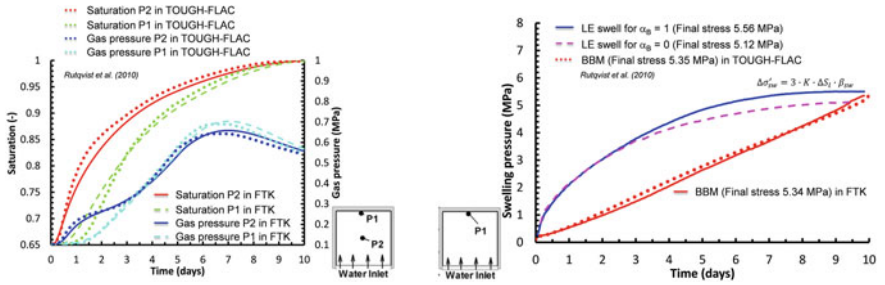

Fig. 4.13 Time-dependent water saturation, gas pressure (left) and swelling pressure (right) in bentonite cube–simulation results–TOUGH-FLAC-simulator (Rutqvist et al., 2011) and FTK-simulator

$\approx$ 0.6–0.7 MPa at around t = 6.5d and then decreases. The reason for this is that the initially present air in the pore space is compressed by the rising water level in the upper region of the cube during the first days, but then gets gradually squeezed out passing the water molecules on the bottom of the cube due to the compression-induced rising gas pressure. This process leads to a gradual reduction of the gas pressure, which is not yet complete even at the end of the simulation, as the water pressure and gas pressure must reach the level of the water pressure in the reservoir at the bottom of the bentonite cube at complete saturation. Figure 4.13(right) shows that the swelling pressure reaches a level of about $p_{\text{swelling}} \approx$ 5–5.5 MPa at the end of the saturation process, which is in good agreement with the observed swelling pressure in Alonso et al. (2005b), according to Rutqvist et al. (2011).

From Figs. 4.12 and 4.13, it is clear that the numerical results obtained using the TOUGH-FLAC-simulator and the FTK-simulator are very similar, thus the validation of the FTK-simulator in terms of the implementation of the Barcelona Basic Model for the physical modeling of the swelling behavior of bentonite appears to be successful.

4.2.3 Validation of the Implementation of the Barcelona Basic Model (BBM) into the FTK-Simulator Via Retrospective Analysis of the China-Mock-Up-Experiment

As part of a retrospective analysis of the measured test data for the Chinese Mock-up Test on GMZ, BRIUG has performed several numerical simulations, as documented in BRIUG (2014). These simulations included thermal, thermally-hydraulically coupled, and thermally-hydraulically-mechanically coupled simulations using the finite element code LAGAMINE. These simulations have been performed using simplified, rotationally symmetric 2D-models without considering the joints between the bentonite blocks. The diffusion of water vapor resulting from evaporation processes

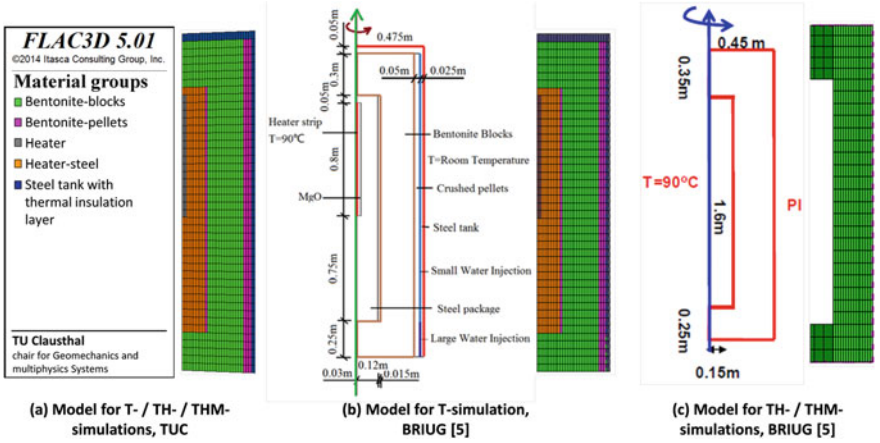

Fig. 4.14 Rotationally symmetric simulation model for retrospective analysis of Chinese Mock-up Test on GMZ: comparison of FTK-simulator **a** at Chair of Geomechanics and multiphysics Systems and LAGAMINE-simulator **b** and **c** at BRIUG

in the existing pore air was considered in all simulations, as it was necessary to reproduce the measured data on the time-dependent development of relative humidity in different measurement positions.

TUC has also done the retrospective analyses performed at BRIUG, but using the FTK-simulator with a similarly simplified rotationally symmetric 3D-segment model. The rotationally symmetric 3D-segment model used in the FTK-simulator, as shown in Fig. 4.14a, represents an 11.25° -segment of a cylindrical structure. This significantly reduces the needed computational effort compared to a simulation with a full 3D-cylinder model. This computational model is used at the Chair of Geomechanics and multiphysics Systems for all simulations performed with the FTK-simulator for the China Mock-up Test on GMZ (thermal / thermally-hydraulically coupled/thermally-hydraulically-mechanically coupled). In contrast, BRIUG (2014) used different models for thermal, thermally-hydraulically and thermally-hydraulically-mechanically coupled simulations, as shown in Fig. 4.14b, c.

As seen in Fig. 4.14, the heater core (gray zones), which represents the actual heat source, is not modeled with its planned height of 1.600 mm, but only with a height of 800 mm. Therefore, only the upper half of the heater is considered in the model. This is because the lower half of the heater was malfunctioning at the time of activation and could not be fixed after the test setup was completed. The radius of the heater core is 30 mm and it is surrounded by a steel jacket (brown zones) with a radius of 150 mm. A layer of bentonite pellets (magenta zones) with a thickness of 15 mm surrounds the heater and separates it from the compacted bentonite blocks (green zones), whose outer radius is 400 mm. To prevent direct contact between the compacted bentonite blocks and the surrounding steel cylinder, a layer of bentonite pellets with 50 mm thickness is placed around the bentonite blocks.

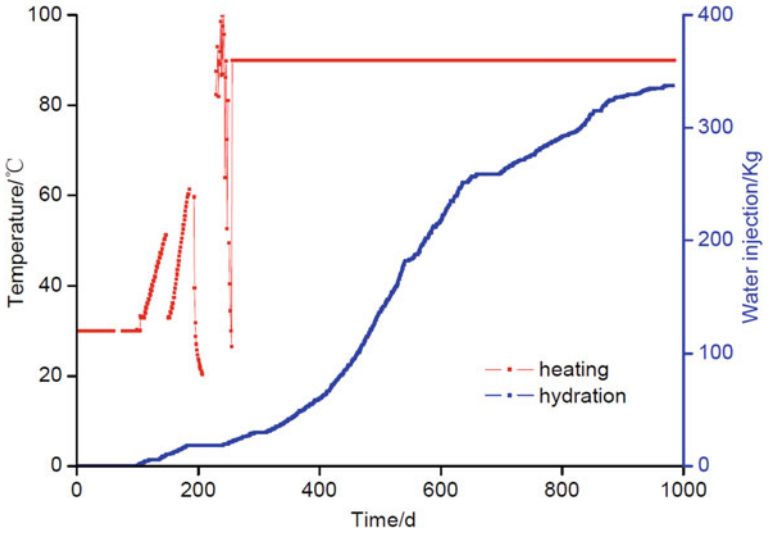

Fig. 4.15 Time-dependent heater temperature and injected water quantity, as documented in BRIUG (2014)

For the retrospective analysis of this TH2M-coupled large-scale experiment, various physical quantities must be taken into account. The most straightforward quantity to model in numerical simulations is the temperature at different positions of the experimental setup, as the temperature distribution primarily depends on the time-dependent heater temperature shown in Fig. 4.15 and the room temperature shown in Fig. 4.16. Although the temperature distribution is also influenced by the thermal conductivity and heat capacity of the bentonite sample, these factors are not significantly affected by other physical quantities, but mainly from water saturation of the bentonite pore space.

However, since the time-dependent heater temperature shown in Fig. 4.15 is relatively complex, the time-dependent heater temperature used in the numerical simulations documented in BRIUG (2014) is simplified as shown in Fig. 4.16.

(a) Thermal Simulation

In accordance to the procedure documented in BRIUG (2014), the TUC-retrospective analysis of the large-scale bentonite test performed at BRIUG uses the FTK-simulator to initially consider only the thermal processes. Figure 4.17(left) shows the temperature distributions obtained with the FTK- simulator at three different times (top) and the simulation results obtained at BRIUG for the temperature distribution at the same times (bottom). It can be seen that the simulation results of the FTK-simulator are in good agreement with the simulation results of BRIUG. In both simulations, temperatures initially increase rapidly in the first few months after the start of the test, with larger temperature increases observed near the heater than farer away from the

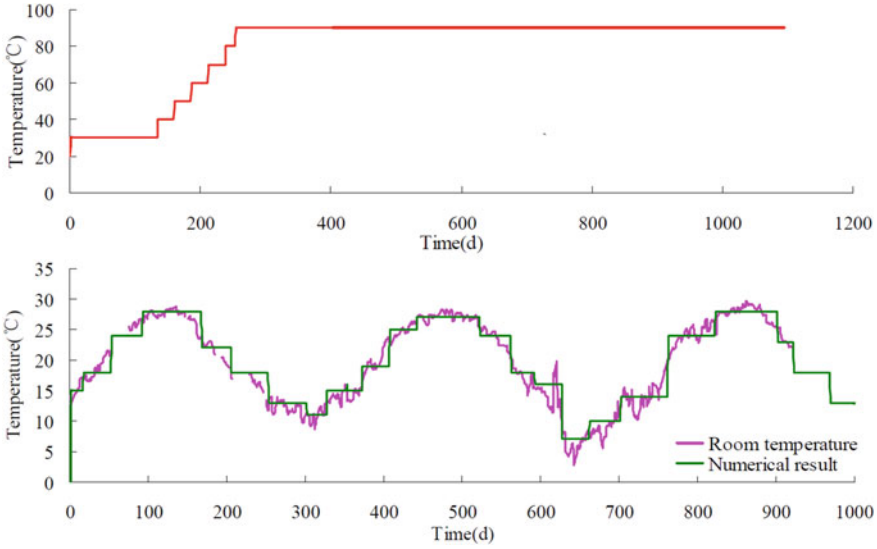

Fig. 4.16 Simplified time-dependent heater temperature and room temperature, as documented in BRIUG (2014)

heater, as expected. With increasing distance from the heater, temperatures approach the outer boundary condition (room temperature outside of the test setup).

As can be seen from Fig. 4.17 (right), the time-dependent temperature developments at selected positions of the specimen obtained with the FTK-simulator are in good agreement with the corresponding time-dependent temperature developments obtained at BRIUG. Additionally, the simulation results of both simulators are consistent with the measured data which are also shown in Fig. 4.17 (right). This validates the use of the FTK-simulator for the case of exclusively thermal simulation.

(b) Thermally-hydraulically coupled simulation

In BRIUG (2014), simulation results of thermally-hydraulically coupled simulations for the large-scale bentonite test are documented, in addition to the simulation results of the exclusively thermal simulations described above. These simulation results were also used to validate the FTK-simulator.

In the thermally-hydraulically coupled simulations of the test, the heat output of the heaters is specified the same as in the thermal-only simulations. The water injection rate applied to the outer edge of the test structure is based on Fig. 4.6. Similar to the procedure documented in BRIUG (2014), a non-uniform water supply is assumed in the lower area of the test structure than the rest of the bentonite block structure, taking into account the effect of gravity within the water injection area.

The simulation is performed here only up to time t = 430 d after the start of the experiment, since no further simulation results are given in BRIUG (2014) for later times of the experiment that can be used to validate the FTK-simulator.

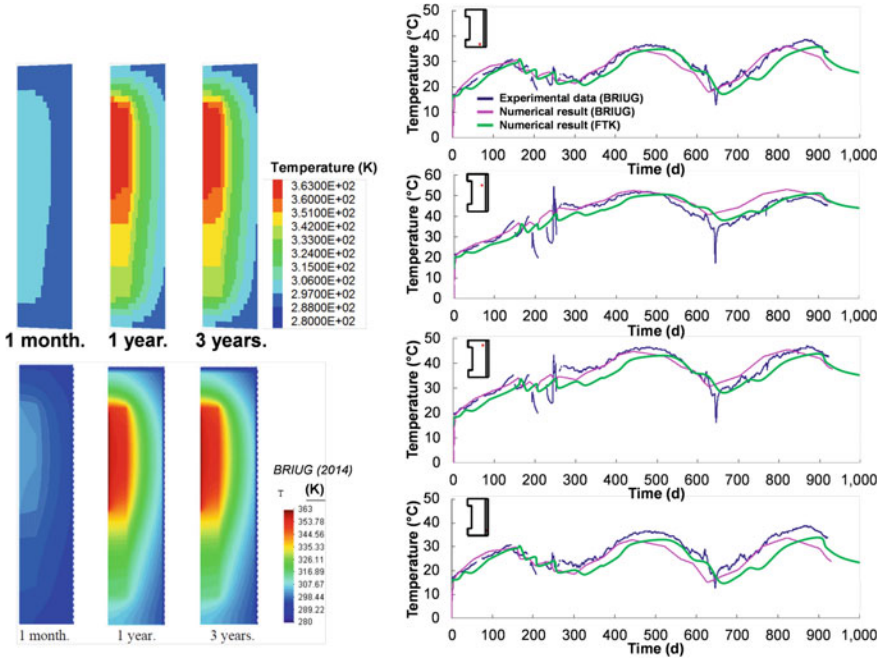

Fig. 4.17 Temperature distribution in bentonite block structure at t_1 = 30 d, t_2 = 1 a, and t_3 = 3 a after test start (left): comparison of FTK-simulator (top) and LAGAMINE-simulator (bottom) results with BRIUG (2014); time-dependent temperature in different areas of the bentonite block structure (right)

Figure 4.18(left) shows a comparison of the pore water pressure distribution obtained with the FTK-simulator at times t_1 = 30 d, t_2 = 200 d and t_3 = 430 d, with corresponding results shown in BRIUG (2014). It can be seen that the pore water pressure near the heater increases over time, from an initial value of $p_1 \approx$ –93 MPa to $p_1 <$ –283 MPa, indicating a decrease in water saturation and therefore an increase in capillary pressure. Analysis of the simulation results reveals that this decrease in water saturation is caused by evaporation of pore water in the pore space of the bentonite block structure, which may also be considered in the FTK-simulator. The evaporation process is dominated by the simultaneous thermally-induced expansion of liquid water, resulting in the superposition of these two processes not causing a decrease in saturation. However, the decrease in saturation can be explained by analyzing the influence of water vapor diffusion resulting from the evaporation of pore water in the gas phase. The diffusion direction is oriented to the concentration gradient, so the water vapor moves from areas of higher concentration to areas of lower concentration, from the heater near-field to cooler areas of the bentonite block structure. This causes further pore water to evaporate in the heater near-field, resulting in a gradual decrease in saturation.

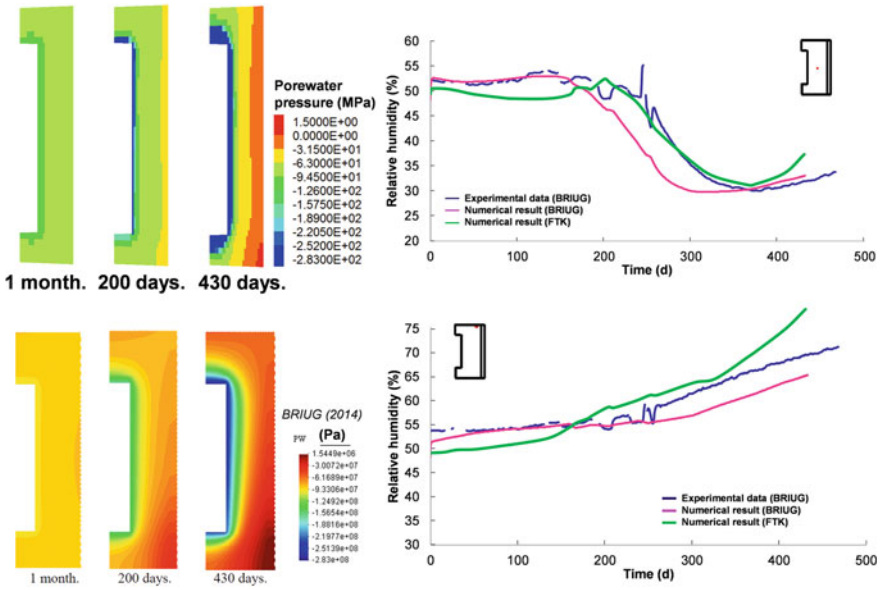

Fig. 4.18 Pore water pressure distribution in bentonite block structure at t_1 = 30 d, t_2 = 200 d, and t_3 = 430 d after test start (left): comparison of FTK-simulator (top) and LAGAMINE-simulator (bottom) results with BRIUG (2014); time-dependent relative humidity at chosen locations in the bentonite block structure (right)

The simulation results obtained with the FTK-simulator and those documented in BRIUG (2014) are very similar, but not identical, at the 3 points in time. The discrepancy is attributed to the lack of a specified diffusion coefficient for the diffusion of water vapor in the gas phase in the simulation documented in BRIUG (2014). To achieve a better match, the diffusion coefficient was adjusted in the FTK-simulation by a sensitivity analysis.

In BRIUG (2014), the simulation results for selected positions of the bentonite block structure are compared with the corresponding measured values for the time-dependent relative humidity in addition to the extensive representation of the pore water pressure distribution shown in Fig. 4.18(left). As per Fredlund and Rahardjo (1993), the relative humidity RH can be calculated from the capillary pressure p_c and suction $s = p_c$ using Eq. (4.17):

$$RH = \exp\left(\frac{-s \cdot w_v}{R \cdot T \cdot \rho_w}\right) \tag{4.17}$$

s – suction kPa,
w_v – molar mass of water vapor with $w_v \approx 18.016$ g/mol,
R – general gas constant with $R \approx 8.31432$ J/(mol K),
ρ_w – water density with $\rho_w \approx 998$ kg/m^3 at 20 °C, and

T – absolute temperature with $T = (273.16 + \frac{\theta}{1°C})K$, where θ is temperature in °C.

The results of the FTK-simulator are in good agreement with the measured values as well as with the simulation results from BRIUG (2014) for the time-dependent development of relative humidity at two selected positions within the bentonite block structure, as shown in Fig. 4.18(right). The relative humidity at one position decreases due to the diffusion of water vapor resulting from evaporation into cooler areas, while at the other position it increases continuously due to distance from the heater and proximity to the external water supply. The validation of the FTK-simulator has been successful for the case of thermally-hydraulically coupled simulations.

(c) Thermally-hydraulically-mechanically coupled simulation

In BRIUG (2013), a thermally-hydraulically-mechanically coupled simulation for the large-scale bentonite test is documented, along with some related simulation results. The Barcelona Basic Model (BBM) was used to model the mechanical behavior of the bentonite material, as it also accounts for the swelling pressure development. However, it should be noted that different material parameters and initial and boundary conditions were applied in this simulation, as it was not a retrospective analysis but a prognostic numerical simulation.

The thermally-hydraulically-mechanically coupled simulation using the FTK-simulator was able to replicate the results from BRIUG (2013) in terms of temperature, degree of saturation and suction development for a horizontal section at half height of the bentonite block structure, as shown in Fig. 4.19. However, some material parameters had to be estimated due to a lack of sufficient information in BRIUG (2013).

In BRIUG (2013), the time-dependent development of the swelling pressure calculated in the simulation is also documented for a selected observation point 'A', which is located nearly at half height of the bentonite block structure in direct contact with the heater surface, as shown in Fig. 4.19(left). It can be seen that a swelling pressure of about $p_{\text{swelling}} = 0.55$ MPa builds up relatively quickly at observation point 'A' within the first 6 months after the start of the test, which then continues to rise at a lower rate up to about $p_{\text{swelling}} = 1.45$ MPa until the end of the simulation. As can be seen from Fig. 4.19(right), the shape of the swelling pressure development curve shown in BRIUG (2013) could unfortunately not be reproduced with the FTK-simulator, since at the FTK-simulation the swelling pressure increases only slowly at first and then more and more rapidly with increasing saturation. Nevertheless, the validation of the FTK-simulator for the case of the thermally-hydraulically-mechanically coupled simulation appears to be largely successful.

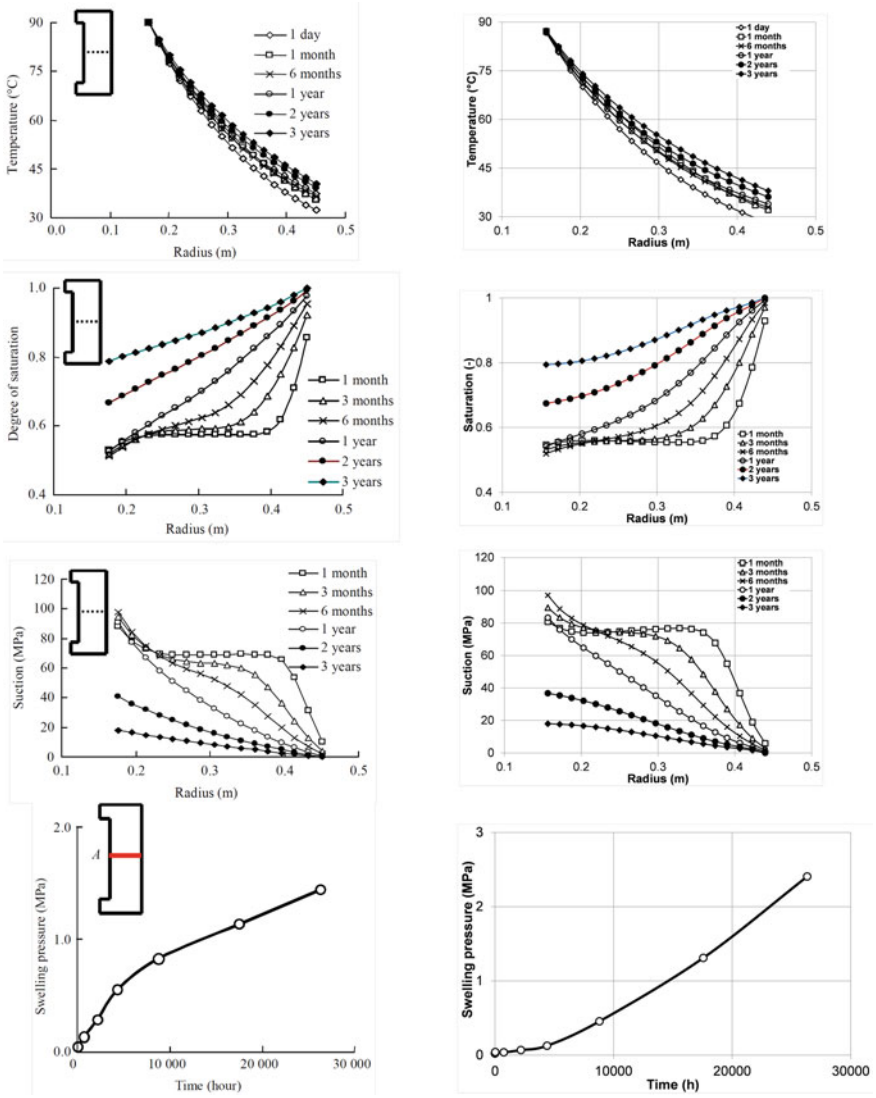

Fig. 4.19 Time-dependent development of temperature, water saturation, suction, and swelling pressure in a horizontal section nearly at half height of the bentonite block structure (left: LAGAMINE-simulator BRIUG (2013), right: FTK-simulator)

4.3 THM–Modelling of Mock-Up Test in LAGAMINE

Jingbo Zhao, Liang Chen, Ju Wang, Yuemiao Liu, Shengfei Cao, Qi Zhang

4.3.1 Description of the Coupled THM

Based on previous experiments, we have introduced a constitutive model (Chen et al., 2012b; Zhao et al., 2016) to replicate the principal THM coupling behavior of GMZ bentonite. Our model incorporates the transfer of heat, moisture (in liquid water and water vapor form), and air in a deformable, unsaturated soil, while also utilizing the BBM model to simulate mechanical behavior. This section provides a brief introduction to our proposed model.

4.3.1.1 Mass Conservation of the Phases

For water, the mass conservation equation is derived by adding the balance equation of liquid water and water vapor. This equation considers changes in water storage and the divergence of water flow in each phase, as Collin et al. (2002) explains:

$$\frac{\partial \text{æ}_{\mathrm{w}} n S_{\mathrm{r,w}}}{\partial t} + div(\rho_{\mathrm{w}} \underline{f}_{\mathrm{w}}) + \frac{\partial \rho_{\mathrm{v}} n S_{\mathrm{r,g}}}{\partial t} + div(\underline{i}_{\mathrm{v}} \rho_{\mathrm{v}} \underline{f}_{\mathrm{g}}) = 0 \tag{4.18}$$

where ρ_w is the liquid water density, n is the medium porosity, $S_{r,w}$ is water saturation degree in volume, $\underline{f}_{\alpha}$ is the macroscopic velocity of the phase α (α = liquid water, gas), ρ_v is the water vapor density, $S_{r,g}$ is water vapor saturation degree in volume, $\underline{i}_v$ is the non-advective flux of water vapor.

Generally, the medium consists of a mixture of water vapor and dry air. To conserve mass of the dry air, the equation must consider the contributions of both the dry air and the dissolved air in water, which can be mathematically expressed as:

$$\frac{\partial \rho_a n S_{\mathrm{r,g}}}{\partial t} + div(\underline{i}_a + \rho_a \underline{f}_{\mathrm{g}}) + \frac{\partial H \rho_a n S_{\mathrm{r,w}}}{\partial t} + div(H \rho_a \underline{f}_w) = 0 \tag{4.19}$$

where $\underline{i}_a$ is the non-advective flux of dry air, ρ_a is dry air density and H is Henry's coefficient.

4.3.1.2 Momentum Conservation of the Phases

The generalized Darcy's law for multiphase porous medium gives the velocity:

$$\underline{f}_{\alpha} = -\frac{k_{int} k_{\mathrm{r},\alpha}}{\mu_{\alpha}} [\underline{\nabla} p_{\alpha} + \rho_{\alpha} g \underline{\nabla} y] \tag{4.20}$$

where p_{α} is the pressure of the phase α, g is the gravitational acceleration, u_{α} is the dynamic viscosity of the phase α, k_{int} is the intrinsic permeability, and $k_{\mathrm{r},\alpha}$ is the relative permeability of the phase α, α=liquid water, gas.

In a convoluted medium, both water vapor and dry air are assumed to adhere to Fick's diffusion law, as formulated by Philip and De Vries (1957b):

$$\underline{i}_{\alpha} = -D_{\mathrm{atm}} \tau_{\mathrm{v}} n S_{\mathrm{r,g}} \underline{\nabla} \rho_{\alpha} \tag{4.21}$$

where D_{atm} is the molecular diffusion coefficient, and τ_v is the tortuosity, α = water vapor, dry air.

4.3.1.3 Energy Conservation of the Phases

Regarding the thermal problem, we assume that there is equilibrium between the phases, resulting in the same temperature for all phases. The total enthalpy of the system can then be expressed as the sum of each component's enthalpy:

$$\begin{aligned}\phi = {} & n S_{\mathrm{r,w}} \rho_{\mathrm{w}} c_{\mathrm{p,w}} (T - T_0) + n S_{\mathrm{r,g}} \rho_{\mathrm{a}} c_{\mathrm{p,a}} (T - T_0) + (1 - n) \rho_{\mathrm{s}} c_{\mathrm{p,s}} (T - T_0) + \\ & n S_{\mathrm{r,g}} \rho_{\mathrm{v}} c_{\mathrm{p,v}} (T - T_0) + n S_{\mathrm{r,g}} \rho_{\mathrm{v}} L\end{aligned} \tag{4.22}$$

where T is the temperature, T_0 is definition temperature, $c_{\mathrm{p},\alpha}$ is the specific heat of the phase α (α= solid, liquid water, gas), ρ_s is the solid density, The last enthalpy term corresponds to the heat stored during the water vaporization.

In this medium, heat is transported through conduction, convection, and vaporization, as shown in the following equation:

$$\begin{aligned}q = {} & -\Gamma \underline{\nabla} T + (\underline{i}_{\mathrm{v}} + \rho_{\mathrm{v}} \underline{f}_{\mathrm{g}}) L + \\ & [c_{\mathrm{p,w}} \rho_{\mathrm{w}} \underline{f}_{\mathrm{w}} + c_{\mathrm{p,a}} (\underline{i}_{\mathrm{a}} + \rho_{\mathrm{a}} \underline{f}_{\mathrm{g}}) + c_{\mathrm{p,v}} (\underline{i}_{\mathrm{v}} + \rho_{\mathrm{v}} \underline{f}_{\mathrm{g}})](T - T_0)\end{aligned} \tag{4.23}$$

where Γ is the medium conductivity.

Neglecting the terms for kinetic energy and pressure energy, we can ultimately obtain the energy balance:

$$\frac{\partial \phi}{\partial t} + div(q) - Q = 0 \tag{4.24}$$

Q is a volume heat source.

4.3.1.4 Mechanical Model

For the BBM (Alonso et al., 1999), the yield surfaces are composed of three parts. In the (p, q) space, for a given suction, the yield surface can be written as:

$$q^2 - M^2(p + p_s)(p_0 - p) = 0 \tag{4.25}$$

where p is the mean stress, q is the deviatoric stress, M is the slop of the critical line, p_s is the soil strength in extension and p_0 is the pre-consolidation pressure.

In the (p, s) space, pre-consolidation pressure p_0 varies with the suction s, which is well known as the LC curve:

$$p_0 = p_c \left(\frac{p_0^*}{p_c} \right)^{\frac{\lambda(0)-k}{\lambda(s)-k}} \tag{4.26}$$

where p_c is a reference pressure, ${p_0}^*$ is the pre-consolidation in saturated condition, k is the elastic slope of the compressibility curve against the net mean stress, $\lambda(s)$ refers to the plastic slope of the compressibility curve against the net mean stress and $\lambda(0)$ is the plastic slope in saturated condition. The relationship between $\lambda(s)$ and $\lambda(0)$ can be expressed as:

$$\lambda(s) = \lambda(0)[(1 - \gamma)\exp(-\beta s) + \gamma] \tag{4.27}$$

where γ and β are the parameters describing the changes in soil stiffness with suction. When the soil is saturated, $\lambda(s)$ is equal to $\lambda(0)$.

The confirmed phenomenon of suction variations causing irreversible volumetric deformations has led to the adoption Thus the following yield locus named SI is adopted:

$$F_2 = s - s_0 = 0 \tag{4.28}$$

where s is the suction and s_0 is the maximum historic suction of the soil.

The evolution of the yield surface is controlled by the hardening parameters ${p_0}^*$ and $s_{0.}$ They depend on the total plastic volumetric strain increment $d{\varepsilon_v}^p$ as follows:

$$dp_0^* = \frac{(1 + e)p_0^*}{\lambda(0) - \kappa} d\varepsilon_v^p \tag{4.29}$$

$$ds_0 = \frac{(1 + e)(s_0 + P_{at})}{\lambda_s - k_s} d\varepsilon_v^p \tag{4.30}$$

where e is the porosity of the soil, p_{at} is the atmosphere pressure, k_s and λ_s are the elastic and plastic stiffness parameter for suction variation, respectively.

4.3.2 Model Setup

4.3.2.1 Geometry and Boundary Conditions

A two-dimensional axisymmetric numerical model is proposed due to the symmetrical nature of the infrastructure of the China mock-up. The program LAGAMINE was utilized to discretize the model domain using rectangular grids which consisted of 4244 nodes and 1482 elements, as shown in Fig. 4.20. The mesh clearly highlighted the five different material zones. The thermal and hydraulic boundary conditions were controlled by heating and hydration systems, while the nodes were subjected to a fixed horizontal/vertical displacement at x=0 and y=0 respectively. In this section, we present numerical simulations conducted over a period of 1800 days using experimental data between April 1, 2011, and December 31, 2015. It is important to note that April 1, 2011, was designated as "day 0" on the time scale in the model.

The numerical simulation of the heater strip entails a heating process that occurs in three stages. Initially, for the first 135 days, the temperature was maintained at 30 °C. Next, from day 136 to day 1800, the temperature gradually increased to 90 °C. Finally,

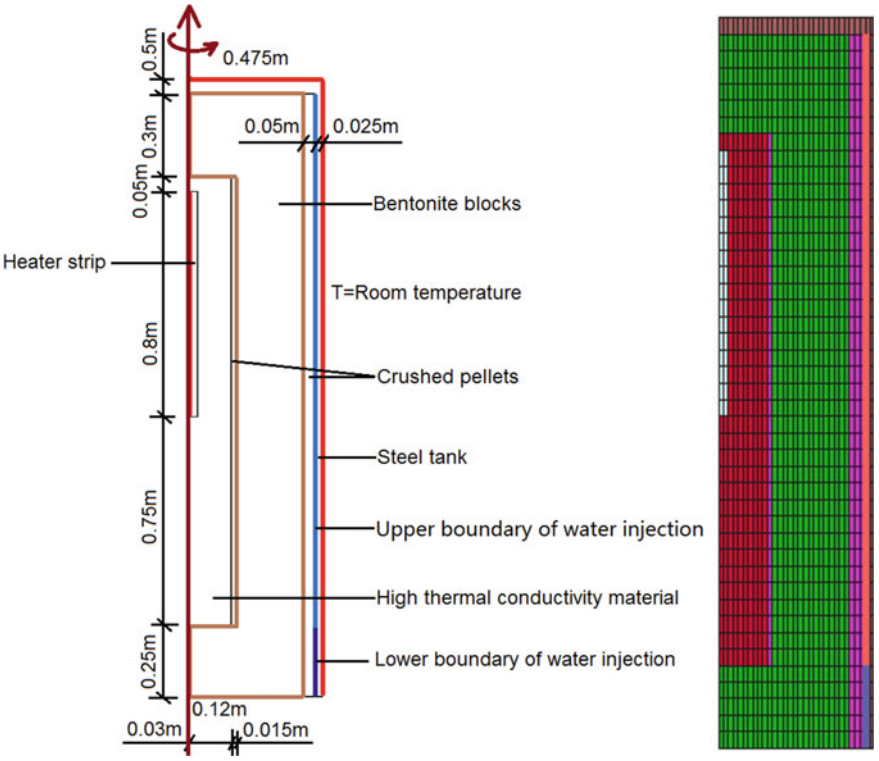

Fig. 4.20 Boundary conditions and meshes (unit: mm)

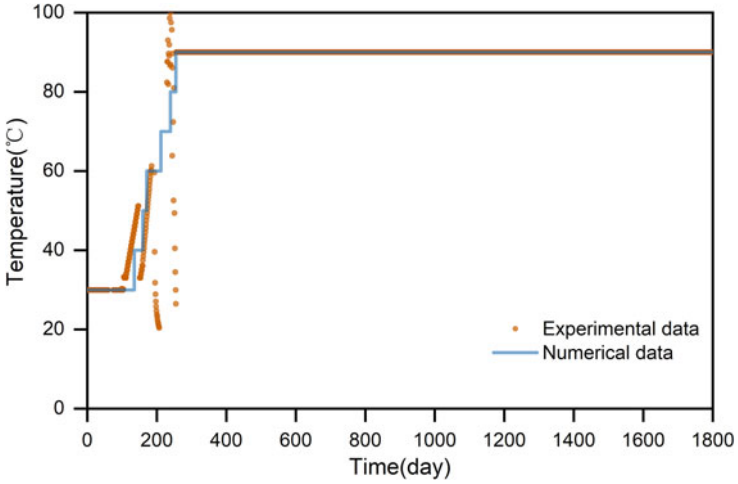

Fig. 4.21 Heating process of the heater strip

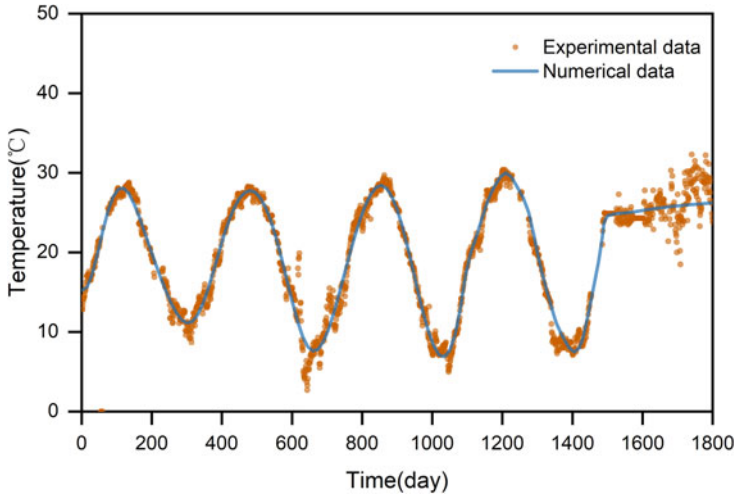

Fig. 4.22 Variation in room temperature with time

the temperature remained constant for the remainder of the test, as depicted in Fig. 4.21. Although the thermal insulation materials were installed on the outer surface of the China-mock-up facility, the interior temperature was significantly influenced by the variation of the room temperature. To account for this, we considered the room temperature as the outer thermal boundary condition and defined it as a piecewise function in the model using recorded data, as shown in Fig. 4.22.

In the China-mock-up test, the hydration process is regulated by a rate of water injection. The total mass variation of water injection is displayed in Fig. 4.23a. The

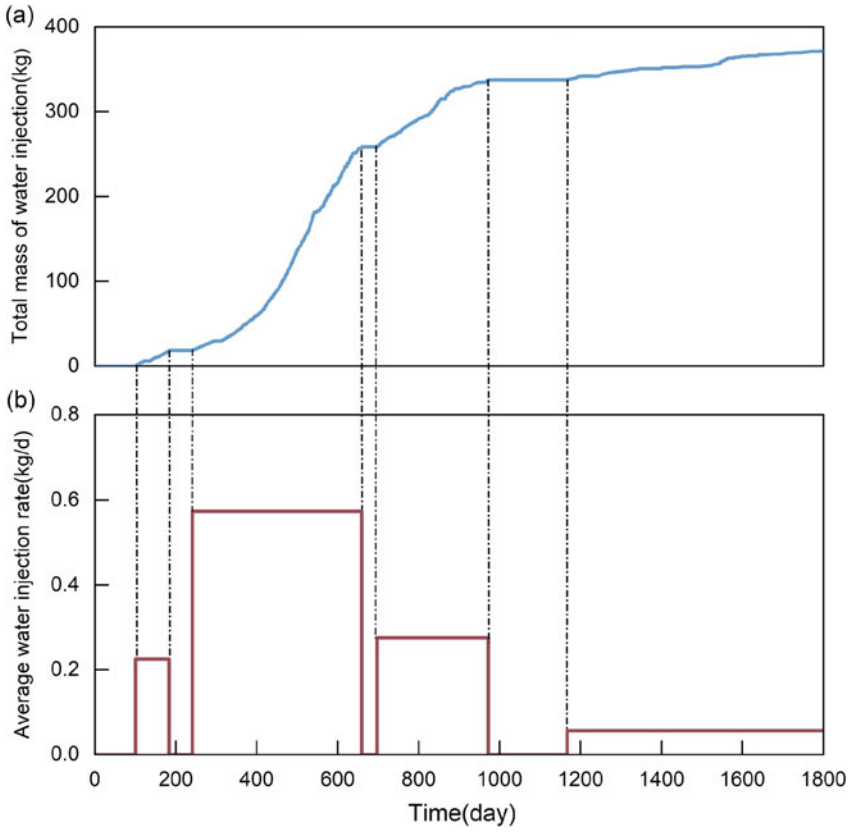

Fig. 4.23 Water injection process of China-mock-up

average water injection rate was used in the numerical model to depict the water injection process on the right boundary, as illustrated in Fig. 4.23b. The remaining borders were assigned a default zero-flow boundary condition. In fact, the hydration process on the right boundary in the vertical direction was inhomogeneous due to the gravity effect. As there was no experimental data available on water injection rate, the right boundary was divided into two parts, namely upper and lower boundary (see Fig. 4.20). During the initial hydration stage, the majority of the injected water accumulated at the bottom, resulting in a higher injection rate at the lower boundary than the upper boundary. As the bentonite at the bottom became saturated, the injection of water in this area became less impactful.

In the numerical model, the GMZ bentonite was initially saturated with 31 % water and had a suction of 80 MPa. To achieve better numerical convergence, the gas pressure was held constant and dissolved air in water was not taken into account. In the hydro-mechanical simulation, the study focused on compacted bentonite blocks and crushed pellets. The water content and stresses in the heater strip, high thermal

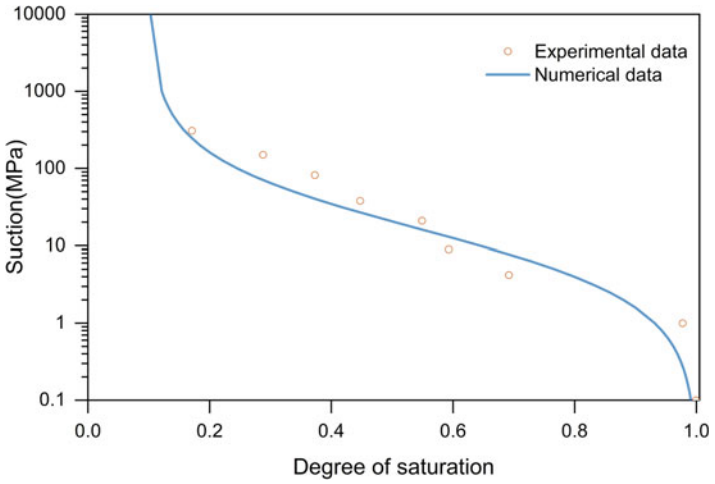

Fig. 4.24 Water retention curve of the GMZ bentonite

conductivity material, and steel tank remained constant throughout the heating and hydration process.

4.3.2.2 Model Parameters Setting

Among the hydrothermal properties, the soil water characteristic curve plays a crucial role in determining water intake volume and the degree of saturation variation. Chen et al. (2015) proposed the following correlation between suction and degree of saturation, based on their experimental investigation of GMZ bentonite:

$$S_{\mathrm{r,w}} = S_{\mathrm{r,res}} + a_3 \frac{S_{\mathrm{r,u}} - S_{\mathrm{r,res}}}{a_3 + (a_1 s)^{a_2}} \tag{4.31}$$

Where $S_{r,u}$ is the maximum degree of saturation in the soil, $S_{r,res}$ is the residual degree of saturation for a very high value of suction, and a_i is the parameters (i=1,2,3).

For the compacted bentonite, values of $S_{r,u}$ and $S_{r,res}$ are 1.0 and 0.1, According to the numerical results of soil water retention curve shown in Fig. 4.24, the values of the parameters a_i can be obtained: $a_1 = 7.0\times10^{-6}$ Pa^{-1}, $a_2 = 0.9$, $a_3 = 70$.

The unsaturated hydraulic conductivity of the bentonite is highly dependent on the degree of saturation $S_{r,u}$. According to the unsaturated permeability test (Chen et al., 2015), the intrinsic permeability of saturated GMZ bentonite is about $k_{int} = 2.5\times10^{-20}$ m^2. An empirical relationship for the relative permeability of the bentonite in terms of the degree of saturation is given as follows in Fig. 4.25:

$$k_{\mathrm{r,w}} = \frac{(S_{\mathrm{r,w}} - S_{\mathrm{r,res}})^3}{(S_{\mathrm{r,u}} - S_{\mathrm{r,res}})^3} \tag{4.32}$$

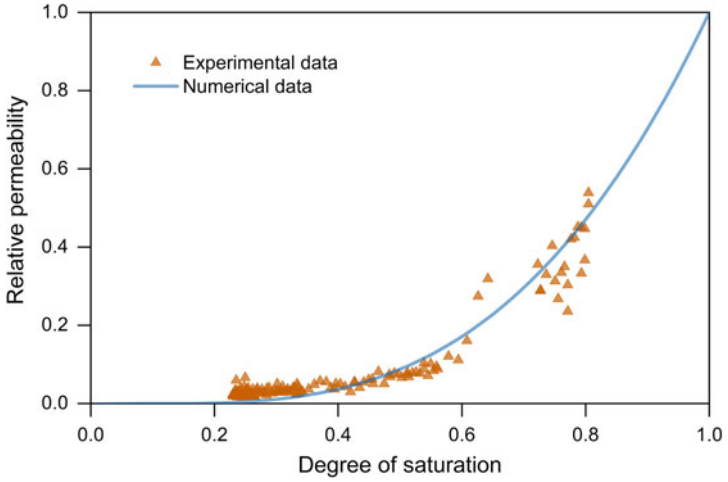

Fig. 4.25 Relative permeability of the GMZ bentonite as a function of degree of saturation

The relationship between thermal conductivity and water content is linear, as noted in the study by Zhao et al. (2016), which also presents other parameters describing the hydrothermal and mechanical properties.

4.3.3 Result Analysis

4.3.3.1 Thermal Response

The temperature at various locations was compared between the predicted and experimental results. These comparisons are shown in Fig. 4.26. Initially, the temperature increased due to the heating process during the first 255 days. However, the subsequent temperature fluctuations were primarily caused by the room temperature variations and the heating process, resulting in minor thermal fluctuations. For example, Figs. 4.21 and 4.22 illustrate that the temperature of the heater strip remained at 60°C from the 180th to the 212th day. The room temperature was the dominant factor during this period and caused a more pronounced decrease in temperature. Subsequently, on the 212th day, the temperature of the heater strip was increased to 70°C, resulting in a corresponding temperature increase due to heating. As the temperature field approached steady state, the room temperature once again became a significant factor and caused a noticeable decrease in overall temperature.

Good agreement is evident between the experimental data and the numerical results both at the bottom (Fig. 4.26a, b) and in the middle section of the facility (Fig. 4.26c, d). Notably, minor temperature fluctuations are accurately reproduced in the numerical modeling. For instance, a significant temperature fluctuation is observed

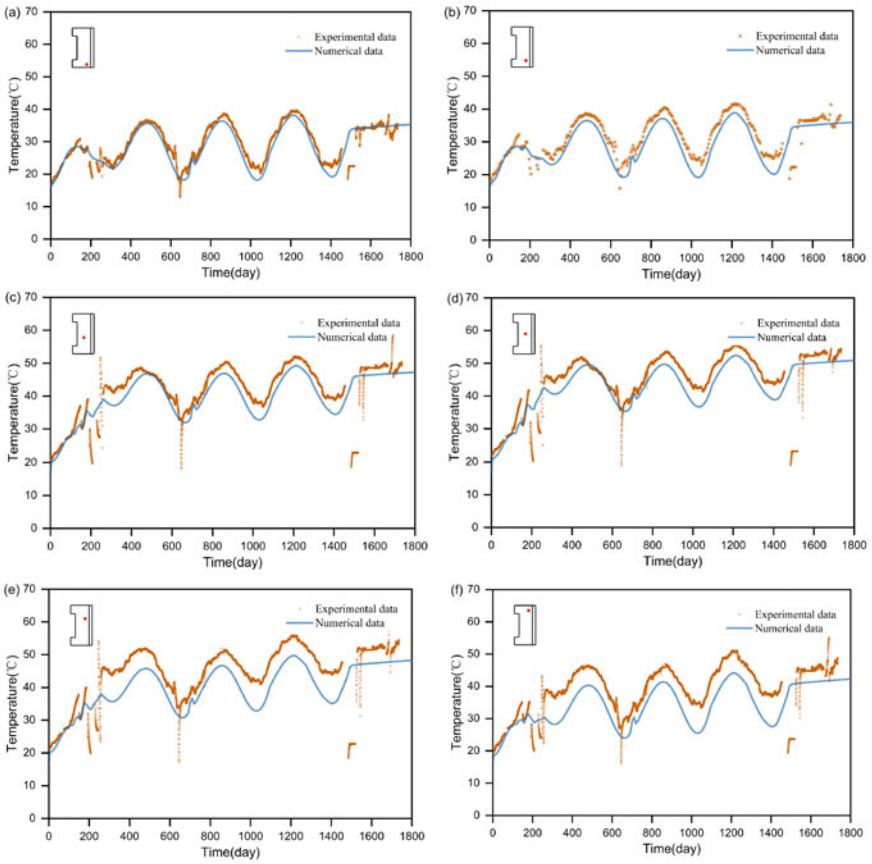

Fig. 4.26 Comparison of the predictive temperature with the experimental results at different locations of the China-mock-up facility

from the 700th to the 720th day, and the numerical analysis replicates this observation effectively. However, a relatively significant difference between the predicted and experimental results is observed in the upper zone of the facility (Fig. 4.26e, f). This disparity can be attributed to various factors, such as non-uniform hydration rates and improved thermal insulation conditions at the top of the facility. The authors suggest that simplifications in gas transportation may be a key factor. In reality, as the heating process progresses, heat energy gradually accumulates in the upper zone, leading to a temperature increase. In numerical simulations, gas pressure is assumed to be constant, so the gas velocity caused by pressure differences is not considered, and the heat transfer induced by gas pressure differences is not represented in the numerical study. Additionally, it's observed that room temperature remains stable from the 1510th day in Fig. 4.22, and the simulated temperature effectively replicates this phenomenon.

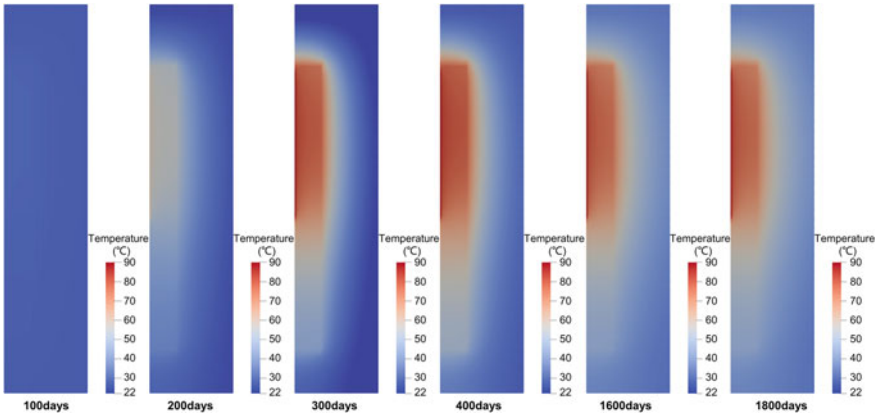

Fig. 4.27 Temperature distribution at different times

Figure 4.27 presents that the distribution of temperature with time during the heating process. The heater strip and room temperature have an obvious influence on the temperature distribution. In the first 135 days the temperature of the heat strip was kept at 30 °C that was close to room temperature. Thus, there does not exist the difference of the temperature distribution in the model domain at time 100days. Then with the increase of the temperature of the heat strip from 136 days to 255 days, the influence of the heat stirp on the temperature distribution became a dominant factor. This phenomenon could be found at times of 100 days, 200 days, 300 days in Fig. 4.27. When the temperature field was close to the steady state, the room temperature has a significant impact on the temperature distribution. For instance, the room temperature was relatively low at time 300 days. The corresponding temperature close to the boundary was also low and changed with the increase of the room temperature. Until the room temperature gradually reached to a stable condition after 1510 days, the temperature distribution in the domain almost keep the same at times of 1600 days and 1800 days.

4.3.3.2 Hydraulic Response

Figure 4.28 presents the predicted relative humidity distributions at various locations within the facility. Initially, relative humidity remained relatively constant before the hydration process, and the simulated relative humidity closely matched experimental data for this period. However, as the hydration process commenced, relative humidity variations became more significant. Notably, in areas near the electrical heater (Fig. 4.28b, c, d, e), a desaturation-saturation process occurred. This was attributed to the interplay between saturation due to water penetration and drying caused by the heater. The low permeability of GMZ bentonite meant that the drying effect initially dominated. While the numerical study showed good overall agreement with

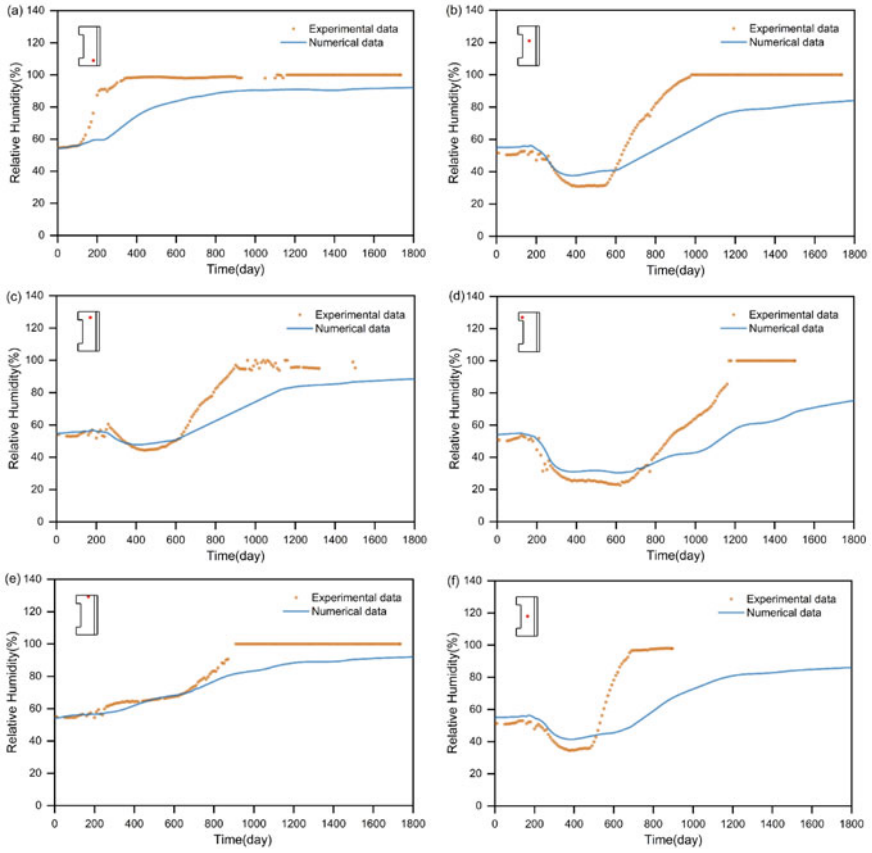

Fig. 4.28 Comparison of the predictive relative humidity with the experimental results at different locations of the China-mock-up facility

experimental data, the variation in relative humidity was slower than observed in the experiments. This difference is largely attributed to the presence of gaps between the compacted bentonite blocks. In the experiments, water initially penetrated into the blocks through these gaps or along sensor cables. In the numerical study, the compacted bentonite blocks were assumed to be homogeneous, neglecting the existence of gaps. As a result, the predicted saturation and desaturation were less pronounced than the experimental measurements, as also evident in Fig. 4.29.

Figure 4.29 presents porewater pressure distribution at different times. The simulated results shows that the compacted bentonite has not yet reached saturation after 1800 days.The maximum of porewater pressure is –9.2 MPa. The saturated process was much slower than the experimental data due to the neglect of the gaps in the model. Besides, a desaturation-saturation process could be clearly presented due to the heating process at times of 200 days, 600 days, 1200 days.The minimum of

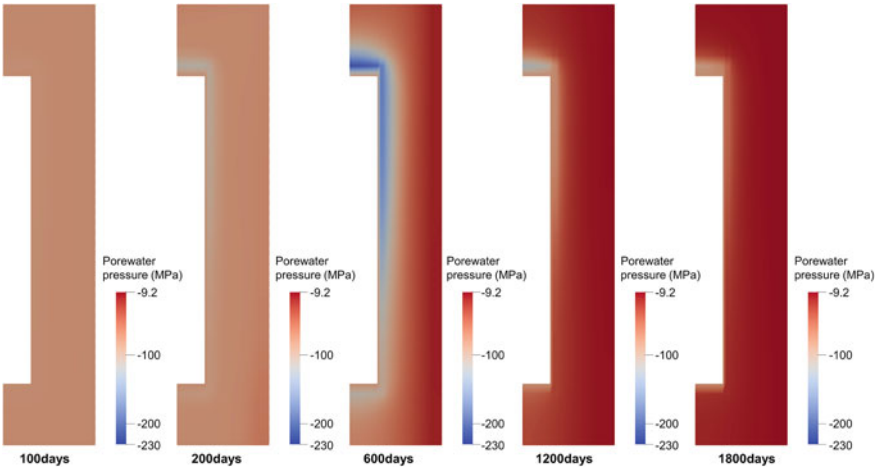

Fig. 4.29 Porewater pressure distribution at different times. Only the domains representing compacted bentonite blocks and crushed bentonite pellets are presented here

porewater pressure is around –230 MPa that is much lower than the initial suction. These phenomena keep consistent with the simulated results in Fig. 4.28.

4.3.3.3 Mechanical Response

Figure 4.30 provides a comparison between the predicted swelling pressure and experimental values at different locations. The maximum measured swelling pressure ranged from 0.5 MPa to 2.5 MPa, depending on the location. The proposed model successfully replicated the overall trend of swelling pressure variation, capturing some key characteristics present in the experimental data and predicted results. As shown in Figs. 4.23 and 4.30b, c, e, a pronounced decrease in swelling pressure is observed due to the temporal cessation of water injection from the 972nd to the 1048th day and the drying effect. However, noticeable differences are also observed at certain locations, particularly in points near the hydration boundary. This discrepancy can be partly attributed to the fact that the expansion strain induced by changes in the microstructure of bentonite during the wetting process was not considered in the BBM model (Alonso et al., 1999). Additionally, the omission of stress release resulting from initial gaps between sensors and blocks may be another significant contributing factor.

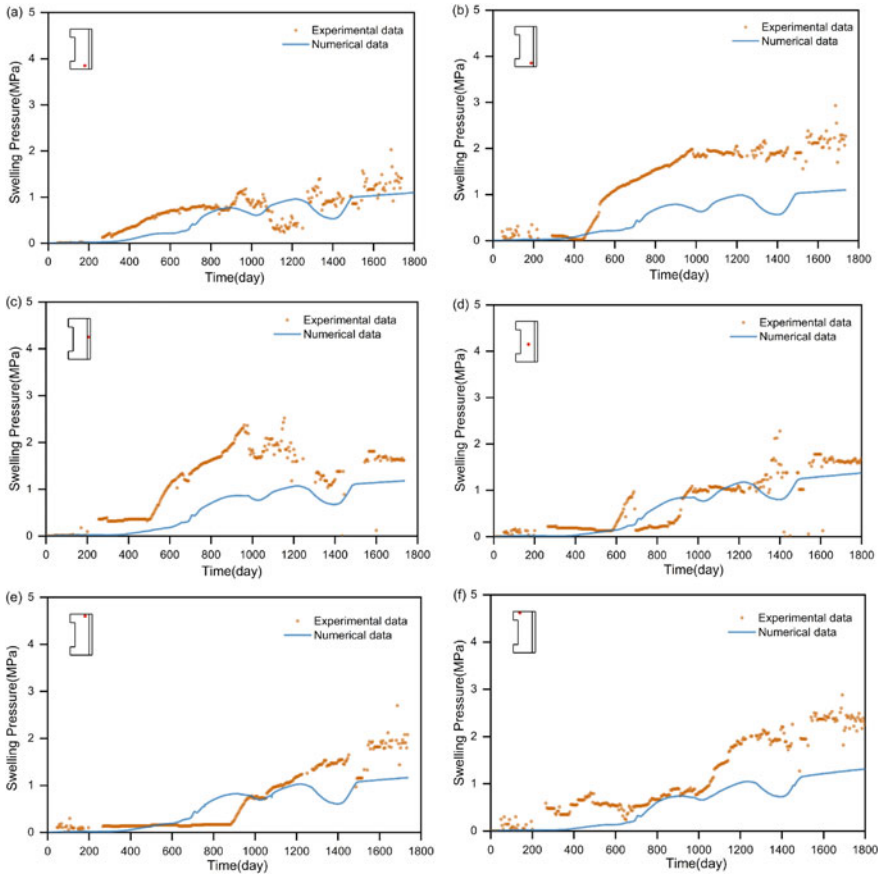

Fig. 4.30 Comparison of the predictive swelling pressure with the experimental results at different locations of the China-mock-up facility

4.4 Diffusion of Radionuclides in Heterogeneous Sediment Formations

Haibing Shao, Chaofan Chen, Tao Yuan, Renchao Lu, Cornelius Fischer, Olaf Kolditz

This chapter is based on the publication by Chen et al. (2022) in a generalized form.

4.4.1 *Upscaling Workflow for Effective Diffusion Coefficient Determination*

In this study, the effective diffusion coefficients are derived through a comprehensive upscaling procedure founded on multiscale digital rock models. These models encompass three key scales: the nanometer scale, micrometer scale, and centimeter scale. At the nanometer scale, digital representations of pore network geometries are meticulously reconstructed from image data acquired using a focused ion beam scanning electron microscope (FIB-SEM). At this level, we take into account the electrostatic diffusion of cations and anions within the diffuse layer, and employ the Donnan approach to calculate the surface electrostatic potential (Appelo and Wersin, 2007; Parkhurst et al., 2013; Yuan and Fischer, 2021). These calculated effective diffusion coefficients at the nanometer scale serve as crucial input parameters for the diffusive transport calculations in the micrometer-scale model.

At the micrometer scale, the digital rock models introduce variability in mineral composition. Transport calculations conducted at the nanometer scale reveal that the effective diffusivity in matrix-supported (MS) texture pores is notably higher, up to two orders of magnitude, in comparison to grain-supported texture pores (GS) and intragranular pores (IG). Consequently, the microstructure of the host rock consists of a combination of highly permeable MS pores and less permeable non-MS pores (GS and IG) (for definition of MS, GS, and IG see Bollermann et al. (2022)). According to the experimental analysis (Bollermann et al., 2022), the clay laminae are comprised of 70% clay mineral aggregates, with 85% being matrix-supported (MS). The mixture of clay and sand layers consists of 50% clay mineral aggregates, with 20% being MS. The carbonate lenses are composed of 54% calcite and 10% clay mineral aggregates, resulting in 5% grain-supported (GS) content and 65% intragranular (IG) content. The effective diffusion coefficient at the micrometer scale is subsequently determined by solving Eqs. (4.33) and (4.34). For a more comprehensive understanding of the upscaling workflow from the nanometer (nm) to the micrometer (μm) scale and the reconstruction of digital rock models, readers are encouraged to refer to the works of Yuan and Fischer (2021) and Bollermann et al. (2022).

The effective diffusivities calculated for the clay laminae, the mixture of clay and sand laminae, and carbonate lenses are employed to estimate the effective diffusivity of the sandy facies of Opalinus Clay (SF-OPA) at the centimeter scale. This estimation takes into account the subfacies compositions, which are quantified through μ-CT segmentation. Subsequently, these effective diffusion coefficients for the sedimentary layers of SF-OPA are integrated into the large-scale structural model to facilitate diffusive transport simulations using the Finite Element Method (FEM)-based OpenGeoSys (OGS) simulator (Kolditz et al., 2012; Bilke et al., 2019; Lu et al., 2022).

4.4.2 Methodology

Governing equation of the component transport

In the study, the Component Transport module within the OGS software is employed for the computation of radionuclide migration in SF-OPA. The mass balance equation is formulated as per previous work by Van Loon et al. (2004); Appelo and Wersin (2007); Bear and Bachmat (2012).

$$\frac{\partial (\alpha C)}{\partial t} - \nabla \cdot (\mathbf{D_e} \nabla C) = 0, \tag{4.33}$$

where C (mol m^{-3}) is the concentration of aqueous solute and $\mathbf{D_e}$ (m^2 s^{-1}) is the effective diffusion coefficient tensor. Assuming linear isotherm sorption (Wersin et al., 2008), the constant rock capacity α can be calculated by $\alpha = \phi + \rho_{bd} K_d$ with the porosity ϕ (–), the bulk dry density ρ_{bd} (kg/m^3), and distribution coefficient K_d (m^3/kg).

To determine the effective diffusion coefficient at the field scale, the diffusion equation (Eq. (4.33)) is numerically solved at the pore scale (Yuan et al., 2019; Yuan and Qin, 2020). By imposing constant concentrations at both the inlet and outlet, and no-flux conditions at the remaining boundaries, the effective diffusion coefficient is computed through the total mass flux, denoted as J, per unit cross-sectional area under steady-state conditions, as outlined in Yuan and Fischer (2021):

$$D_e = \frac{J \times L}{C_{in} - C_{out}}, \tag{4.34}$$

where C_{in} and C_{out} are the prescribed concentrations at the inlet and outlet, respectively. L is the length of the domain.

Molecular diffusion

In the context of the diffusion process, the movement of molecules is depicted as a result of molecular random migration when viewed at a microscopic level, and this behavior can be effectively characterized by Brownian motion, as discussed in previous studies (Grathwohl, 1998; Berg, 2018). Since the diffusive spread of molecules follows a Gaussian normal distribution, the effective diffusion coefficient displays a linear correlation with the mean square displacement. This displacement can be calculated using the standard deviation of the molecular distribution, denoted as σ, as detailed in Grathwohl (1998).

$$N(x,t) = \frac{N_0}{2\sqrt{Dt\pi}} \exp\left[-\frac{x^2}{4Dt}\right] \tag{4.35}$$

where, $N(x,t)$ is the number density of molecules at x after time t, N_0 is the total number of molecules.

According to the Gaussian normal distribution, the mean square displacement in a 2D system can be described as a measure for the diffusion distance,

$$\sigma^2 = 2Dt \tag{4.36}$$

In this study, we account for molecules falling within the range of $\pm\sigma$ from the mean position, which encompasses approximately 68% of the total molecules at each diffusion time, as discussed in Yuan and Fischer (2022). Additionally, at the standard deviation σ, the concentration of molecules amounts to 61% of the maximum concentration at each diffusion time, in line with the findings of Grathwohl (1998).

4.4.3 Numerical Simulation Setup

For the field-scale simulation, we have established four representative structural models of SF-OPA, each featuring different subfacies compositions. These conceptual models are visually depicted in Fig. 4.31. Structure 1 (S1) is characterized by a low concentration of carbonate lenses distributed separately within the clay laminae of the shale. In Structure 2 (S2), there is a continuous thin layer of carbonate lenses. Structures 3 (S3) and 4 (S4) exhibit large patches of isolated carbonate lenses, resulting in a higher concentration of carbonate lenses. A detailed breakdown of the subfacies compositions for S1–S4, along with the corresponding effective diffusivities derived from the upscaling workflow, is provided in Table 4.2.

Based on the four distinct types of SF-OPA and the corresponding effective diffusion coefficients obtained at the pore scale, we have developed a simplified 2D geological formation model, as depicted in Fig. 4.32. In this 2D model, we assume the diffusive migration of the Na^+ tracer from a canister (with dimensions:

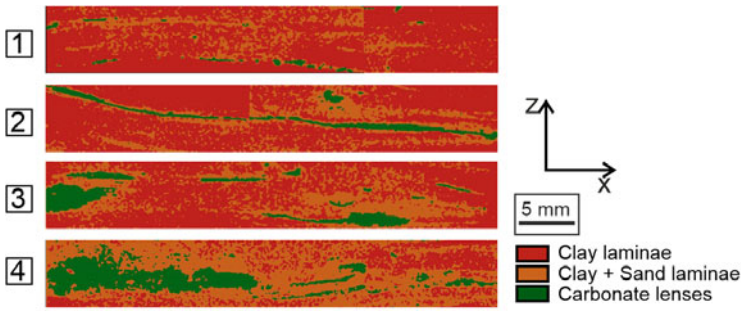

Fig. 4.31 Four SF-OPA structures with distinct subfacies compositions, including cases with low carbonate lens concentration (S1), a single layer (S2), and high carbonate lens concentration (S3 and S4)

Table 4.2 Subfacies compositions and effective diffusivities of four SF-OPA structures

Structure	S1	S2	S3	S4
Clay Laminae composition (%)	78.50	67.60	53.80	25.30
Clay+Sand composition (%)	20.00	26.90	36.40	55.00
Carbonate lenses composition (%)	1.50	5.50	9.80	19.70
Effective diffusivity parallel to bedding direction (x direction in Fig. 4.31) ($\times 10^{-11} m^2/s$)	2.41	1.77	1.28	0.61
Effective diffusivity perpendicular to bedding (z direction in Fig. 4.31) ($\times 10^{-11} m^2/s$)	0.77	0.43	0.43	0.18

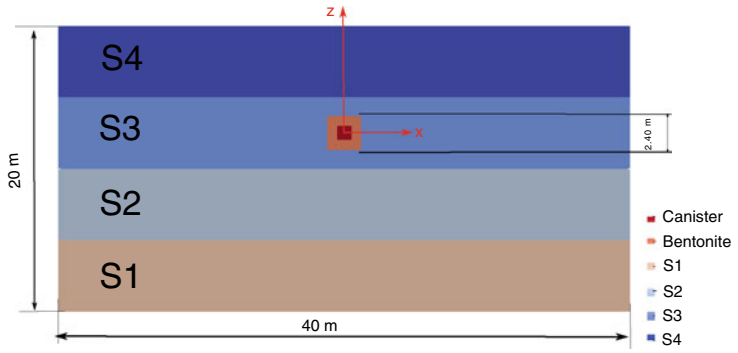

Fig. 4.32 2D structured model of SF-OPA formation with four sedimentary layers (S1–S4) and canister placement in layer S3

length = 1.2 m, width = 1.2 m) into the structured SF-OPA formation (with dimensions: length = 40 m, thickness = 20 m).

Each layer within the formation exhibits a homogeneously distributed structure, mirroring the four structures illustrated in Fig. 4.31. Consequently, every layer features a uniform diffusivity coefficient calculated at the pore scale. In the base case, the canister is placed within layer S3, positioned within a bentonite buffer (with dimensions: length = 2.4 m, width = 2.4 m). This buffer has a known porosity of 0.36 and an effective diffusion coefficient of 2.01×10^{-11} m^2/s, as documented in Nagra (2002). To initiate the simulation, the initial concentration of Na^+ is set at 0.3 mol/L. All boundaries are treated as no-flux conditions, and the total simulation duration spans 2000 years.

In the subsequent sensitivity analysis, we have devised five additional conceptual models, which are enumerated in Table 4.3.

First, in practice, the bedding planes of sedimentary SF-OPA formations at the field scale are typically not oriented perpendicular to the z direction, as established by Leupin et al. (2018). Due to the anisotropic diffusivity properties of SF-OPA, varying bedding angles can exert a considerable influence on the encapsulated effect of radionuclides in the $z+$ direction, as observed from a ground surface perspective. To

Table 4.3 Conceptual model overview

Conceptual model ID	Canister location	Bedding orientation
0	S3	0
1A	S3	30
1B	S3	50
2A	S2	0
2B	S1	0
2C	S4	0

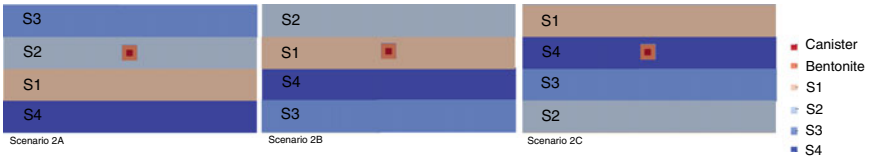

Fig. 4.33 Distribution of SF-OPA layers in conceptual models 2A, 2B, and 2C with canister placement in S2, S1, and S4 layers

explore the impact of these different bedding angles, we have undertaken simulations in Conceptual Model Series #1 (Fig. 4.33).

Second, in the context of radioactive waste disposal within SF-OPA, each sedimentary layer can potentially serve as the site for canister emplacement. The heterogeneity within these layers, where the canister is positioned, leads to distinct effects on radionuclide diffusion. In an effort to investigate and assess the implications of these different heterogeneities, we have emplaced the canister in various layers, as depicted in Fig. 4.34, within Conceptual Model Series #2.

4.4.4 Results and Discussion

Temporal and spatial evolution of heterogeneous diffusion

In Conceptual Model 0 (base case), the highest concentration of sodium (Na^+) in the canister experiences a decrease from 0.071 to 0.055 mol/L between the 1000- and 2000-year marks. The sodium distribution profile along the z direction is visually represented in Fig. 4.34. After 1000 years, sodium has diffused to approximately 5.80 m in the z- direction and about 4.76 m in the z+ direction. This disparity arises because the neighboring layer in the z- direction (S2) possesses a higher diffusivity coefficient compared to the layer in the z+ direction (S4). The difference in sodium concentration distribution is attributed to the heterogeneous layer surrounding the canister.

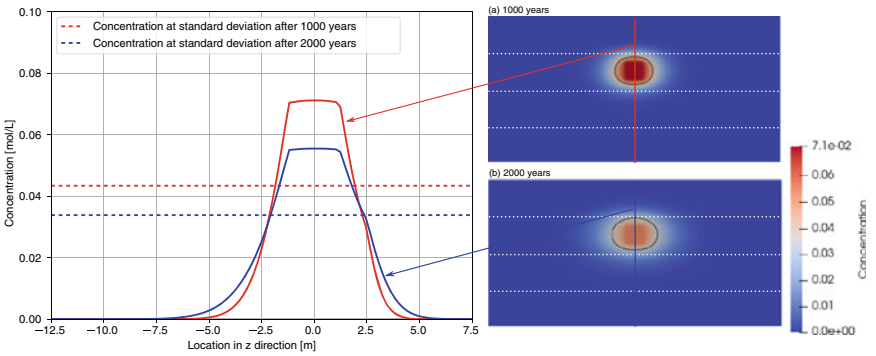

Fig. 4.34 The concentration profiles of Na^+ along the z direction after 1000 years (red line) and 2000 years (blue line) of diffusion. Subsets **a** and **b** provide a detailed view of the concentration distribution across the entire domain after 1000 years and 2000 years of diffusion, respectively. The red line in subset **a** and the blue line in subset **b** are used to facilitate a comparison of concentration profiles along the z direction. Notably, the canister is positioned at the center, located at $z = 0$ m. The white dashed lines delineate the boundaries between different layers, while the black line represents the diffusion front

Examining the diffusion front, which corresponds to the location where sodium concentration equals the standard deviation, it remains within the S3 layer even after 2000 years. Interestingly, the movement of the diffusion front extends further in the $z+$ direction, in contrast to the sodium diffusion's path. Specifically, sodium can migrate an additional 1.04 m in the z- direction. In summary, the movement of the diffusion front is more distant from the canister center in the direction where the neighboring layer possesses a lower diffusivity coefficient. A layer with lower diffusivity coefficient effectively retards the tracer migration in that direction.

The effect of bedding angles

For Conceptual Models 0, 1A, and 1B, where the bedding angle of SF-OPA is set at 0, 30, and 50 degrees, the progression of the diffusion front line in the $z+$ direction is depicted in Fig. 4.35.

It is evident that the diffusion front advances further in the $z+$ direction as the bedding angle increases. After 100 years, with a bedding angle of 0 degrees, the diffusion front is situated at a distance of 1.39 m from the canister center in the $z+$ direction. This distance expands to 1.73 m and 1.81 m when the bedding angle is raised to 30 and 50 degrees, respectively. Remarkably, the locations of the diffusion front line are closely aligned between the two conceptual models with bedding angles of 30 and 50 degrees, with a mere 0.08-meter discrepancy.

Furthermore, it's noteworthy that the diffusion front locations with non-zero bedding angles exceed the distance compared to the model with a bedding angle of 0 degrees. This phenomenon can be attributed to the fact that the diffusion plumes are situated in close proximity to the canister after 100 years, and the influence of

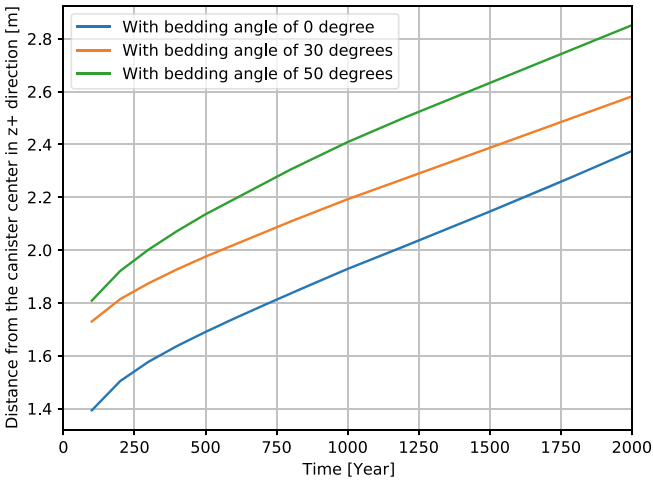

Fig. 4.35 The displacements of diffusion front along $z+$ direction versus diffusion time under bedding angle of 0, 30 and 50 degrees

heterogeneity caused by the neighboring layer is limited. Consequently, the variation in diffusion front displacement is primarily attributed to the anisotropic diffusivity property arising from different bedding angles within the SF-OPA layer.

As the simulation time progresses to 2000 years, a noteworthy change occurs in the sodium diffusion behavior. After 2000 years, the diffusion of sodium notably decelerates due to the influence of the upper neighboring layer S4, especially in the direction perpendicular to the bedding angle. Under these conditions, all diffusion fronts gravitate toward the layer interface in that specific direction.

In the $z+$ direction, the diffusion front is observed to be situated at distances of 2.37, 2.58, and 2.85 m away from the canister center after 2000 years for the conceptual models with bedding angles of 0, 30, and 50 degrees, respectively. The discrepancy between the conceptual models with bedding angles of 30 and 50 degrees amounts to 0.27 m, which is slightly larger (by 0.06 m) compared to the difference between the models with bedding angles of 30 and 0 degrees. This is a consistent trend observed in all three conceptual models, emphasizing the substantial retardation effect exerted by the upper neighboring layer S4 in this specific direction.

The effect of canister emplacement in different layers

The conceptual models 2A, 2B, and 2C have been simulated, and their respective diffusion front displacements are illustrated in Fig. 4.36. After 2000 years, it's noteworthy that in the conceptual models 2A and 2C, the diffusion front remains within the layer where the canister was originally placed. The movement distance is notably smaller than 2.5 m, even falling below 2 m in the case of conceptual model 2C.

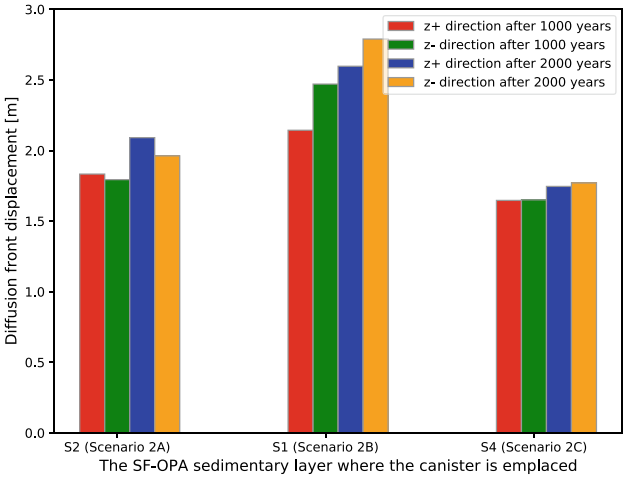

Fig. 4.36 The diffusion front movement in z direction after 1000 and 2000 years, with the canister placement in layers of S2, S1, and S4, respectively

In contrast, for conceptual model 2B, where the canister is located in the S1 layer with the highest diffusivity coefficient, the diffusion front extends to approximately 2.60 m in the z+ direction and 2.79 m in the z- direction. The movement in the z-direction is more pronounced, primarily due to the presence of the neighboring S4 layer, which exhibits the lowest diffusivity coefficient and thereby offers the most effective retardation effect on sodium migration within the 2000-year timespan.

The neighboring layers indeed exert a modest influence on the reshaping of the tracer's diffusion front within a 2000-year timeframe. In the case of conceptual model 2B, where the canister is positioned in the layer featuring the highest diffusivity coefficient, the diffusion front extends an additional 0.19 m further in the vertical downward direction over the course of 2000 years, primarily due to the impact of the neighboring layer. However, it is important to note that the impact of m-scale heterogeneity, despite this effect, remains relatively limited in larger model geometries and longer timespans.

References

Alonso, E., Vaunat, J., & Gens, A. (1999). Modelling the mechanical behaviour of expansive clays. *Engineering geology, 54*(1–2), 173–183.

Alonso, E. E., Alcoverro, J., Coste, F., Malinsky, L., Merrien-Soukatchoff, V., Kadiri, I., Nowak, T., Shao, H., Nguyen, T., Selvadurai, A., et al. (2005). The febex benchmark test: case definition and comparison of modelling approaches. *International Journal of Rock Mechanics and Mining Sciences, 42*(5–6), 611–638.

Appelo, C. A. J., & Wersin, P. (2007). Multicomponent diffusion modeling in clay systems with application to the diffusion of tritium, iodide, and sodium in opalinus clay. *Environmental Science & Technology, 41*(14), 5002–5007.

Bear, J., & Bachmat, Y. (2012). *Introduction to modeling of transport phenomena in porous media*, (vol. 4). Springer Science & Business Media.

Berg, H. C. (2018). Diffusion: microscopic theory. In *Random Walks in Biology* (pp 5–16). Princeton University Press.

Bilke, L., Flemisch, B., Kalbacher, T., Kolditz, O., Helmig, R., & Nagel, T. (2019). Development of open-source porous media simulators: Principles and experiences. *Transport in Porous Media, 130*(1), 337–361.

Blanco-Martín, L., Wolters, R., Rutqvist, J., Lux, K.-H., & Birkholzer, J. T. (2016). Thermal-hydraulic-mechanical modeling of a large-scale heater test to investigate rock salt and crushed salt behavior under repository conditions for heat-generating nuclear waste. *Computers and Geotechnics, 77*, 120–133.

Bollermann, T., Yuan, T., Kulenkampff, J., Stumpf, T., and Fischer, C. (2022). Pore network and flow field analysis towards improved predictability of diffusive transport in argillaceous host rocks. *Chemical Geology*, 606.

BRIUG (2013). Comparison of code-bright and lagamine for thm modeling (d-n^o: Db-wp3), long-term performance of engineered barrier systems.

BRIUG (2014). China-mock-up status annual report (d-n^o: Db-2.4), long-term performance of engineered barrier systems.

Chaudhry, A. A., Buchwald, J., & Nagel, T. (2021). Local and global spatio-temporal sensitivity analysis of thermal consolidation around a point heat source. *International Journal of Rock Mechanics and Mining Sciences, 139*, 104662.

Chen, L., Wang, J., Liu, Y., Collin, F., & Xie, J. (2012). Numerical thermo-hydro-mechanical modeling of compacted bentonite in china-mock-up test for deep geological disposal. *Journal of Rock Mechanics and Geotechnical Engineering, 4*(2), 183–192.

Chen, L., Liu, Y., Wang, J., Cao, S., Xie, J., Ma, L., Zhao, X., Li, Y., & Liu, J. (2014). Investigation of the thermal-hydro-mechanical (thm) behavior of gmz bentonite in the china-mock-up test. *Engineering Geology, 172*, 57–68.

Chen, B., Li, C., Zhang, Y., He, Y., Zhang, F., & Chen, F. (2015). *Experimental study on the unsaturated behavours of gmz bentonite*. Technical Report (in Chinese): Technical report.

Chen, C., Yuan, T., Lu, R., Fischer, C., Kolditz, O., & Shao, H. (2022). The influence of sedimentary heterogeneity on the diffusion of radionuclides in the sandy facies of opalinus clay at the field scale. *Advances in Geosciences, 58*, 77–85.

Collin, F., Li, X.-L., Radu, J.-P., & Charlier, R. (2002). Thermo-hydro-mechanical coupling in clay barriers. *Engineering Geology, 64*(2–3), 179–193.

De Vries, D. (1958). Simultaneous transfer of heat and moisture in porous media. *Eos, Transactions American Geophysical Union, 39*(5), 909–916.

Fredlund, D. G., & Rahardjo, H. (1993). *Soil mechanics for unsaturated soils*. John Wiley & Sons.

Grathwohl, P. (1998). Diffusion in natural porous media: Contaminant transport. *Sorption/Desorption and Dissolution Kinetics*, 207.

Grunwald, N., Lehmann, C., Maßmann, J., Naumov, D., Kolditz, O., & Nagel, T. (2022). Non-isothermal two-phase flow in deformable porous media: systematic open-source implementation and verification procedure. *Geomechanics and Geophysics for Geo-Energy and Geo-Resources, 8*(3), 107.

Harrison, L. P. (1965). Fundamental concepts and definitions relating to humidity. In A. Wexler (Ed.), *Humidity and moisture.* (Vol. 3). New York: Reinhold Publishing Company.

Kolditz, O., Bauer, S., Bilke, L., Böttcher, N., Delfs, J., Fischer, T., Görke, U., Kalbacher, T., Kosakowski, G., McDermott, C., Park, C., Radu, F., Rink, K., Shao, H., Shao, H., Sun, F., Sun, Y., Singh, A., Taron, J., & Zehner, B. (2012). Opengeosys: An open-source initiative for numerical simulation of thermo-hydro-mechanical/chemical (thm/c) processes in porous media. *Environmental Earth Sciences,67*(2), 589–599.

Leupin, O. X., Loon, L. R. V., Gimmi, T., Wersin, P., & Soler, J. M. (2018). Exploring diffusion and sorption processes at the mont terri rock laboratory (switzerland): lessons learned from 20 years of field research. In *Mont Terri Rock Laboratory, 20 Years* (pp. 393–405). Springer.

Liu, Y., Ma, L., Ke, D., Cao, S., Xie, J., Zhao, X., Chen, L., & Zhang, P. (2014). Design and validation of the thmc china-mock-up test on buffer material for hlw disposal. *Journal of Rock Mechanics and Geotechnical Engineering, 6*(2), 119–125.

Lu, R., Nagel, T., Poonoosamy, J., Naumov, D., Fischer, T., Montoya, V., Kolditz, O., & Shao, H. (2022). A new operator-splitting finite element scheme for reactive transport modeling in saturated porous media. *Computers & Geosciences, 163*, 105106.

Nagra (2002). Demonstration of disposal feasibility for spent fuel, vitrified high-level waste and long-lived intermediate-level waste (entsorgungsnachweis).

Nguyen, S., Lanru, J., Boergesson, L., Chijimatzu, M., Jussila, P., & Rutqvist, J. (2007). Decovalex-thmc project. task a. influence of near field coupled thm phenomena on the performance of a spent fuel repository. report of task a1: Preliminary scoping calculations. Technical report, Report of Task A2, Swedish Nuclear Power Inspectorate.

Parkhurst, D. L., Appelo, C., et al. (2013). Description of input and examples for phreeqc version 3-a computer program for speciation, batch-reaction, one-dimensional transport, and inverse geochemical calculations. *US Geological Survey Techniques and Methods, 6*(A43), 497.

Philip, J., & De Vries, D. (1957). Moisture movement in porous materials under temperature gradients. *Eos, Transactions American Geophysical Union, 38*(2), 222–232.

Philip, J., & De Vries, D. (1957). Moisture movement in porous materials under temperature gradients. *Eos, Transactions American Geophysical Union, 38*(2), 222–232.

Pitz, M., Kaiser, S., Grunwald, N., Kumar, V., Buchwald, J., Wang, W., Naumov, D., Chaudhry, A. A., Maßmann, J., Thiedau, J., Kolditz, O., and Nagel, T. (2022). Non-isothermal consolidation: A systematic evaluation of two implementations based on multiphase and richards equations [manuscript submitted for publication]. *International Journal of Rock Mechanics and Mining Sciences*.

Richards, L. A. (1931). Capillary conduction of liquids through porous mediums. *Physics, 1*(5), 318–333.

Rutqvist, J., Ijiri, Y., & Yamamoto, H. (2011). Implementation of the barcelona basic model into tough-flac for simulations of the geomechanical behavior of unsaturated soils. *Computers & Geosciences, 37*(6), 751–762.

Saito, H., Simunek, J. J., & Mohanty, B. (2006). Numerical analysis of coupled water, vapor and heat transport in the vadose zone. *Vadose Zone Journal, 5*, 784–800.

Van Loon, L. R., Wersin, P., Soler, J., Eikenberg, J., Gimmi, T., Hernan, P., Dewonck, S., & Savoye, S. (2004). In-situ diffusion of HTO, $^{22}Na^{+}$, Cs^{+} and I^{-} in Opalinus Clay at the Mont Terri underground rock laboratory. *Radiochimica Acta, 92*(9–11), 757–763.

Wang, J. (2010). High-level radioactive waste disposal in china: update 2010. *Journal of Rock Mechanics and Geotechnical Engineering, 2*(1), 1–11.

Wang, W., Rutqvist, J., Görke, U.-J., Birkholzer, J. T., & Kolditz, O. (2010). Non-isothermal flow in low permeable porous media: A comparison of richards' and two-phase flow approaches. *Environmental Earth Sciences, 62*, 1197–1207.

Wersin, P., Soler, J., Van Loon, L., Eikenberg, J., Baeyens, B., Grolimund, D., Gimmi, T., & Dewonck, S. (2008). Diffusion of HTO, Br^{-}, I^{-}, Cs^{+}, $^{85}Sr^{2+}$ and $^{60}Co^{2+}$ in a clay formation: Results and modelling from an in situ experiment in Opalinus Clay. *Applied Geochemistry, 23*(4), 678–691.

Yuan, T., & Fischer, C. (2022). The influence of sedimentary and diagenetic heterogeneity on the radionuclide diffusion in the sandy facies of the opalinus clay at the core scale. *Applied Geochemistry*.

Yuan, T. and Qin, G. (2020). Numerical investigation of wormhole formation during matrix acidizing of carbonate rocks by coupling stokes-brinkman equation with reactive transport model under radial flow conditions. In *SPE International Conference and Exhibition on Formation Damage Control*. OnePetro.

Yuan, T., & Fischer, C. (2021). Effective diffusivity prediction of radionuclides in clay formations using an integrated upscaling workflow. *Transport in Porous Media, 138*(2), 245–264.

Yuan, T., Wei, C., Zhang, C.-S., & Qin, G. (2019). A numerical simulator for modeling the coupling processes of subsurface fluid flow and reactive transport processes in fractured carbonate rocks. *Water, 11*(10), 1957.

Zhao, J., Chen, L., Collin, F., Liu, Y., & Wang, J. (2016). Numerical modeling of coupled thermal-hydro-mechanical behavior of gmz bentonite in the china-mock-up test. *Engineering Geology, 214*, 116–126.

Chapter 5
Synthesis and Outlook

Haibing Shao, Ju Wang, Thorsten Schäfer, Chun-Liang Zhang, Horst Geckeis, Thomas Nagel, Uwe Düsterloh, Olaf Kolditz, and Hua Shao

This book provides a comprehensive overview of Chinese activities to establish a new underground laboratory for repository research. The URL project in the Chinese province of Gansu started in 2015 with several potentially suitable sites in crystalline and clay rock. The Beishan site has proven to be the most suitable location for the

H. Shao (✉) · O. Kolditz
Helmholtz Centre for Environmental Research UFZ, 04318 Leipzig, Germany
e-mail: haibing.shao@ufz.de

J. Wang
Beishan Underground Research Laboratory for HLW Disposal, Beijing Research Institute of Uranium Geology, Beijing 100029, China

T. Schäfer
Friedrich-Schiller-University Jena, Institute of Geosciences, Applied Geology, 07749 Jena, Germany

C.-L. Zhang
Gesellschaft für Anlagen- und Reaktorsicherheit (GRS) gGmbH, 38122 Braunschweig, Germany

H. Geckeis
Karlsruhe Institute of Technology, Institute for Nuclear Waste Disposal (INE), 76094 Karlsruhe, Germany

T. Nagel
Technische Universität Bergakademie Freiberg, Geological Institute, 09599 Freiberg, Germany

U. Düsterloh
Clausthal University of Technology, Geomechanics and Multiphysical Systems, 38678 Clausthal-Zellerfeld, Germany

H. Shao
Federal Institute for Geosciences and Natural Resources (BGR), 30655 Hanover, Germany

H. Shao et al. (eds.), *Thermo-Hydro-Mechanical-Chemical (THMC) Processes in Bentonite Barrier Systems*, Terrestrial Environmental Sciences,
https://doi.org/10.1007/978-3-031-53204-7_5

construction of the underground research laboratory. A tunnel boring machine (TBM) was specially designed and constructed for the excavation of the URL tunnel. The start-up of the laboratory is planned in four years for 2027 (see Sect. 2.1).

In addition to the host rock, the geotechnical barrier plays an important role in the concept for the final disposal of radioactive waste. The so-called Gaomiaozi (GMZ) bentonite, which is available in sufficient quantities in China, is intended for this purpose. In order to investigate the thermo-hydro-mechanical-chemical (THMC) processes acting on the GMZ, a corresponding long-term laboratory experiment was carried out (GMZ Mock-Up Test) (see Chap. 2). The data from the large-scale laboratory experiment are available for process studies. To evaluate the data, the modelling teams from BRIUG, TU Clausthal and TU Freiberg joined forces and interpreted the measurement results with different models (see Chap. 4). The results are also to be published in a joint publication. Transport processes in the far field of a deep geological repository were investigated by the UFZ. This primarily involved the influence of heterogeneities in the aquifers of the framework rock. As part of the pilot project, the experimental database on the GMZ bentonite was further completed. Geomechanical, mineralogical and geochemical investigations were carried out in the laboratories of BGR, GRS, Jena University and KIT (Chap. 3). For this purpose, BRIUG provided corresponding samples of the GMZ bentonite. The results of the project have contributed both to the experimental basis and to a better understanding of the complex THMC processes in the geotechnical barrier (GZM bentonite). In addition, the cooperation between the Chinese and German scientists could be further deepened, despite the difficult conditions caused by the Corona pandemic.

With the site selection act (2014/2017) and the final report of the commission 'Deposition of highly radioactive waste' (2016), Germany faces the challenge of the comparative site search in the different types of host rocks: salt, clay and crystalline formations. In Germany, there is an excellent level of knowledge regarding salt rock, an advanced status with regard to clay/clay stone, but only few insights into crystalline formations, so there is a special need for research and cooperation here. The teaching and research underground laboratory 'Reiche Zeche' operated by TU Freiberg covers broad aspects of mining research. Since Germany does not have its own dedicated underground laboratory (URL) for repository studies in crystalline rock, individual aspects of long-term safety in granite formations have been investigated in cooperation with the Swiss NAGRA[1] (Grimsel Rock Laboratory) and the Swedish SKB[2] (Hard Rock Laboratory Äspö). However, these studies do not comply requirements of the above-mentioned legal acts, and they are not transferable (e.g. unlike in Germany, in Sweden no higher and longer heat-generating mixed-oxide (MOX) fuel elements are stored). China's decision to establish a new URL in Beishan (Gansu Province) offers a unique opportunity to obtain data in its original state in an undisturbed crystalline formation (with regionally higher than average geothermal gradients). The new URL in Beishan is welcomed in the network of established URLs in crystalline rocks (Fig. 5.1) and shall play an important role also

[1] Nationale Genossenschaft für die Lagerung radioaktiver Abfälle.

[2] Swedish Nuclear Fuel and Waste Management Company.

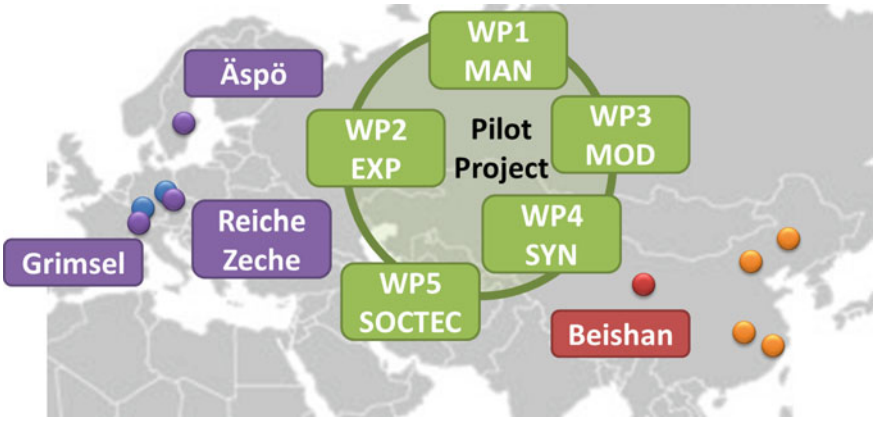

Fig. 5.1 Network of URLs in crystalline rock environments

for international research in future—as a place of international collaboration in order to improve the knowledge base for safe deep geological deposition of radioactive waste in the subsurface.

Bibliography

Ahn, J., & Apted, M. (2010). *Geological repository systems for safe disposal of spent nuclear fuels and radioactive waste*. Cambridge, UK: Woodhead Publishing Limited.

Alonso, E., Alcoverro, J., Coste, F., Malinsky, L., Merrien-Soukatchoff, V., Kadiri, I., Nowak, T., Shao, H., Nguyen, T., Selvadurai, A., Armand, G., Sobolik, S., Itamura, M., Stone, C., Webb, S., Rejeb, A., Tijani, M., Maouche, Z., Kobayashi, A., Kurikami, H., Ito, A., Sugita, Y., Chijimatsu, M., Börgesson, L., Hernelind, J., Rutqvist, J., Tsang, C.-F., and Jussila, P. (2005a). The febex benchmark test: Case definition and comparison of modelling approaches. *International Journal of Rock Mechanics and Mining Sciences, 42*(5), 611–638. Research results from the Decovalex III & Benchpar projects.

Alonso, E. E., Alcoverro, J., Coste, F., Malinsky, L., Merrien-Soukatchoff, V., Kadiri, I., Nowak, T., Shao, H., Nguyen, T., Selvadurai, A., et al. (2005b). The febex benchmark test: Case definition and comparison of modelling approaches. *International Journal of Rock Mechanics and Mining Sciences,42*(5–6), 611–638.

Alonso, E., Vaunat, J., & Gens, A. (1999). Modelling the mechanical behaviour of expansive clays. *Engineering Geology, 54*(1–2), 173–183.

Appelo, C. A. J., & Wersin, P. (2007). Multicomponent diffusion modeling in clay systems with application to the diffusion of tritium, iodide, and sodium in opalinus clay. *Environmental Science & Technology, 41*(14), 5002–5007.

Bear, J., & Bachmat, Y. (2012). *Introduction to modeling of transport phenomena in porous media* (Vol. 4). Springer.

Berg, H. C. (2018). Diffusion: Microscopic theory. In *Random walks in biology* (pp. 5–16). Princeton University Press.

Bergmann, J., & Kleeberg, R. (1998). Rietveld analysis of disordered layer silicates. *Materials Science Forum, 278–281*(PART 1), 300–305. Cited by: 59.

Bilke, L., Flemisch, B., Kalbacher, T., Kolditz, O., Helmig, R., & Nagel, T. (2019). Development of open-source porous media simulators: Principles and experiences. *Transport in Porous Media, 130*(1), 337–361.

Birgersson, M., Hedström, M., Karnland, O., & Sjöland, A. (2017). Bentonite buffer: Macroscopic performance from nanoscale properties. In *Geological repository systems for safe disposal of spent nuclear fuels and radioactive waste* (pp. 319–364). Elsevier.

Blanco-Martín, L., Wolters, R., Rutqvist, J., Lux, K.-H., & Birkholzer, J. T. (2016). Thermal-hydraulic-mechanical modeling of a large-scale heater test to investigate rock salt and crushed salt behavior under repository conditions for heat-generating nuclear waste. *Computers and Geotechnics, 77*, 120–133.

H. Shao et al. (eds.), *Thermo-Hydro-Mechanical-Chemical (THMC) Processes in Bentonite Barrier Systems*, Terrestrial Environmental Sciences,
https://doi.org/10.1007/978-3-031-53204-7

Bollermann, T., Yuan, T., Kulenkampff, J., Stumpf, T., & Fischer, C. (2022). Pore network and flow field analysis towards improved predictability of diffusive transport in argillaceous host rocks. *Chemical Geology, 606*.

Bouby, M., Kraft, S., Kuschel, S., Geyer, F., Moisei-Rabung, S., Schäfer, T., & Geckeis, H. (2020). Erosion dynamics of compacted raw or homoionic mx80 bentonite in a low ionic strength synthetic water under quasi-stagnant flow conditions. *Applied Clay Science, 198*, 105797.

Bradbury, M. H., & Baeyens, B. (2002a). A comparison of apparent diffusion coefficients measured in compacted kunigel v1 bentonite with those calculated from batch sorption measurements and d e (hto) data: A case study for cs (i), ni (ii), sm (iii), am (iii), zr (iv) and np (v). Technical report, NAGRA Technical Report, NTB 02-17.

Bradbury, M. H., & Baeyens, B. (2002b). Porewater chemistry in compacted re-saturated mx-80 bentonite: Physico-chemical characterisation and geochemical modelling. Technical report, PSI Bericht Nr. 02-10, ISSN 1019-0643.

Brandt, F., & Bosbach, D. (2001). Bassanite (caso4· 0.5 h2o) dissolution and gypsum (caso4· 2h2o) precipitation in the presence of cellulose ethers. *Journal of Crystal Growth, 233*(4), 837–845.

BRIUG. (2013). Comparison of code-bright and lagamine for thm modeling (d-n^o: Db-wp3), long-term performance of engineered barrier systems.

BRIUG. (2014). China-mock-up status annual report (d-n^o: Db-2.4), long-term performance of engineered barrier systems.

Bucher, F., & Müller-Vonmoos, M. (1989). Bentonite as a containment barrier for the disposal of highly radioactive wastes. *Applied Clay Science, 4*(2), 157–177.

(CAEA), C. A. E. A. (2006). R&d guidelines for the geological disposal of high-level radioactive waste in china. Technical report, CAEA, Beijing, China.

CASEA. (2013). Datasheet alpha agr 40. *99755 Ellrich, Germany, CASEA GmbH, REMONDIS-Group.*

Chaparro, M. C., Finck, N., Metz, V., & Geckeis, H. (2021). Reactive transport modelling of the long-term interaction between carbon steel and mx-80 bentonite at 25° c. *Minerals, 11*(11), 1272.

Chaudhry, A. A., Buchwald, J., & Nagel, T. (2021). Local and global spatio-temporal sensitivity analysis of thermal consolidation around a point heat source. *International Journal of Rock Mechanics and Mining Sciences, 139*, 104662.

Chen, B., Li, C., Zhang, Y., He, Y., Zhang, F., & Chen, F. (2015). Experimental study on the unsaturated behavours of gmz bentonite. Technical report, Technical Report (in Chinese).

Chen, B., Chen, J. Q., & Cao, Y. C. (2012a). Influence of joint on self-sealing behavior of highly compacted bentonite in engineering barrier. *Chinese Journal of Rock Mechanics and Engineering,31*(3), 618–624.

Chen, L., Wang, J., Liu, Y., Collin, F., & Xie, J. (2012b). Numerical thermo-hydro-mechanical modeling of compacted bentonite in china-mock-up test for deep geological disposal. *Journal of Rock Mechanics and Geotechnical Engineering,4*(2), 183–192.

Chen, L., Liu, Y., Wang, J., Cao, S., Xie, J., Ma, L., Zhao, X., Li, Y., & Liu, J. (2014). Investigation of the thermal-hydro-mechanical (thm) behavior of gmz bentonite in the china-mock-up test. *Engineering Geology, 172*, 57–68.

Chen, B., Qian, L., Ye, W., Cui, Y. J., & Wang, J. (2006). Soil-water characteristic curves of gaomiaozi bentonite. *Chinese Journal of Rock Mechanics and Engineering, 25*(4), 1054–1058.

Chen, C., Yuan, T., Lu, R., Fischer, C., Kolditz, O., & Shao, H. (2022). The influence of sedimentary heterogeneity on the diffusion of radionuclides in the sandy facies of opalinus clay at the field scale. *Advances in Geosciences, 58*, 77–85.

Collin, F., Li, X.-L., Radu, J.-P., & Charlier, R. (2002). Thermo-hydro-mechanical coupling in clay barriers. *Engineering Geology, 64*(2–3), 179–193.

Cui, Y., Tang, A., Qian, L., Ye, W., & Chen, B. (2011). Thermal-mechanical behavior of compacted gmz bentonite. *Soils and Foundations, 51*(6), 1065–1074.

Cui, L.-Y., Ye, W.-M., Wang, Q., Chen, Y.-G., Chen, B., & Cui, Y.-J. (2021). Insights into gas migration behavior in saturated gmz bentonite under flexible constraint conditions. *Construction and Building Materials, 287*, 123070.

Cuss, R., Harrington, J., Noy, D., Graham, C., & Sellin, P. (2014). Evidence of localised gas propagation pathways in a field-scale bentonite engineered barrier system; results from three gas injection tests in the large scale gas injection test (lasgit). *Applied Clay Science, 102*, 81–92.

De Vries, D. (1958). Simultaneous transfer of heat and moisture in porous media. *Eos, Transactions American Geophysical Union, 39*(5), 909–916.

Dohrmann, R., Genske, D., Karnland, O., Kaufhold, S., Kiviranta, L., Olsson, S., Plötze, M., Sandén, T., Sellin, P., Svensson, D., et al. (2012). Interlaboratory cec and exchangeable cation study of bentonite buffer materials: I. cu (ii)-triethylenetetramine method. *Clays and Clay Minerals, 60*(2), 162–175.

Duda, R., Rejl, L., & Slivka, D. (1990). Minerals (in czech). *Aventinum*, Prague, from https://www.mindat.org/loc-7944.html.

Ebner, A. D., Ritter, J. A., & Navratil, J. D. (2001). Adsorption of cesium, strontium, and cobalt ions on magnetite and a magnetite- silica composite. *Industrial & Engineering Chemistry Research, 40*(7), 1615–1623.

Féron, D., Crusset, D., & Gras, J. M. (2009). Corrosion issues in the French high-level nuclear waste program. *Corrosion, 65*(3), 213–223.

Fredlund, D. G., & Rahardjo, H. (1993). *Soil mechanics for unsaturated soils*. Wiley.

García-García, S., Wold, S., & Jonsson, M. (2007). Kinetic determination of critical coagulation concentrations for sodium-and calcium-montmorillonite colloids in nacl and cacl2 aqueous solutions. *Journal of Colloid and Interface Science, 315*(2), 512–519.

Graham, C. C., Harrington, J. F., & Sellin, P. (2016). Gas migration in pre-compacted bentonite under elevated pore-water pressure conditions. *Applied Clay Science, 132*, 353–365.

Grathwohl, P. (1998). Diffusion in natural porous media: Contaminant transport. *Sorption/Desorption and Dissolution Kinetics, 207*.

Grunwald, N., Lehmann, C., Maßmann, J., Naumov, D., Kolditz, O., & Nagel, T. (2022). Non-isothermal two-phase flow in deformable porous media: Systematic open-source implementation and verification procedure. *Geomechanics and Geophysics for Geo-Energy and Geo-Resources, 8*(3), 107.

Gutiérrez-Rodrigo, V., Martín, P. L., & Villar, M. V. (2021). Effect of interfaces on gas breakthrough pressure in compacted bentonite used as engineered barrier for radioactive waste disposal. *Process Safety and Environmental Protection, 149*, 244–257.

Harrington, J. F., Graham, C. C., Cuss, R. J., & Norris, S. (2017). Gas network development in a precompacted bentonite experiment: Evidence of generation and evolution. *Applied Clay Science, 147*, 80–89.

Harrison, L. P. (1965). Fundamental concepts and definitions relating to humidity. In A. Wexler (Ed.), *Humidity and moisture.* (Vol. 3). New York: Reinhold Publishing Company.

HPF. (2015). Sikron® quarz - stoffdaten. *H.-T. M. E. Q. G. Frechen*

IAEA. (2013). Characterization of swelling clays as components of the engineered barrier system for geological repositories. *IAEA-TECDOC-1718. Vienna, International Atomic Energy Agency.*

Imbert, C., & Villar, M. (2006). Hydro-mechanical response of a bentonite pellets/powder mixture upon infiltration. *Applied Clay Science, 32*(3–4), 197–209. cited By 123.

Jenni, A., Wersin, P., Mäder, U., Gimmi, T., Thoenen, T., Baeyens, B., Hummel, W., Ferrari, A., Marschall, P., & Leupin, O. (2019). Bentonite backfill performance in a high-level waste repository: A geochemical perspective. Technical report, University of Berne.

Ju, W., Liang, C., Rui, S., & Xingguang, Z. (2018). The Beishan underground research laboratory for geological disposal of high-level radioactive waste in China: Planning, site selection, site characterization and in situ tests. *Journal of Rock Mechanics and Geotechnical Engineering, 10*(3), 411–435.

Kahr, G., Meier, L., Wolf, D., Starke, R., & Kleeberg, R. (1996). Einfache bestimmungsmethode des kationenaustauschvermögens von tonen mit komplexverbindungen des kupfer (ii)-ions mit triethylentetramin und tetraethylenpentamin. *Berichte der DTTG* (pp. 122–126).

Karnland, O., Nilsson, U., Weber, H., & Wersin, P. (2008). Sealing ability of wyoming bentonite pellets foreseen as buffer material-laboratory results. *Physics and Chemistry of the Earth, Parts A/B/C, 33*, S472–S475.

Kaufhold, S., Dohrmann, R., Ufer, K., & Meyer, F. (2002). Comparison of methods for the quantification of montmorillonite in bentonites. *Applied Clay Science, 22*(3), 145–151. Cited by: 77.

Kaufhold, S., Hein, M., Dohrmann, R., & Ufer, K. (2012). Quantification of the mineralogical composition of clays using ftir spectroscopy. *Vibrational Spectroscopy, 59*, 29–39. Cited by: 69.

Kaufhold, S., Kremleva, A., Krüger, S., Rösch, N., Emmerich, K., & Dohrmann, R. (2017). Crystal-chemical composition of dicoctahedral smectites: An energy-based assessment of empirical relations. *ACS Earth and Space Chemistry, 1*(10), 629–636. Cited by: 6.

Kaufhold, S., Dohrmann, R., & Klinkenberg, M. (2010). Water-uptake capacity of bentonites. *Clays and Clay Minerals, 58*(1), 37–43.

Kaufhold, S., Schippers, A., Marx, A., & Dohrmann, R. (2020). Sem study of the early stages of fe-bentonite corrosion-the role of naturally present reactive silica. *Corrosion Science, 171*, 108716.

Kiviranta, L., & Kumpulainen, S. (2011). Quality control and characterization of bentonite materials. Technical report, Posiva Oy. Working Report 2011-84.

Kolditz, O., Bauer, S., Bilke, L., Böttcher, N., Delfs, J., Fischer, T., Görke, U., Kalbacher, T., Kosakowski, G., McDermott, C., Park, C., Radu, F., Rink, K., Shao, H., Shao, H., Sun, F., Sun, Y., Singh, A., Taron, J., Walther, M., Wang, W., Watanabe, N., Wu, Y., Xie, M., Xu, W., & Zehner, B. (2012). Opengeosys: An open-source initiative for numerical simulation of thermo-hydro-mechanical/chemical (thm/c) processes in porous media. *Environmental Earth Sciences,67*(2), 589–599.

Leupin, O. X., Loon, L. R. V., Gimmi, T., Wersin, P., & Soler, J. M. (2018). Exploring diffusion and sorption processes at the mont terri rock laboratory (Switzerland): Lessons learned from 20 years of field research. In *Mont Terri Rock Laboratory, 20 Years* (pp. 393–405). Springer.

Levasseur, S., Collin, F., Daniels, K., Dymitrowska, M., Harrington, J., Jacops, E., Kolditz, O., Marschall, P., Norris, S., Sillen, X., Talandier, J., Truche, L., & Wendling, J. (2020). Initial state of the art on gas transport in clayey materials. Technical report, Final version as of 30.11.2020 of deliverable D6.1 of the HORIZON 2020 project EURAD. EC Grant agreement no: 847593.

Liu, H.-H. (2017). *Fluid flow in the subsurface*. Springer.

Liu, Y. M., Wang, J., Cao, S. F., Ma, L. K., Xie, J. L., Zhao, X. G., & Chen, L. (2013). A large-scale thmc experiment of buffer material for geological disposal of high level radioactive waste in China. *Rock and Soil Mechanics,34*(10), 2756–2762.

Liu, Y., & Cai, M. (2007). Thermal conductivity of buffer material for high-level waste disposal (in Chinese). *Chinese Journal of Rock Mechanics and Engineering, 26*(S2), 3891–3896.

Liu, Y., Cai, M., & Wang, J. (2007). Compressibility of buffer material for hlw disposal in china (in Chinese). *Uranium Geology, 23*, 91–95.

Liu, Y., Ma, L., Ke, D., Cao, S., Xie, J., Zhao, X., Chen, L., & Zhang, P. (2014). Design and validation of the thmc china-mock-up test on buffer material for hlw disposal. *Journal of Rock Mechanics and Geotechnical Engineering, 6*(2), 119–125.

Liu, Y., & Wen, Z. (2003). Study on clay-based materials for the repository of high level radioactive waste (in Chinese). *Journal of Mineralogy and Petrology, 23*(4), 42–45.

Lorenz, P., Meier, L., & Kahr, G. (1999). Determination of the cation exchange capacity (cec) of clay minerals using the complexes of copper (ii) ion with triethylenetetramine and tetraethylenepentamine. *Clays and Clay Minerals, 47*(3), 386–388.

Lu, R., Nagel, T., Poonoosamy, J., Naumov, D., Fischer, T., Montoya, V., Kolditz, O., & Shao, H. (2022). A new operator-splitting finite element scheme for reactive transport modeling in saturated porous media. *Computers & Geosciences, 163*, 105106.

Martín, P., & Barcala, J. (2005). Large scale buffer material test: Mock-up experiment at ciemat. *Engineering Geology, 81*(3), 298–316. Issues in Nuclear Waste Isolation Research.

Ma, H., Wang, J., Man, K., Chen, L., & Gong, Q. (2020). Excavation of underground research laboratory ramp in granite using tunnel boring machine: Feasibility study. *Journal of Rock Mechanics and Geotechnical Engineering, 12*(6), 1201–1213.

Mehrabi, K., Nowack, B., Arroyo Rojas Dasilva, Y., & Mitrano, D. M. (2017). Improvements in nanoparticle tracking analysis to measure particle aggregation and mass distribution: A case study on engineered nanomaterial stability in incineration landfill leachates. *Environmental science & technology,51*(10), 5611–5621.

Missana, T., Garcı, M., et al. (2007). Adsorption of bivalent ions (ca (ii), sr (ii) and co (ii)) onto febex bentonite. *Physics and Chemistry of the Earth, Parts A/B/C, 32*(8–14), 559–567.

Molera, M., & Eriksen, T. (2002). Diffusion of 22na+, 85sr2+, 134cs+ and 57co2+ in bentonite clay compacted to different densities: Experiments and modeling. *Radiochimica Acta, 90*(9–11), 753–760.

Müller, H. R., Garitte, B., Vogt, T., Köhler, S., Sakaki, T., Weber, H., Spillmann, T., Hertrich, M., Becker, J. K., Giroud, N., et al. (2018). Implementation of the full-scale emplacement (fe) experiment at the mont terri rock laboratory. *Mont Terri Rock Laboratory, 20 Years: Two Decades of Research and Experimentation on Claystones for Geological Disposal of Radioactive Waste* (pp. 289–308).

Muurinen, A., Pentilla-Hiltunen, P., Rantanen, J., & Uusheimo, K. (1987). Diffusion of uranium and chloride in compacted na bentonite. In *Technical Report YJT-87-14*. Nuclear waste Commission of Finnish Power Companies Helsinki, Finland.

Nagra. (2002). Demonstration of disposal feasibility for spent fuel, vitrified high-level waste and long-lived intermediate-level waste (entsorgungsnachweis).

Nguyen, S., Lanru, J., Boergesson, L., Chijimatzu, M., Jussila, P., & Rutqvist, J. (2007). Decovalex-thmc project. task a. influence of near field coupled thm phenomena on the performance of a spent fuel repository. report of task a1: Preliminary scoping calculations. Technical report, Report of Task A2, Swedish Nuclear Power Inspectorate.

Parkhurst, D. L., Appelo, C., et al. (2013). Description of input and examples for phreeqc version 3-a computer program for speciation, batch-reaction, one-dimensional transport, and inverse geochemical calculations. *US Geological Survey Techniques and Methods, 6*(A43), 497.

Philip, J., & De Vries, D. (1957a). Moisture movement in porous materials under temperature gradients. *Eos, Transactions American Geophysical Union,38*(2), 222–232.

Philip, J., & De Vries, D. (1957b). Moisture movement in porous materials under temperature gradients. *Eos, Transactions American Geophysical Union,38*(2), 222–232.

Pitz, M., Kaiser, S., Grunwald, N., Kumar, V., Buchwald, J., Wang, W., Naumov, D., Chaudhry, A. A., Maßmann, J., Thiedau, J., Kolditz, O., & Nagel, T. (2022). Non-isothermal consolidation: A systematic evaluation of two implementations based on multiphase and Richards equations [manuscript submitted for publication]. *International Journal of Rock Mechanics and Mining Sciences*.

Pospiskova, I., Dobrev, D., Kouril, M., Stoulil, J., Novikova, D., Kotnour, P., & Matal, O. (2017). Czech national programme and disposal canister concept. *Corrosion Engineering, Science and Technology, 52*(sup1), 6–10.

Pusch, R., Hökmark, H., & Börgesson, L. (1987). Outline of models of water and gas flow through smectite clay buffers. Technical report, SKB Technical Report 87-10, Stockholm, Sweden.

Pusch, R., Karnland, O., & Hökmark, H. (1990). Gmm-a general microstructural model for qualitative and quantitative studies of smectite clays. Technical report, SKB Technical Report 90-43, Stockholm, Sweden.

Richards, L. A. (1931). Capillary conduction of liquids through porous mediums. *Physics, 1*(5), 318–333.

Rutqvist, J., Ijiri, Y., & Yamamoto, H. (2011). Implementation of the barcelona basic model into tough-flac for simulations of the geomechanical behavior of unsaturated soils. *Computers & Geosciences, 37*(6), 751–762.

Saito, H., Simunek, J. J., & Mohanty, B. (2006). Numerical analysis of coupled water, vapor and heat transport in the vadose zone. *Vadose Zone Journal, 5*, 784–800.

Schäfer, T., Geckeis, H., Bouby, M., & Fanghänel, T. (2004). U, th, eu and colloid mobility in a granite fracture under near-natural flow conditions. *Radiochimica Acta, 92*(9–11), 731–737.

Schwertmann, U., & Cornell, R. M. (2000). *Iron oxides in the laboratory: Preparation and characterization*. WILEY-VCH, Weinheim, Berlin: Wiley.

Seher, H., Geckeis, H., Fanghänel, T., & Schäfer, T. (2020). Bentonite nanoparticle stability and the effect of fulvic acids: Experiments and modelling. *Colloids and Interfaces, 4*(2), 16.

Seiphoori, A. (2015). *Thermo-hydro-mechanical characterisation and modelling of Wyoming granular bentonite*. Switzerland: Nagra Wettingen.

Sellin, P. (2014). Experiments and modelling on the behaviour of ebs. *FORGE Reprot D, 3*, 38.

SKB. (2011). Long-term safety for the final repository for spent nuclear fuel at forsmark. *Main report of the SR-Site project, Volume I, Technical Report, TR-11-01*. AB, Svensk Kärnbränslehantering.

Svensson, D., Dueck, A., Nilsson, U., Olsson, S., Sanden, T., Lydmark, S., Jaegerwall, S., Pedersen, K., & Hansen, S. (2011). Alternative buffer material. Status of the ongoing laboratory investigation of reference materials and test package 1. *AB, Svensk Kärnbränslehantering*.

Ufer, K., Roth, G., Kleeberg, R., Stanjek, H., Dohrmann, R., & Bergmann, J. (2004). Description of x-ray powder pattern of turbostratically disordered layer structures with a rietveld compatible approach. *Zeitschrift fur Kristallographie, 219*(9), 519–527. Cited by: 129.

Van Loon, L. R., Wersin, P., Soler, J., Eikenberg, J., Gimmi, T., Hernan, P., Dewonck, S., & Savoye, S. (2004). In-situ diffusion of HTO, $^{22}Na^{+}$, Cs^{+} and I^{-} in Opalinus Clay at the Mont Terri underground rock laboratory. *Radiochimica Acta,92*(9–11), 757–763.

Van Loon, L. R., & Müller, W. (2014). A modified version of the combined in-diffusion/abrasive peeling technique for measuring diffusion of strongly sorbing radionuclides in argillaceous rocks: A test study on the diffusion of caesium in opalinus clay. *Applied Radiation and Isotopes, 90*, 197–202.

Van Loon, L. R., & Soler, J. M. (2004). Diffusion of hto, 36 cl-, 125 i-and 22 na+ in opalinus clay: Effect of confining pressure, sample orientation, sample depth and temperature. Technical report, PSI Bericht Nr. 04-03, February 2004.

Villar, M., Armand, G., Conil, N., de Lesquen, C., Herold, P., Simo, E., Mayor, J., Dizier, A., Li, X., Chen, G., Leupin, O., Niskanen, M., Bailey, M., Thompson, S., Svensson, D., Sellin, P., & Hausmannova, L. (2020). Initial state-of-the-art on thm behaviour of i) buffer clay materials and of ii) host clay materials. Technical report, Deliverable D7.1 HITEC. EURAD Project, Horizon 2020, No. 847593. 214 pp.

Villar, M. V., Gómez-Espina, R., & Lloret, A. (2010). Experimental investigation into temperature effect on hydro-mechanical behaviours of bentonite. *Journal of Rock Mechanics and Geotechnical Engineering, 2*(1), 71–78.

Villar, M., Martín, P., Bárcena, I., García-Siñeriz, J., Gómez-Espina, R., & Lloret, A. (2012). Long-term experimental evidences of saturation of compacted bentonite under repository conditions. *Engineering Geology, 149–150*, 57–69.

Wang, J. (2010a). High-level radioactive waste disposal in China: Update 2010. *Journal of Rock Mechanics and Geotechnical Engineering,2*(1), 1–11.

Wang, J. (2010b). High-level radioactive waste disposal in China: Update 2010. *Journal of Rock Mechanics and Geotechnical Engineering,2*(1), 1–11.

Wang, J. (2014). On area-specific underground research laboratory for geological disposal of high level radioactive waste in china. *Journal of Rock Mechanics and Geotechnical Engineering, 6*(2), 99–104.

Wang, W., Rutqvist, J., Görke, U.-J., Birkholzer, J. T., & Kolditz, O. (2010). Non-isothermal flow in low permeable porous media: A comparison of Richards' and two-phase flow approaches. *Environmental Earth Sciences, 62*, 1197–1207.

Wersin, P., Soler, J., Van Loon, L., Eikenberg, J., Baeyens, B., Grolimund, D., Gimmi, T., & Dewonck, S. (2008). Diffusion of HTO, Br^{-}, I^{-}, Cs^{+}, $^{85}Sr^{2+}$ and $^{60}Co^{2+}$ in a clay formation: Results and modelling from an in situ experiment in Opalinus Clay. *Applied Geochemistry,23*(4), 678–691.

Wu, T., Wang, H., Zheng, Q., Zhao, Y. L., & Van Loon, L. R. (2014). Diffusion behavior of se (iv) and re (vii) in gmz bentonite. *Applied Clay Science, 101*, 136–140.

Xie, J., Cao, S., Gao, Y., Ma, L., & Liu, Y. (2018). Exploration of gaomiaozi bentonite deposit and excavation of natural sodium bentonite (in Chinese). *China Mining Magazine, 140*, 125–129.

Xu, L., Ye, W., & Ye, B. (2017). Gas breakthrough in saturated compacted gaomiaozi (gmz) bentonite under rigid boundary conditions. *Canadian Geotechnical Journal, 54*(8), 1139–1149. Cited By 27.

Ye, W.-M., Schanz, T., Lixin, Q., Wang, J., & Arifin, Y. (2007). Characteristics of swelling pressure of densely compacted gaomiaozi bentonite gmz01 (in Chinese). *Yanshilixue Yu Gongcheng Xuebao/Chinese Journal of Rock Mechanics and Engineering,26*, 3861–3865.

Ye, W., Cui, Y., Qian, L., & Chen, B. (2009). An experimental study of the water transfer through confined compacted gmz bentonite. *Engineering Geology, 108*(3), 169–176.

Ye, W.-M., Wan, M., Chen, B., Chen, Y., Cui, Y.-J., & Wang, J. (2009). Effect of temperature on soil-water characteristics and hysteresis of compacted gaomiaozi bentonite. *Journal of Central South University of Technology, 16*, 821–826.

Yong, R. N., Nakano, M., & Pusch, R. (2012). *Environmental soil properties and behaviour*. CRC Press.

Yuan, T., & Fischer, C. (2022). The influence of sedimentary and diagenetic heterogeneity on the radionuclide diffusion in the sandy facies of the opalinus clay at the core scale. *Applied Geochemistry*.

Yuan, T., & Qin, G. (2020). Numerical investigation of wormhole formation during matrix acidizing of carbonate rocks by coupling stokes-brinkman equation with reactive transport model under radial flow conditions. In *SPE International Conference and Exhibition on Formation Damage Control*. OnePetro.

Yuan, T., & Fischer, C. (2021). Effective diffusivity prediction of radionuclides in clay formations using an integrated upscaling workflow. *Transport in Porous Media, 138*(2), 245–264.

Yuan, T., Wei, C., Zhang, C.-S., & Qin, G. (2019). A numerical simulator for modeling the coupling processes of subsurface fluid flow and reactive transport processes in fractured carbonate rocks. *Water, 11*(10), 1957.

Zhang, C.-L., Wang, J., Kaufhold, S., Liu, Y., & Czaikowski, O. (2022). Buffering performance of gmz and mx80 bentonites for geological disposal of high- level radioactive waste. Technical report, GRS report 702, ISBN 978-3-949088-93-3.

Zhang, C.-L. (2021). Deformation and water/gas flow properties of claystone/bentonite mixtures. *Journal of Rock Mechanics and Geotechnical Engineering, 13*(4), 864–874.

Zhang, F., Ye, W.-M., Wang, Q., Chen, Y.-G., & Chen, B. (2019). An insight into the swelling pressure of gmz01 bentonite with consideration of salt solution effects. *Engineering Geology, 251*, 190–196.

Zhao, J., Chen, L., Collin, F., Liu, Y., & Wang, J. (2016). Numerical modeling of coupled thermal-hydro-mechanical behavior of gmz bentonite in the china-mock-up test. *Engineering Geology, 214*, 116–126.

Zhao, X., Wang, J., Cai, M., Ma, L., Zong, Z., Wang, X., Su, R., Chen, W., Zhao, H., Chen, Q., An, Q., Qin, X., Ou, M., & Zhao, J. (2013). In-situ stress measurements and regional stress field assessment of the beishan area, china. *Engineering Geology, 163*, 26–40.

Zhu, H., Fu, H., Yan, P., Li, X., Zhang, L., Wang, X., & Chai, C. (2022). Study on the release of gmz bentonite colloids by static multiple light scattering technique. *Colloids and Surfaces A: Physicochemical and Engineering Aspects*, 128374.

Zhu, C.-M., Ye, W.-M., Chen, Y.-G., Chen, B., & Cui, Y.-J. (2013). Influence of salt solutions on the swelling pressure and hydraulic conductivity of compacted gmz01 bentonite. *Engineering Geology, 166*, 74–80.